TECHNISCHE UNIVERSITÄT WIEN

INSTITUT FÜR PHOTONIK
Photonics Institute

DIPLOMARBEIT

Sidewall Roughness of Silicon Nitride Waveguides in Visible and Ultra-violet Wavelengths

eingereicht von

Luca Rieder

an der

Technischen Universität Wien

Fakultät für Elektrotechnik und Informationstechnik

zum Zwecke der Erlangung des akademischen Grades

Diplom-Ingenieur

unter der Anleitung von

Univ.Prof. Mag.rer.nat. Dr.rer.nat.
Karl Unterrainer

Wien, September 2025

Eidesstattliche Erklärung

Ich erkläre an Eides statt, dass ich die vorliegende Arbeit selbstständig und ohne fremde Hilfe verfasst, andere als die angegebenen Quellen und Hilfsmittel nicht benutzt bzw. die wörtlich oder sinngemäß entnommenen Stellen als solche kenntlich gemacht habe. Zudem bestätige ich, dass keine künstliche Intelligenz (KI) für die Verfassung der Arbeit bzw. für Teile der Arbeit zum Einsatz gekommen ist.

Wien, am 18.08.2025

……
Luca Rieder

Einverständniserklärung zur Plagiatsprüfung

Ich nehme zur Kenntnis, dass die vorgelegte Arbeit mit geeigneten und dem derzeitigen Stand der Technik entsprechenden Mitteln (Plagiat-Erkennungssoftware) elektronisch-technisch überprüft wird. Dies stellt einerseits sicher, dass bei der Erstellung der vorgelegten Arbeit die hohen Qualitätsvorgaben im Rahmen der ausgegebenen der an der TU Wien geltenden Regeln zur Sicherung guter wissenschaftlicher Praxis - „Code of Conduct“ (Mitteilungsblatt 2007, 26. Stück, Nr. 257 idgF.) an der TU Wien eingehalten wurden. Zum anderen werden durch einen Abgleich mit anderen studentischen Abschlussarbeiten Verletzungen meines persönlichen Urheberrechts vermieden.

Wien, am 18.08.2025

……
Luca Rieder

Kurzfassung

Diese Arbeit untersucht das Design, die Herstellung, die Charakterisierung und die Verlustanalyse von Siliziumnitrid-(SiN)-Wellenleitern im sichtbaren bis nahen UV-Wellenlängenbereich, mit einem Fokus auf der Charakterisierung von Ausbreitungsverlusten durch eine detaillierte Untersuchung der Seitenwandrauheit. Wellenleiter wurden erfolgreich gefertigt und charakterisiert, sowie die gemessenen Verluste mit Simulationen verglichen.

Die Untersuchung bewertet verschiedene Ätztechniken und -werkzeuge, um den optimalen Prozess zu ermitteln, der Konuswinkel nahe 90° und minimale Seitenwandrauheit für SiN-Wellenleiter erreicht. Der beste Fertigungsprozess erzielte Seitenwandrauheitswerte im quadratischen Mittel von 1.05 nm und einer Korrelationslänge von 67 nm entlang der Ausbreitungsrichtung des geführten Lichts bei einem Konuswinkel von 85° im Querschnitt des Wellenleiters, was mit dem Stand der Technik vergleichbar ist. Die Wellenleiter wurden bei mehreren Wellenlängen gemessen, mit Ergebnissen von 6.02±0.77 dB/cm bei $\lambda = 532$ nm und bis zu 0.95±0.10 dB/cm bei $\lambda = 730$ nm für transversal elektrisch (TE)-polarisiertes Licht. In Kombination mit einem exponentiellen Materialabsorptionsmodell wurden die Verluste mithilfe eines bereits etablierten Modells zur Schätzung von Streuverlusten modelliert. Der Vergleich zeigt eine akzeptable Übereinstimmung zwischen Messung und Simulation, obwohl bei kürzeren Wellenlängen und schmaleren Wellenleiterdimensionen Abweichungen weitere Untersuchungen erfordern.

Letztlich zeigen die Ergebnisse, dass aktuelle Fertigungstechniken zwar akzeptable Rauheitswerte erzielen, jedoch zusätzliche Schritte erforderlich sind, um rauheitsbedingte Streuverluste weiter zu reduzieren und die Skalierbarkeit von photonischen integrierten Schaltungen (PIC) zu erreichen. Insbesondere für den Einsatz in Quantencomputern mit gefangenen Ionen, bei denen effiziente Lichtführung und hohe optische Güte entscheidend sind. Durch die Bewältigung von Fertigungsherausforderungen und die Verfeinerung von Verlustvorhersagemethoden schafft diese Arbeit die Grundlage für die Realisierung von ultra-verlustarmen Wellenleitern und vollständig integrierten PIC-Plattformen.

Abstract

This thesis investigates the design, fabrication, characterisation, and loss analysis of silicon nitride (SiN) waveguides in the visible to near-UV wavelength range, with a focus on characterising propagation losses through a detailed study of the sidewall roughness. Waveguides were successfully fabricated and characterised, while measured losses were compared to simulations.

The study evaluates various etching techniques and tools to determine the optimal process to achieve taper angles close to 90° and minimal sidewall roughness for SiN waveguides. The best fabrication process achieved root mean square sidewall roughness values of of 1.05 nm and correlation lengths along the waveguide's propagation direction of 67 nm at a taper angle of 85° of the waveguide's cross section, comparable to state-of-the-art benchmarks. The waveguides were measured for multiple wavelengths with results of 6.02±0.77 dB/cm at $\lambda = 532$ nm and as low as 0.95±0.10 dB/cm at $\lambda = 730$ nm for transverse electric (TE) polarised light. Combined with an exponential material absorption fit, losses were modelled using an already established model for estimation of the scattering loss. The comparison shows acceptable agreement of measurement and simulation, though deviations at shorter wavelengths and narrow waveguide dimensions require further investigation.

Ultimately, the results indicate that while current fabrication techniques result in acceptable roughness, further steps need to be taken to reduce roughness-induced scattering losses to achieve scalability of photonic integrated circuits (PIC). In particular, for trapped-ion quantum computing, where efficient light delivery and high optical fidelity are paramount. By addressing fabrication challenges and refining loss prediction methodologies, this thesis sets the stage for realising ultra-low-loss waveguides and achieving fully integrated PIC platforms.

Contents

CHAPTER 1

Introduction

Photonic integrated circuits (PICs) for visible light are a promising technology for medical diagnostics [1], gas sensing [2], photodetectors [3], and the scalability of quantum computing using neutral atoms [4], photons [5], and trapped ions [6]. For trapped-ion quantum computing, ions are confined in all three dimensions by an electromagnetic field forming an effective potential well. This trapping field is caused by a combination of static and dynamic potentials of the ion traps surface electrodes. Lasers are used to control the electronic states of the ion. The two-level system of the qubit as a basic unit is formed by choosing two states of the ion's manifold of available states. To initialize the qubit, laser cooling to the motional ground state of the system is utilized, followed by optical pumping to prepare the state. Afterwards an additional laser pulse is applied to excite the ion to a chosen qubit state. The qubit state readout is performed via a cycling-transition of one of the qubit states to an additional short lived state. The fluorescence light is collected by a microscope and a sensitive camera [7]. To implement the basis for gate operations, long-lived excited states of the system are selected and qubit rotation is driven with an additional laser pulse [8]. Instead of using lasers, microwave gates can be realized by driving the ion's qubit transition using microwave fields [9].

Scaling the number of qubits while maintaining high fidelity is one of the main challenges to achieve fault tolerant quantum computers. Here Infineon Technologies AG takes advantage of the advances made in semiconductor manufacturing to produce microfabricated ion traps [10]. Although the chip-integrated approach scales well, optical access of the lasers poses a major bottleneck in the scalability as free-space optics are commonly used for the optical interaction mentioned above, here integrated photonics offers a solution. Passive components such as waveguides and grating couplers are used to deliver light to

the ion, while active components such as modulators are used to manipulate properties of the laser light on chip. A schematic cross-section of a grating coupler delivering light to a trapped ion is shown in Figure 1.1a. Mehta et al. [6] have shown such a chip-integrated light delivery to a $^{88}Sr^{+}$ ion, a schematic view of their light delivery zone is depicted in Figure 1.1b.

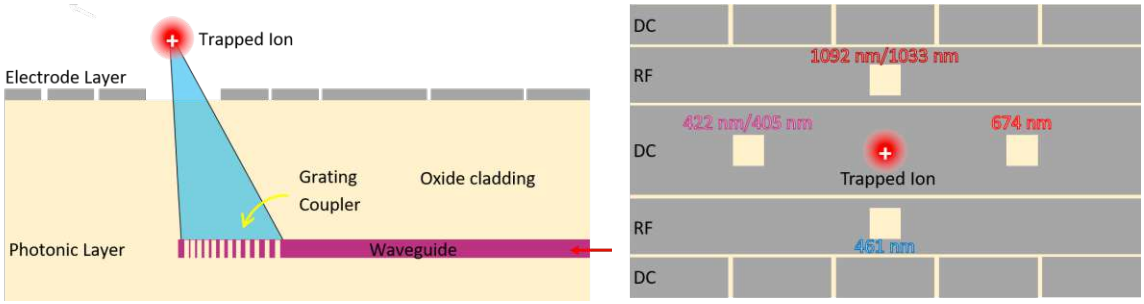

(a) (b)

Figure 1.1: (a) Schematic cross-section of a SiN waveguide and grating coupler in SiOx cladding to deliver light to the trapped ion, (b) Schematic top-down view of the site where the ion is illuminated by laser light, the square windows allow the light to be delivered from the grating couplers below for different wavelengths, as seen in [6].

Of note is the wide variety of different wavelengths which are required to manipulate the ion. To effectively carry out the ion-laser interactions mentioned above, the intensity at the ion must be as required, high waveguide losses would thus require an increased input power. Therefore, the light delivery to the grating coupler must exhibit low loss for the needed light wavelengths, as scattering and absorption of the light in the waveguide reduces the intensity of the outcoupled light at the ion, which is detrimental for scaling. Additionally, scattered light could unintentionally interact with other ions. Figure 1.1a shows that a silicon nitride (SiN) waveguide is used, as material absorption losses are low in the visible wavelength regime compared to commonly used PIC materials such as silicon (Si) which shows high absorption. For wavelengths in the UV spectrum (< 400 nm) materials such as aluminium oxide (Al_2O_3) are commonly preferred over SiN as it exhibits high material losses. Figure 1.2 shows simplified electronic state diagrams for (a) calcium, (b) strontium, and (c) barium ions. Other less commonly used ion species in quantum computing are ytterbium and beryllium, whose state diagrams are not depicted here. The latter ion species is of interest for this thesis because it exhibits the widest variety of required wavelengths for quantum computing: From 493.5 nm for Doppler cooling and readout to 1760 nm for the qubit transition, which waveguides for barium would therefore be required to guide. Figure 1.2 emphasises the wide variety of wavelengths needed for trapped ions, which must be guided by waveguides.

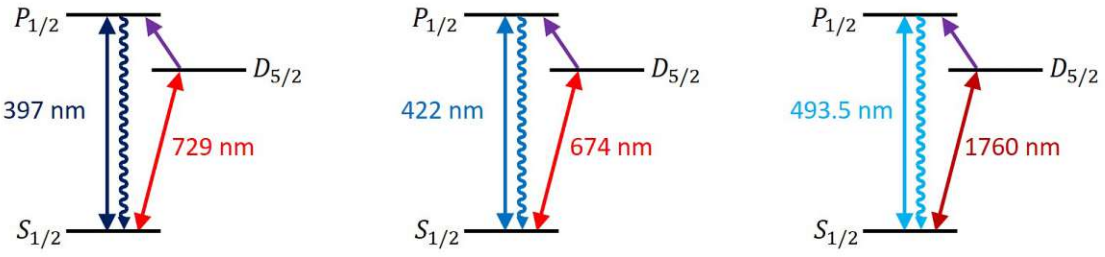

Figure 1.2: Simplified electronic state diagrams of (a) calcium, (b) strontium and (c) barium [11].

Material losses are not the only loss mechanism that affects waveguides. For wavelengths greater than 400 nm, scattering due to roughness of the sidewalls was shown to cause most losses [12][13]. The loss due to sidewall roughness is commonly described by the Payne-Lacey model [14], which is accurate for the slab waveguide, that is, waveguides showing a large width-to-height ratio. Recently, a model by Hoermann et al. [15] was proposed aiming to accurately describe the losses of waveguides with width-to-height ratios closer to unity.

Within this thesis, I fabricated SiN waveguides in the cleanroom of Infineon Technologies in Villach that are able to guide wavelengths from 493 to 866 nm and measured their propagation losses under the supervision of Alexander Zesar in the Ion Trap Systems group at Infineon Technologies. As will be shown in a later chapter, the propagation loss for IR wavelengths is negligible compared to losses in the visible spectral range, which is why IR wavelengths were not closely investigated in this thesis. Furthermore, the sidewall roughness of the fabricated waveguide structures is measured and statistical parameters of the sidewall topography are extracted that are used to calculate the expected loss of the waveguides using a Python implementation of the model from [15].

Chapter 2 focusses on the fundamental properties of plane waves for waveguiding and light-matter interaction. Chapter 3 describes the frequency dependence of the material by introducing different models to describe the dependence. Chapter 4 presents how light behaves at a dielectric interface, leading to the equations needed for waveguiding. In the end of Chapter 4, a short overview of the simulation of waveguides is given. In Chapter 5, the commonly used Payne-Lacey model is introduced together with the Hoermann model, both of which describe the loss due to scattering of a waveguide. Chapter 6 shows the current state of the art for waveguide fabrication and measurement. In Chapter 7, measured refractive indices and losses for SiN are fitted using models described in Chapter 3. Chapter 8 focusses on the design of the PIC used in this thesis, while Chapter 9 describes the fabrication process and shows the results of the different investigated

methods and processes. The results of the measurement of fabricated waveguides are shown in Chapter 10 and Chapter 11 compares the measurements with simulations.

CHAPTER 2

Light as an Electromagnetic Wave

For the purpose of the waveguiding of monochromatic laser light, it can be assumed that the light propagates as plane waves of the form [16]

$$\mathbf{E}(\mathbf{x}, t) = \mathbf{E}_0 \mathrm{e}^{-\mathrm{j}(\mathbf{k}\cdot\mathbf{x}-\omega \mathrm{t})} \tag{2.1}$$

with the wavevector $\mathbf{k} \coloneqq k\mathbf{e}$ and its magnitude k, which is often called the wavenumber or propagation constant, while $\mathbf{e}$ is the unit vector which defines the vector orientation and ω denotes the angular frequency. The imaginary part of the argument of the exponential function, in this case $-(\mathbf{k}\cdot\mathbf{x}-\omega t)$, is called the phase. The wavevector $\mathbf{k}$ and the angular frequency ω are not independent of each other and are connected through the dispersion relation

$$k^2 = \frac{\omega^2}{c_0^2}\varepsilon_r \tag{2.2}$$

where c_0 is the speed of light in vacuum and ε_r the relative permittivity of the material. The commonly known form is the vacuum dispersion relation

$$k_0 \coloneqq \frac{\omega}{c_0}. \tag{2.3}$$

As monochromatic waves from Equation 2.1 oscillate with an angular frequency ω, the period of oscillation in time is $2\pi/\omega$. Planes of constant phase $\mathbf{k}\cdot\mathbf{x}-\omega t = \text{const.}$ are normal to the wavevector $\mathbf{k}$. The magnitude of the wavevector $k = |\mathbf{k}|$ is the spatial angular frequency and thus the oscillation period in space. The distance between planes of equal phase is called the wavelength λ, thus the number of spatial oscillations per unit of length is $1/\lambda$ and the spatial angular frequency

$$k := \frac{2\pi}{\lambda} \tag{2.4}$$

with the vacuum wavelength, using Equation 2.3 [16]

$$\lambda_0 = \frac{2\pi}{k_0} = 2\pi\frac{c_0}{\omega}. \tag{2.5}$$

As can be observed in Equation 2.2 the behaviour of light depends on the medium in which it propagates. The polarisation density $\mathbf{P}$ is the reaction of the medium on an impinging electric field and is linear in a first order approximation [16]

$$\mathbf{P} = \varepsilon_0 \chi \mathbf{E} \tag{2.6}$$

with the vacuum permittivity ε_0 and the susceptibility χ as a dimensionless parameter to describe the relationship between the medium and the field. The relative permittivity from Equation 2.2 is

$$\varepsilon_r = 1 + \chi. \tag{2.7}$$

The relationship between light and material will be closer inspected in Chapter 3.

CHAPTER 3

Frequency Dependence of Refractive Index and Absorption

The relationship $\varepsilon_r = 1 + \chi$ between permittivity and susceptibility of a material has been briefly explained in Chapter 2. It is used to describe the reaction of the material to an external electric field, the polarisation. Generally speaking, the polarisation density is the vectorial sum over all microscopic dipole moments in a unit volume. As the elementary charges possess mass, the polarisation does not follow a change in the field instantaneously, it is instead determined by the pattern of the field experienced before. This implies the existence of time constants, which in turn depend on the mechanism of polarisation, and transforming these into the frequency domain shows a frequency dependence of the susceptibility [16]. First, a relationship of the complex permittivity of a material with its absorption and refractive index is presented, followed by a selection of different models to describe the permittivity of a material.

3.1 Absorption and Refractive Index

In general, the permittivity is assumed to be complex $\tilde{\varepsilon}$ and is described by the relation

$$\tilde{\varepsilon} = 1 + \tilde{\chi} =: \varepsilon' + \mathrm{j}\varepsilon''. \tag{3.1}$$

With real numbers ε' and ε'' for the real and imaginary part of the complex permittivity, respectively. This results in a complex wavenumber due to the dispersion relation (Equation 2.2) of

$$\tilde{k} = \frac{\omega}{c_0}\sqrt{\varepsilon' + \mathrm{j}\varepsilon''} =: \tilde{n}k_0 \tag{3.2}$$

with the complex refractive index

$$\tilde{n} = \sqrt{\varepsilon' + \mathrm{j}\varepsilon''} =: n - \mathrm{j}\kappa. \tag{3.3}$$

Solving a system of equations to determine n and κ from $\tilde{\varepsilon}$ yields

$$n^2 = \frac{1}{2}\left[(\varepsilon'^2 + \varepsilon''^2)^{1/2} + \varepsilon'\right] \tag{3.4}$$

and

$$\kappa^2 = \frac{1}{2}\left[(\varepsilon'^2 + \varepsilon''^2)^{1/2} - \varepsilon'\right]. \tag{3.5}$$

This complex wavenumber modifies the spatially dependent part of the plane wave propagating in z direction to

$$\mathbf{E}(\omega)\mathrm{e}^{-\mathrm{j}\tilde{k}(\omega)z} = \mathbf{E}_0\mathrm{e}^{-\kappa(\omega)k_0 z}\mathrm{e}^{-\mathrm{j}n(\omega)k_0 z}. \tag{3.6}$$

The imaginary part of the refractive index $\kappa(\omega)$ acts as a frequency-dependent dampening of the amplitude, the sign is chosen so that the wave decreases exponentially for a propagation in positive z-direction. The intensity is the square of the absolute value of the electric field's amplitude and thus

$$\frac{I(z)}{I(0)} = \mathrm{e}^{-2\kappa k_0 z} := \mathrm{e}^{-\alpha z} \tag{3.7}$$

with

$$\alpha = 2\kappa k_0. \tag{3.8}$$

This introduces the commonly used value α called the absorption coefficient, where $1/\alpha$ denotes the absorption length, meaning the distance after which the intensity dropped by 1/e [16].

As mentioned in Chapter 2 the current polarisation depends on the current electric field. Therefore, the real and imaginary parts of the susceptibility are directly connected which is described by the Kramers-Kronig relations [16].

A widely accepted model to describe polarisation is the Lorentz-Drude model. It combines a harmonic oscillator that binds an electron of mass m_e with a force $a\mathbf{x}$ to the atom, with a velocity-dependent damping of the electron's movement $b\dot{\mathbf{x}}$. The parameters a and b can be thought of as the spring constant and damping of a spring-mass-system and $\mathbf{x}$ the mechanical deflection of the system [16]. However, the Lorentz-Drude model does not contain any description of the electronic structure of the material. The Tauc-Lorentz and Tauc-Lorentz-Uhrbach models do contain a modification of the Lorentz-Drude model due to the electric density of states (DOS) and energy bands of the materials.

3.2 Density of States and Energy Bands

The density of states is the number of free electronic states per unit volume and per unit energy around an energy E. The DOS denoted by $N(E)$ and the number of states in a unit volume around an energy interval dE around an energy E is $N(E)dE$. In three-dimensional systems, such as SiN, the DOS is $N(E) \propto \sqrt{E}$. Between the valence and conduction bands of a material is the bandgap E_g. An example of the 3D DOS for the valence and conduction bands is shown in Figure 3.1.

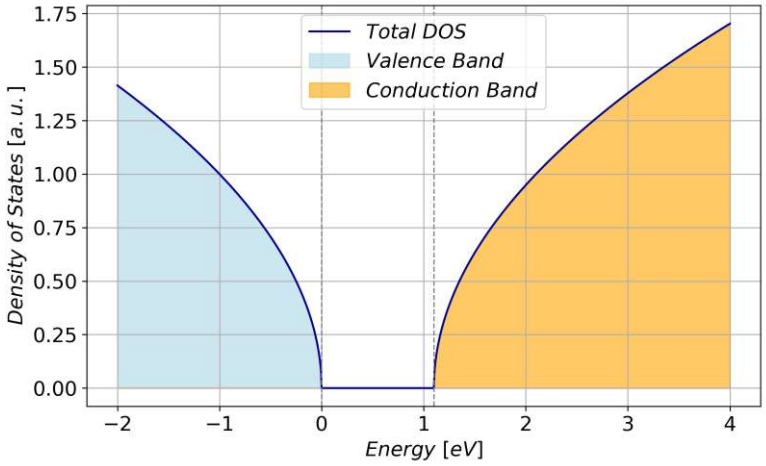

Figure 3.1: Example of the density of states for a 3D material. The conduction and valence bands are separated by the bandgap E_g of energy 1.1 eV. The grey dotted lines represent the energy at the top of valence band E_v as well as the energy at the bottom of the conduction band E_c.

In crystalline materials, which exhibit periodicity, the band structure describes how the energy of electrons is affected by their momentum in the k-space. Although amorphous materials, such as SiN and amorphous Si, do not have band structures in the k-space sense due to their lack of periodicity, the do possess energy bands and the aforementioned DOS [17].

Semiconductors as well as dielectric materials can exhibit an exponential decay of the absorption coefficient below the bandgap energy [18]

$$\alpha(E) = \alpha_0 \exp\left(\frac{E}{E_0}\right). \tag{3.9}$$

This Urbach tail stems from the exponential tail of the density of states in the top of the valence band or bottom of the conduction band. One possible explanation was proposed by Bacalis et al. [19] wherein they named fluctuating potentials as the source of exponential tails. According to them, the tail is caused by independent local potential wells of atomic scale whose depths exhibit a Gaussian distribution. Figure 3.2 demonstrates how the bands are extended into the bandgap by the exponential Urbach tail, meaning that energy states exist in the bandgap which would otherwise be forbidden.

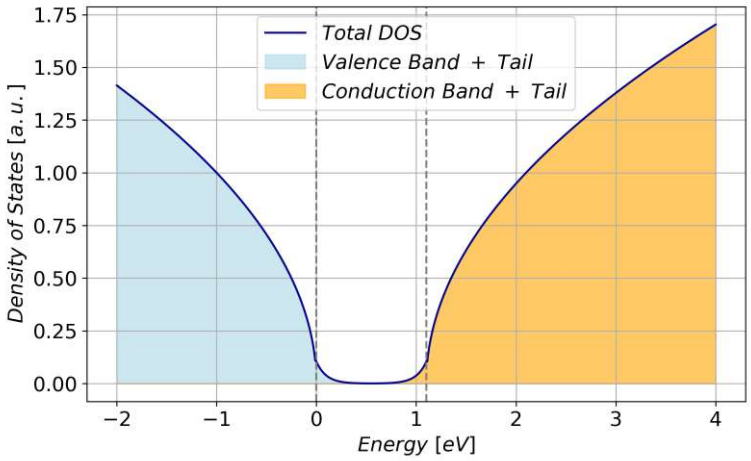

Figure 3.2: Modified example from Figure 3.1 to show the extension of the bands via the exponential Urbach tail.

3.3 Tauc-Lorentz Model

The Tauc-Lorentz (TL) model combines the Tauc model of the DOS with the Lorentz-Drude model. It is commonly used to describe amorphous semiconductors and insulators, and thus it could also be used to describe silicone nitride. Larruquert and Rodriguez de Marcos [20] propose an analytical modification, as previous models relied on piecewise functions which change the functional behaviour at the energy gap. This results in a kink of the resulting function, which is thus non-analytical and therefore does not fulfil the Kramers-Kronig relations. They arrive at a formalism which enables an analytical fit over large photon energies. The energy of photons is calculated by the following commonly known formula

$$E_{ph} = \frac{hc}{\lambda} = \hbar\omega \tag{3.10}$$

whereas h is Planck's constant, c the speed of light, and λ the photon's wavelength.

Larruquert and Rodriguez de Marcos [20] modify the Tauc-Lorentz model, by using the imaginary ($\tilde{\varepsilon}_r''$) or the real part ($\tilde{\varepsilon}_r'$) of the non-analytic permittivity function $\tilde{\varepsilon}_r$ to obtain the analytical function $\tilde{\varepsilon}_{r,an}$. Integrating $\tilde{\varepsilon}_{r,an}$ results in

$$\tilde{\varepsilon}_{r,TL-an}(E; A, E_0, E_g, C, a) = 1 + \frac{AE_0C}{\pi}\left[F(b, d, d^*) + F(d, d^*, b) + F(d^*, b, d)\right] \tag{3.11}$$

with

$$F(\alpha, \beta, \gamma) = \frac{(E_g + \alpha)^2 \log(E_g + \alpha) - (E_g - \alpha)^2 \log(E_g - \alpha)}{\alpha(\alpha^2 - \beta^2)(\alpha^2 - \gamma^2)} \tag{3.12}$$

$$b \equiv b(E) \equiv E + \mathrm{j}a \tag{3.13}$$

$$d = \sqrt{E_0^2 - \left(\frac{C}{2}\right)^2} - \mathrm{j}\frac{C}{2} \tag{3.14}$$

with A as a fitting parameter, E_0 as the central energy of the oscillator, E_g as the bandgap energy, C the width of the oscillator, and a a parameter used for a weight function. The asterisk denotes the conjugate complex. Equation 3.11 is the analyticized Tauc-Lorentz model (TL-an). Due to the single expression for the permittivity, it can be fitted with experimental data from the complex refractive index $\tilde{n}$ [20].

3.4 Tauc-Lorentz-Urbach Model

Even though the imaginary part of the TL-an model approaches zero for energies below E_g, the decay does not fit for materials that exhibit a Urbach tail.

The model proposed by Foldyna et al. [21] contains two piecewise functions in the intervals $E < E_c$ and $E > E_c$ where E_c is the connection energy between the two functions. This results in their Tauc-Lorentz-Urbach (TLU) model being non-analytic. It is transformed in the same way as the TL model. The Urbach tail term is integrated for energies below E_c while the TL term is integrated for energies above E_c. The new analytic model, called TLU-an is given by the addition of the two terms [20]

$$\begin{aligned}\tilde{\varepsilon}_{r,TLU-an}(E) =& \tilde{\varepsilon}_{r,U-an}(E; A, E_0, E_g, C, a, E_c) + \\ & \tilde{\varepsilon}_{r,TL-an}(E; A, E_0, E_g, C, a, E_c).\end{aligned} \tag{3.15}$$

The permittivites $\tilde{\varepsilon}_{r,U-an}$ and $\tilde{\varepsilon}_{r,TL-an}$ are evaluated as follows:

$$\begin{aligned}\tilde{\varepsilon}_{r,U-an}(E; A, E_0, E_g, C, a, E_c) &= 1 + \frac{1}{\pi}\int_{-\infty}^{\infty} \frac{\varepsilon''_{r,U}(E')}{E' - E - \mathrm{j}a} dE' \\ &= \frac{A_u}{\pi}\left\{ b\exp\left(\frac{b}{E_u}\right)\left[\mathrm{Ei}\left(\frac{E_c - b}{E_u}\right) - \mathrm{Ei}\left(\frac{-b}{E_u}\right)\right] \right. \\ &\quad + b\exp\left(\frac{-b}{E_u}\right)\left[\mathrm{Ei}\left(\frac{b}{E_u}\right) - \mathrm{Ei}\left(\frac{E_c + b}{E_u}\right)\right] \\ &\quad \left. + 2\exp\left(\frac{E_c}{E_u}\right)E_u - 2E_u \right\}\end{aligned} \tag{3.16}$$

with the addition that the sign of $\varepsilon''_{r,U}$ was reversed for negative energies to turn it into an odd function. The function Ei stands for the exponential integral

$$\mathrm{Ei}(z) = -\int_{-z}^{\infty} \frac{\mathrm{e}^{-t}}{t} dt \tag{3.17}$$

which is included in common mathematical packages such as Scipy for Python.

$$\tilde{\varepsilon}_{r,TL-an}\left(E;A,E_0,E_g,C,a,E_c\right)=1+\frac{AE_0C}{\pi}\left[\bar{F}\left(b,d,d^*\right)+\bar{F}\left(d,d^*,b\right)+\bar{F}\left(d^*,b,d\right)\right] \tag{3.18}$$

with

$$\bar{F}(\alpha,\beta,\gamma)=\frac{\left(E_g+\alpha\right)^2\log\left(E_c+\alpha\right)-\left(E_g-\alpha\right)^2\log\left(E_c-\alpha\right)}{\alpha\left(\alpha^2-\beta^2\right)\left(\alpha^2-\gamma^2\right)}. \tag{3.19}$$

The comparison between $\bar{F}$ in Equation 3.19 and F in Equation 3.12 shows that the only difference is the replacement of E_g with the new parameter E_c in the logarithms. Therefore, $\bar{F}$ converges to F for $E_c = E_g$, while $b(E)$ and d are given by Equations 3.13 and 3.14 respectively [20].

The TLU-an model is analytic, as singularities occurring in the $b(E)$ function counterbalance each other, $\tilde{\varepsilon}_{r,U-an}$ decays asymptotically for large energies, and it is not a piecewise function. Unlike a piecewise function, it is made up of two terms, each of which is defined over the full spectrum and corresponds to the functionality of the TLU model. Furthermore, the function does not diverge at zero energy. Unlike the TL and TLU models, the additional parameter $\varepsilon_r'(\infty)$ for ε_r' is not needed any more. The model can therefore be fit with either ε_r', ε_r'' or both. As with the TL-an model, experimental data from n, κ or both can be used to fit the TLU-an model [20].

CHAPTER 4

Waveguiding

This chapter introduces the behaviour of monochromatic light at a dielectric interface that lays the basis for the discussion of the dielectric slab waveguide, which is discussed subsequently. The chapter closes with a brief overview of the rectangular waveguide and the simulation of such a waveguide.

4.1 Light at an interface

Assuming that a plane wave impinges on a perfectly flat interface between to media i and t with the refractive indices n_i and n_t under a certain angle θ^i between the wave's wavevector $\mathbf{k}^i$ and the normal of the interface, the impinging wave i is partly refracted in the medium i, denoted as wave r in medium r where $n_i = n_r$ and therefore $\theta^i = \theta^r$, and partly transmitted into the medium t with an angle θ^t. The spatial periodicity of the three waves at the interface must be equal, which results in the condition that the tangential component, the component parallel to the interface, of the three wavevectors $n_{i,r,t}k_0 \sin\theta^{i,r,t}$ must be equal at the interface . This results in the condition

$$\sin\theta^r = \sin\theta^i \tag{4.1}$$

and Snell's law

$$n_t \sin\theta^t = n_i \sin\theta^i \tag{4.2}$$

which holds for optically isotropic media [16].

If the medium i is optically denser than the medium t, which means $n_i > n_t$, the tangential component can be larger than the wavevector's magnitude for certain θ_i. This

results in total internal reflection, where only a reflected wave exists with the critical angle θ_c

$$\theta^i > \theta_c := \arcsin \frac{n_t}{n_i}. \tag{4.3}$$

Under total internal reflection, the perpendicular component of the wave vector is imaginary in the optically thinner medium

$$k_z^t = \pm k_0 \sqrt{n_t^2 - n_i^2 \sin^2 \theta^i} =: \pm \mathrm{j}\gamma^t \tag{4.4}$$

and the wave in the optically thinner medium (for which we assume the area z<0) is given by

$$E^t = E_0^t e^{-\mathrm{j}(\mathbf{k}\ \mathbf{x} - \omega t)} = E_0^t e^{\gamma^t z} e^{-\mathrm{j}(k_x^i x - \omega t)}. \tag{4.5}$$

The amplitude of this inhomogeneous wave, called the evanescent wave, decays exponentially with distance from the interface and the sign of Equation 4.4 has to be chosen in such a way as to ensure an exponential decay, for energetic reasons. The depth of penetration is $1/\gamma^t$, which is for incident angles significantly larger than θ_c in the order of one wavelength and increases the closer θ is to θ_c, for $\theta := \theta_c$ it is infinite [16].

It can be shown [16] that the light reflected at an interface experiences a phase shift for total internal reflection depending on the polarisation. For this, the polarisation is separated into two linear polarisations, one perpendicular to the incident plane called σ- or s-polarization, and one parallel to the incident plane called π- or p polarisation. This follows from the fact that the Fresnel coefficients for the polarised light acquire a non-zero imaginary part, where the magnitude of the reflectivity is 1 and the argument is described by the arctan, as described in Equations 4.6 and 4.7. The incident wave is subject to a phase shift $\phi_{\sigma,\pi}$ dependent on the incident angle θ^{i} at the dielectric interface

$$\frac{\phi_\sigma}{2} = \arctan \frac{\gamma^{\mathrm{t}}}{k_z^{\mathrm{i}}} = \arctan \frac{\left(n_{\mathrm{i}}^2 \sin^2 \theta^{\mathrm{i}} - n_{\mathrm{t}}^2\right)^{1/2}}{n_{\mathrm{i}} \cos \theta^{\mathrm{i}}} \tag{4.6}$$

and

$$\frac{\phi_\pi}{2} = \arctan \frac{n_{\mathrm{i}}^2}{n_{\mathrm{t}}^2} \frac{\gamma^{\mathrm{t}}}{k_z^{\mathrm{i}}} = \arctan \frac{n_{\mathrm{i}}^2}{n_{\mathrm{t}}^2} \frac{\left(n_{\mathrm{i}}^2 \sin^2 \theta^{\mathrm{i}} - n_{\mathrm{t}}^2\right)^{1/2}}{n_{\mathrm{i}} \cos \theta^{\mathrm{i}}}. \tag{4.7}$$

The phase shift is different for σ- and π-polarised light, and the difference depends on the incident angle θ^{i} as well as the ratio of $n_{\mathrm{i}}/n_{\mathrm{t}}$.

4.2 Planar Dielectric Waveguide

Even though rectangular waveguides are used in modern PICs, the fundamental properties of waveguiding are best explained by using the so-called planar or slab waveguide. It consists of a substrate, core, and cladding layer with refractive indices of n_s, n_g, and n_c respectively. The layered structure is depicted in Figure 4.1.

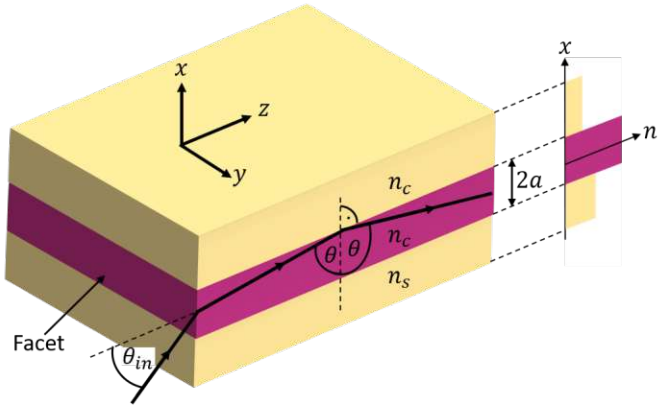

Figure 4.1: Planar waveguide structure. The core material n_g of thickness $2a$ guides the modes, which bounce under the mode's angle θ at the interfaces, with the substrate material n_s and the cladding material n_c on bottom and top, respectively. The waveguide is extended infinitely in y-direction. Pictured the right side is the refractive index of the three materials, where n_c must be larger than the others to enable waveguiding [16].

Both interfaces are plane, and thus it can be assumed that a pair of planar waves which merge into each other as they reflect at the interfaces exist, as shown in Figure 4.2 the wavevectors are therefore [16] [22]

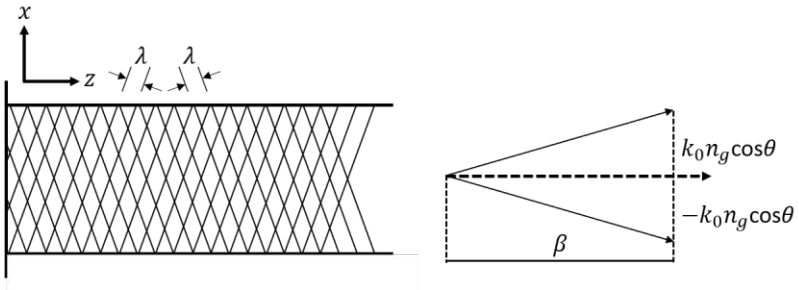

Figure 4.2: Graphical depiction of the two planar waves which superimpose as the waveguide's modes inside the waveguide. Shown on the right side are the wavevectors of the two waves [16].

$$\begin{bmatrix} \pm k_\perp \\ 0 \\ k_\parallel \end{bmatrix} =: \begin{bmatrix} \pm k_\perp \\ 0 \\ \beta \end{bmatrix} = n_g k_0 \begin{bmatrix} \pm \cos\theta \\ 0 \\ \sin\theta \end{bmatrix}. \tag{4.8}$$

One condition for a guided wave is the total internal reflection at both interfaces,

which means that the tangential component of the wavevector $k_{\parallel}$, further labelled as β, is larger than the wavenumber in the adjacent media

$$\beta \coloneqq n_g k_0 \sin\theta > n_{s,c} k_0. \tag{4.9}$$

Thus, the angle θ must be larger than the critical angle (4.3) at the interface. To simplify and without restriction of generality, it is assumed that $n_s \geq n_c$, which results in [16]

$$\theta > \theta_{\text{crit}} \coloneqq \arcsin \frac{n_g}{n_c}. \tag{4.10}$$

The assumption is valid because the smaller refractive index defines the largest critical angle.

Another important aspect is the incoupling of light, which is most commonly done via the facet of the waveguide, as seen in Figure 4.1. For efficient incoupling, the field that would be coupled out of the waveguide into the medium with refractive index n should have a good overlap with the field coupled from the medium with n into the waveguide. Therefore, it is of interest to transform Equation 4.10 into a condition for the largest incident angle $\theta_{\text{in,max}}$ allowed on the facet. Assuming that light is coupled in from a medium of refractive index n yields

$$n \sin\theta_{\text{in,max}} = n_g \cos\theta_{\text{crit}} = n_g \sqrt{1 - \sin^2\theta_{\text{crit}}} = \sqrt{n_g^2 - n_s^2} =: \text{NA}. \tag{4.11}$$

The so-called numerical aperture NA is defined by the difference of refractive indices in the waveguide's layers and determines the largest angle of acceptance [16].

The second condition for waveguiding is the self-consistency condition. It requires the planar waves to reproduce themselves after being reflected twice, so that only two distinct plane waves, as seen in Figure 4.2, can exist. This is possible if the accumulated phase of the two reflections is a multiple of 2π. As waves travel through the layer of thickness $2a$ twice, one part of the phase is $-4k_{\perp}a$. The second is the phase shift at the dielectric boundaries $\phi^s + \phi^c$, as described in Equations 4.6 and 4.7. Therefore, the self-consistency condition is [16] [22]

$$-4k_{\perp}a + \phi^s_{\sigma,\pi} + \phi^c_{\sigma,\pi} = -2\pi m, \qquad m = 0, 1, 2, \ldots \quad . \tag{4.12}$$

Depending on the polarisation of the light. Equation 4.12 thus has, for a given set of parameters a, k_0 and $n_{g,s,c}$ a finite number of solutions $\theta^{(m)}$, where each is equal to an eigenmode with the propagation constants

$$\beta^{(m)} = n_g k_0 \sin\theta^{(m)} =: n_{\text{eff}}^{(m)} k_0 \tag{4.13}$$

and the phase velocities

$$v_{ph}^{(m)} = \frac{\omega}{\beta^{(m)}} = \frac{c_0}{n_{\text{eff}}^{(m)}}. \tag{4.14}$$

Here, $n_{\text{eff}}^{(m)}$ is called the effective refractive index

$$n_{\text{eff}}^{(m)} = \frac{\beta}{k_0} = n_g \sin\theta^{(m)} \tag{4.15}$$

which is in the interval $n_{s,c} < n_{\text{eff}}^{(m)} < n_g$ [16][22].

To facilitate single mode operation of the waveguide, the so-called cut-off condition or cut-off frequency is

$$V < V_c \coloneqq \pi/2 \tag{4.16}$$

where

$$V \coloneqq ak_0\sqrt{n_g^2 - n_{s,c}^2} = ak_0\text{NA} = 2\pi\frac{a}{k_0}\text{NA} = a\frac{\omega}{c_0}\text{NA} \tag{4.17}$$

is the normalised frequency, which is proportional to the frequency of the light and includes all relevant parameters of the waveguide. Equation 4.16 can also be expressed in terms of the wavelength

$$\lambda_0 > \lambda_{0,c} = 4a\text{NA} \tag{4.18}$$

where $\lambda_{0,c}$ is referred to as the cut-off wavelength for single mode operation [16].

The solutions for the modes were focused on the case of σ-polarised light, where the electric field possesses no longitudinal components. The modes are referred to as transverse electrical (TE) modes. The solution for π-polarised light can be obtained similarly [22].

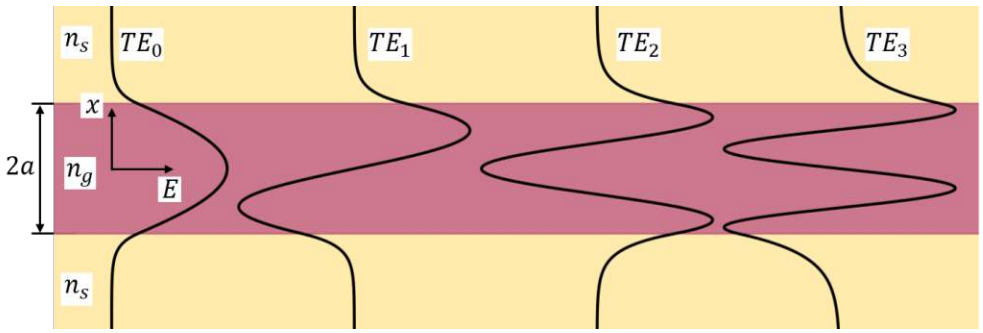

Figure 4.3: Transversal field distribution of the first four TE modes for a symmetrical waveguide ($n_s = n_c$), note that the evanescent field penetrates deeper into the cladding for a higher mode number [16].

After determining the propagation constants, the transversal amplitude distributions of the modes' fields can be described. Within the core material, the field results from the superposition of two plane waves, as shown in Figure 4.2. Depending on the mode number m, the total field inside the core region ($|x| < a$) can be expressed as:

$$E^{\mathrm{g}} = \begin{cases} E_0^{\mathrm{g}} \cos\left(\frac{2\pi \sin\theta_m}{\lambda} x\right) \mathrm{e}^{-\mathrm{j}\beta_m z}, & \text{for even modes } (m = 0, 2, 4, ...) \\ E_0^{\mathrm{g}} \sin\left(\frac{2\pi \sin\theta_m}{\lambda} x\right) \mathrm{e}^{-\mathrm{j}\beta_m z}, & \text{for odd modes } (m = 1, 3, 5, ...) \end{cases} . \tag{4.19}$$

Even modes exhibit symmetrical fields, while odd modes are antisymmetrical, as illustrated in Figure 4.3. The mode number m corresponds to the number of field zero crossings, with the fundamental mode ($m = 0$) having no zero crossing.

In the cladding regions ($|x| > a$), the tangential component of the wavevector remains β, but the normal component becomes imaginary due to total internal reflection. The resulting field has the form:

$$E^{\mathrm{s}} = E_0^{\mathrm{s}} \mathrm{e}^{-\gamma|x|} \mathrm{e}^{-\mathrm{j}\beta_m z}, \tag{4.20}$$

where γ indicates the decay rate of the evanescent field as obtained by Equation 4.4. Higher-order modes exhibit smaller $\beta^{(m)}$ values, implying a deeper penetration of the mode into the cladding materials. The continuity of the transverse electric field at the boundaries ensures a transition between the core and the cladding fields [16] [22].

4.3 Rectangular Dielectric Waveguides

Infinite slabs and circular waveguides, such as optical fibre cables, cannot be achieved with the planar fabrication techniques used in modern semiconductor fabrication, which is why the most commonly used structure for integrated photonic chips is the rectangular waveguide.

Unlike optical fibres, which are used to transport optical signals over long distances, rectangular waveguides involve shorter lengths, typically a few centimetres.

As was the case before for the dielectric slab waveguide, the core material must have a refractive index higher than that of the surrounding cladding. Assuming the simplest case, a purely rectangular waveguide, core and cladding material can be separated into regions as seen in Figure 4.4. Assuming that the frequency of light in the waveguide is significantly larger than the cut-off frequency, the corner regions in Figure 4.4 can be disregarded as the mode is tightly confined in the core material, and thus the power is negligible. For wavelengths closer to the cut-off frequency, perturbation techniques can be used to improve solutions. These cases can be solved analytically, albeit with significant effort, as shown in [23].

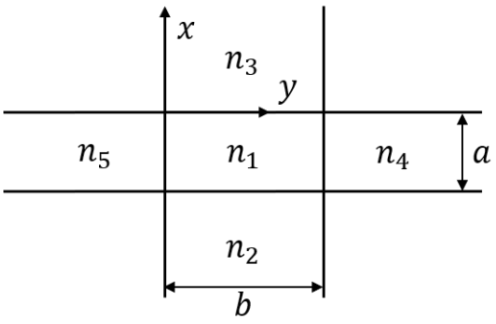

Figure 4.4: A rectangular waveguide with a thickness of a, width b, and refractive index n_1 surrounded by materials of lower refractive index, $n_{2,3,4,5}$. For tight confinement in the core material, solutions for the four corner regions can be neglected [23].

4.3.1 Effective Index Method

The effective index method transforms a single two-dimensional problem into two one-dimensional problems. The buried waveguide in Figure 4.5 serves as an example of how the effective index method functions: First, the waveguide is stretched along its thin x-axis, turning it into a horizontal slab waveguide. This one-dimensional waveguide can be analysed in terms of the TE and TM modes, as shown in Chapter 4.2, which results in the β allowed for the wavelength and mode of interest. The effective index of the slab is then determined by calculating

$$n_{eff} = \frac{\beta}{k_0} \tag{4.21}$$

with the vacuum wavevector k_0.

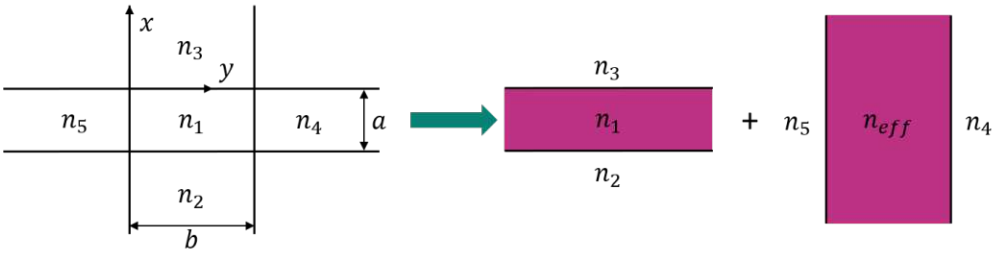

Figure 4.5: Principle of the effective index method. The waveguide is decomposed into two spatially orthogonal waveguides, one horizontal and one vertical slab waveguide. The thinner waveguide is analysed using the initial refractive indices, while the thicker waveguide replaces n_1 with the effective refractive index of the first waveguide [23].

The original structure is then analysed along its thicker y-axis, resulting in a slab waveguide in y-direction. Once again, the modes of this waveguide can be determined, substituting n_1 with the previously determined n_{eff}. The β which is now determined is the actual value for the mode in the rectangular waveguide. One must be cautious

in applying the correct characteristic equations for each structure, using Figure 4.5 as an example again to calculate the field for an electric field polarised in the x-direction: First, the field will appear as a TE mode for the thin slab waveguide, but in the second calculation, the field will appear as an TM mode. The effective index method is only accurate for aspect ratios of width to height of a factor three [23]. The same restrictions as for the slab waveguide remain, the refractive indices n_2-n_5 have to be smaller than the core index n_1. It should also be mentioned that even though the structure in Figure 4.5 shows different refractive indices for the cladding material, it is common that n_3-n_5 are of the same material and often do not deviate too much from n_2.

4.4 Numerical Solutions for Waveguides

The previous chapters provided analytical solutions for waveguides. If the shape of the waveguide's cross-section is, for example, trapezoidal, these methods cannot be applied any more, and numerical methods have to be employed. With ever increasing computational power, it is an easy task to discretise and solve Maxwell's equations. The accuracy of the simulation is limited by the mesh size, and the modes of arbitrary waveguide shapes can be calculated. Common commercial simulation suits are *Ansys Lumerical* and *Comsol*.

For example *Ansys Lumerical* offers a Finite Difference (FD) solver. The two vector fields

$$\begin{aligned} E(x,y)\mathrm{e}^{\mathrm{j}(-\omega t+\beta z)} \\ H(x,y)\mathrm{e}^{\mathrm{j}(-\omega t+\beta z)} \end{aligned} \tag{4.22}$$

with the angular frequency ω and the propagation constant β are the desired modefields for each corresponding β. To find these modes, the waveguide cross section is discretised into a rectangular mesh and Maxwell's equations are solved. The algorithm is able to handle arbitrary waveguide structures. Figure 4.6 depicts the case where the mesh points are not positioned along an interface. Even though the mesh grid lays on dielectric discontinuities, all transverse field components are tangential to the unit cell boundaries, which satisfies the continuity conditions. To approximate the refractive indices at these points, the refractive indices of adjacent cells are averaged [24]. To obtain the effective refractive indices and mode profiles of the waveguide modes, Maxwell's equations are transformed into a matrix eigenvalue problem and solved using sparse matrix techniques [25].

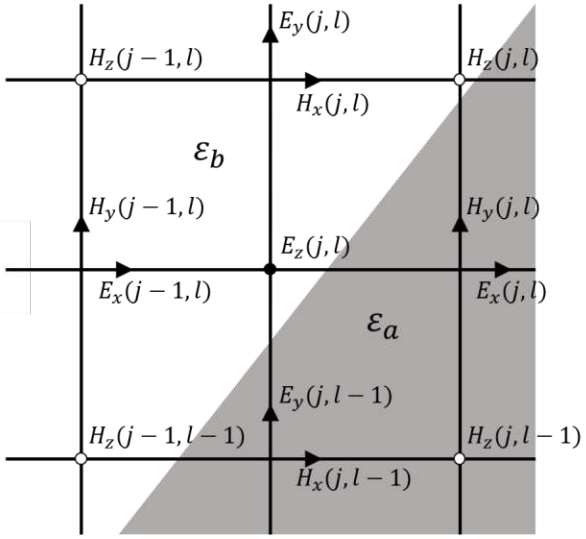

Figure 4.6: Two dimensional mesh at an interface with permittivity ε_a in the shaded area and ε_b in the white area. The z-component of the electric and magnetic fields points into the plane and is connected to four adjacent points containing the y- and z-components of the magnetic and electric field [24].

CHAPTER 5

Scattering Losses in Waveguides

5.1 The Payne-Lacey Model

In Chapter 3 the frequency dependence of the complex permittivity of materials was explained, this includes refractive index n and extinction coefficient κ. Material losses in waveguides correspond to the portion of a guided modes' power in the waveguide, multiplied by the wavelength-dependent loss coefficient, as described in Chapter 3, which yields [13]

$$\alpha_{WG,material} = \alpha_{material}\ P_{confined}\ . \tag{5.1}$$

As will be shown in a later chapter, this loss is small for SiN waveguides in wavelengths >500 nm, yet waveguides still show significant losses in this regime. The cause of this is scattering losses due to rough surfaces caused by etching processes. One of the first investigations was done by Dietrich Marcuse in 1969 [26]. He investigated the losses of slab waveguides, in which he described the scattering losses as mode conversion between guided and unguided modes due to roughness at the waveguide-cladding interface. The statistical treatment of these losses was based on the correlation function of the surface and its corresponding power spectrum. The resulting expression for the waveguide loss is a complicated integral over the radiation modes, which hides the influence of important waveguide parameters such as the material's refractive index or light wavelength. Due to this and improvements in fabrication techniques, Payne and Lacey formulated a simpler expression for the scattering loss coefficient, Equation 5.2, of a rough slab waveguide as depicted in Figure 5.1 [27].

The scattering loss coefficient is calculated by

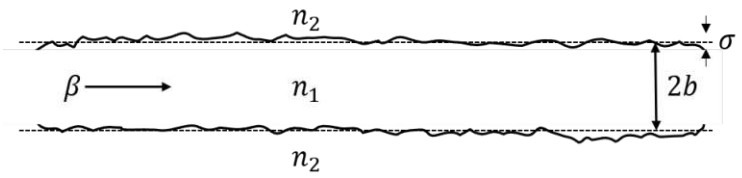

Figure 5.1: Geometry of the planar waveguide used for derivation of Equation 5.2. The slab waveguide exhibits rough top and bottom surfaces, which deviate by the roughness root mean square (RMS) value from the unperturbed waveguide thickness $2d$. As described in Chapter 4.2, the incident mode has the propagation constant β [14].

$$\alpha = \varphi^2(d)(n_1^2 - n_2^2)^2 \frac{k_0^3}{4\pi n_1} \int_0^\pi \tilde{R}(\beta - n_2 k_0 \cos\theta)\mathrm{d}\theta \ . \tag{5.2}$$

Where $\varphi(d)$ is the modal field at the interface between waveguide and cladding, n_1 and n_2 are the refractive indices of the core and cladding, respectively, k_0 is the wavenumber of the free space, and β is the propagation constant. If only one surface is rough, the equation above can be multiplied by 1/2. The spectral density function $\tilde{R}(\Omega)$ describes the surface roughness and is related to the autocorrelation function (ACF) $R(u)$ via the Fourier transform

$$\tilde{R}(\Omega) = \int_{-\infty}^{\infty} R(u) \exp(\mathrm{j}\Omega u)\mathrm{d}u \ . \tag{5.3}$$

The surface roughness is characterised by the correlation length L_c and the mean square deviation σ^2 from the flat surface. The ACF and σ^2 are related via

$$\sigma^2 = R(0) \ . \tag{5.4}$$

The modal field $\varphi(y)$ is normalised so that

$$\int_{-\infty}^{\infty} \varphi^2(y)\mathrm{d}y = 1 \ . \tag{5.5}$$

To gain insight into how important waveguide parameters such as n_1, n_2, d, k_0, σ, or L_c influence scattering, Equation 5.2 is solved analytically [14]. To facilitate this, Payne and Lacey make use of the dimensionless parameters V (Equation 4.17) as well as U and W with

$$U = d\sqrt{n_1^2 k_0^2 - \beta^2} \tag{5.6}$$

and

$$W = d\sqrt{\beta^2 - n_2^2 k_0^2} \ . \tag{5.7}$$

Furthermore, the ACF needs to be an explicit function where they used the exponential

and Gaussian autocorrelation functions, respectively

$$R(u) = \sigma^2 \exp\left(-\frac{|u|}{L_c}\right) \tag{5.8}$$

and

$$R(u) = \sigma^2 \exp\left(-\frac{u^2}{L_c^2}\right) \ . \tag{5.9}$$

5.1.1 Exponential Autocorrelation Function

To evaluate Equation 5.2 the integral needs to be calculated. Inserting the exponential ACF from Equation 5.8 into the integral and solving it yields the power spectral density S. Together with an expression for $\varphi^2(d)$, α can be obtained by combining S and $\varphi^2(d)$ and using the dimensionless parameters

$$\Delta = \frac{n_1^2 - n_2^2}{2n_1^2} \qquad x = W\frac{L_c}{d} \qquad \gamma = \frac{n_2 V}{n_1 W\sqrt{\Delta}} \tag{5.10}$$

where x represents the normalised correlation length, γ describes how weakly the waveguide guides, and the normalised parameters V (Equation 4.17) and W (Equation 5.7). The final expression for α is therefore [14]

$$\alpha = \frac{\sigma^2}{\sqrt{2}k_0 d^4 n_1} g(V) f_c(x,\gamma) \ . \tag{5.11}$$

The function $g(V)$ is determined purely by the waveguide geometry

$$g(V) = \frac{U^2 V^2}{1+W} \tag{5.12}$$

with the normalised parameter U (Equation 5.6). While $f_c(x,\gamma)$ describes the integral over the spectral density function S

$$f_c(x,\gamma) = \frac{x\left\{\left[(1+x^2)^2 + 2x^2\gamma^2\right]^{1/2} + 1 - x^2\right\}^{1/2}}{\left[(1+x^2)^2 + 2x^2\gamma^2\right]^{1/2}} \ . \tag{5.13}$$

Going through the same procedure as above by inserting the Gaussian ACF into the integral yields an expression for S of the Gaussian ACF and thus α is obtained [14].

5.2 Model for Rectangular Waveguides

While the Payne-Lacey model [14] provided accurate estimations for slab waveguides, it is imprecise for rectangular waveguides and shows an overestimation of the scattering loss. There have been attempts to improve the model such as those done by Yap et al.

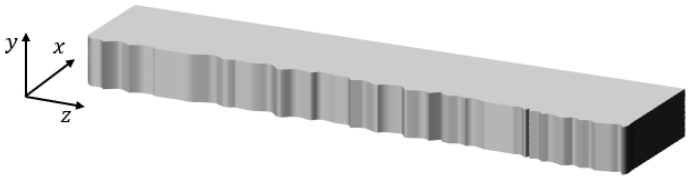

Figure 5.2: Schematic drawing of a rectangular and rough waveguide with the coordinate system used for the model in [15] to describe scattering.

[28] applying a correction factor or by Barwicz and Haus [29]. Both improved it but did not provide accurate estimates and cannot describe waveguides consisting of a stack of different materials such as InPGaAs. Recently, a model by Hoermann et al. [15], further referred to as the Hoermann model, was proposed which aimed at improving these drawbacks for rough sidewalls.

Barwicz and Haus [29] proposed the volume current method (VCM) which models surface roughness as a perturbation in the form of an oscillating volume current, but the discontinuity at the waveguide interface for high-index-contrast waveguides demands additional approximation [15]. The Hoermann model utilises the perturbation from Johnson et al. [30] and therefore allows for arbitrary index profiles, including high-index-contrast systems, with the added benefit that it can be combined with common electrodynamics simulation software suites due to the model's closed form. The model incorporates the surface roughness as Gaussian processes, which enables analysis of the whole surface.

The model assumes that the mode propagates as a plane wave along the waveguide in z-direction, which decays exponentially with α as it travels along the waveguide in the form of

$$\mathbf{E}(\mathbf{r},t) = \mathbf{E}_0(x,y)\mathrm{e}^{(\mathrm{j}\beta-\alpha)z-\mathrm{j}\omega t} \ . \tag{5.14}$$

5.2.1 Roughness Statistics

The surface roughness can be described as the spatial shift of the material boundary in the waveguides The shift is often considered to be constant along the waveguide height and varying along the propagation direction. The shift of the planar interface Δh at $x = x_0$, the interface between the waveguide material and cladding, and the resulting perturbation are described by

$$\varepsilon_p(\mathbf{r}) = \frac{\partial \varepsilon}{\partial h}(\mathbf{r})\Delta h(\mathbf{r}) = (\varepsilon_w - \varepsilon_s)\delta(x - x_0)\Delta h(y,z) \ . \tag{5.15}$$

With ε_w and ε_s being the permittivity of the waveguide and surrounding material, respectively. Then, the tangential and perpendicular components of the field with regard

to the interface are distinguished to conform to the interface boundary conditions. This results in the following expression for the perturbed permittivity

$$\varepsilon_p(\mathbf{r})\mathbf{E}_0(x,y) = \begin{pmatrix} \frac{\Delta\varepsilon}{\varepsilon_w\varepsilon_s}\varepsilon^2(x,y)\ \mathrm{E}_{0,x}(x,y) \\ \Delta\varepsilon\ \mathrm{E}_{0,y}(x,y) \\ \Delta\varepsilon\ \mathrm{E}_{0,z}(x,y) \end{pmatrix} \Delta h(y,z)\delta(x-x_0) \tag{5.16}$$

with the permittivity difference between the waveguide and its surrounding $\Delta\varepsilon = \varepsilon_w - \varepsilon_s$.

To simplify, only a single surface is calculated at a time, thus the perturbation is a function of (y,z) at a fixed x_0. The shift $\Delta h(y,z)$ can be statistically described by a zero-mean Gaussian process which is completely described by its autocorrelation function, the kernel $\kappa(\Delta y, \Delta z)$.

The sidewall roughness is a stationary Gaussian process, and due to this, the kernel depends solely on the distance of its arguments. In other words, the kernel defines the similarity between two neighbouring function values [31]. As the roughness in y and z can be assumed to be uncorrelated, the Gaussian process is decomposed into its subspaces and the kernel thus factors into

$$\kappa(\Delta y, \Delta z) = \kappa_y(\Delta y)\kappa_z(\Delta z)\ . \tag{5.17}$$

Melati et al. [12] found that the kernel for the 1D Gaussian process of the sidewall roughness is best described by the exponential process

$$\kappa_z(\Delta z) = \sigma^2 \mathrm{e}^{-\frac{1}{L_{c,z}}|\Delta z|} \tag{5.18}$$

with the RMS roughness σ and the correlation length L_c. The kernel in Equation 5.17 is therefore

$$\kappa(\Delta y, \Delta z) = \sigma^2 \mathrm{e}^{-\frac{1}{L_{c,y}}|\Delta y|} \mathrm{e}^{-\frac{1}{L_{c,z}}|\Delta z|} \tag{5.19}$$

with

$$\kappa_y(\Delta y) = \mathrm{e}^{-\frac{1}{L_{c,y}}|\Delta y|} \tag{5.20}$$

where σ^2 was moved to κ_z [15].

As the sidewall roughness along the waveguide height is considered constant, it can be realised by setting $\kappa_y(\Delta y) \approx 1$.

5.2.2 Calculation of the Loss Coefficient

The perturbation from the varying sidewall can be described as an imaginary current which causes the scattered field in a volume. Using this imaginary current, a radiation field is constructed, with which the radiated intensity per waveguide length is obtained from the radiation field's θ- and ϕ-components. The coupling of the scattered radiation back into the waveguide is neglected, as the backscattering was found to be negligible by Melati et al. [12]. Further simplification yields the final expression for the radiation intensity

$$\begin{aligned} u(\theta,\phi) =& \frac{\mu_0\omega^4}{32\pi^2 c_0}\pi S_z(\beta - k_z)\int_0^H \int_0^H \\ & \kappa_y(y-y')o(\theta,\phi,y,y')\mathrm{e}^{-\mathrm{j}k_y(y-y')}\,\mathrm{d}y\,\mathrm{d}y' \ . \end{aligned} \tag{5.21}$$

Where the x-integral dissolves due to the δ-distribution of the perturbation from Equation 5.16. Furthermore, assuming that the waveguide is long with regard to the correlation length in z-direction, it is possible to collect the z-dependent integrands which evaluate to the Gaussian process' z-spectrum S_z via the ergodicity- and Wiener-Kinchin therorem. As discussed in the previous chapter, the spectrum of an ACF is defined by the Fourier transform. As the zero-mean Gaussian process is completely described by its ACF, the spectrum of a Gaussian process is also defined by the Fourier transform

$$\pi S(q) \coloneqq \frac{1}{2}\int_{-\infty}^{\infty}\kappa(\Delta z)\mathrm{e}^{\mathrm{j}q\Delta z}\mathrm{d}\Delta z \tag{5.22}$$

which yields for the exponential kernel in Equation 5.18

$$\pi S(q) = \sigma^2\frac{L_{c,z}}{1+(qL_{c,z})^2} \ . \tag{5.23}$$

Due to this, only the integral over the waveguide height in y-direction remains and the overlap $o(\theta,\phi,y,y')$ is defined as

$$\begin{aligned} o(\theta,\phi,y,y') = & \begin{pmatrix} \frac{\Delta\varepsilon}{\varepsilon_w\varepsilon_s}\varepsilon^2(x_0,y)\ \mathrm{E}_{0,x}(x_0,y) \\ \Delta\varepsilon\ \mathrm{E}_{0,y}(x_0,y) \\ \Delta\varepsilon\ \mathrm{E}_{0,z}(x_0,y) \end{pmatrix} \\ & \cdot\hat{T}(\theta,\phi)\begin{pmatrix} \frac{\Delta\varepsilon}{\varepsilon_w\varepsilon_s}\varepsilon^2(x_0,y')\ \mathrm{E}^*_{0,x}(x_0,y') \\ \Delta\varepsilon\ \mathrm{E}^*_{0,y}(x_0,y') \\ \Delta\varepsilon\ \mathrm{E}^*_{0,z}(x_0,y') \end{pmatrix} \end{aligned} \tag{5.24}$$

with

$$\hat{T}(\theta,\phi) = \hat{R}^T(\theta,\phi)\hat{R}(\theta,\phi) \tag{5.25}$$

and

$$\hat{R}(\theta,\phi) = \begin{pmatrix} 0 & 0 & 0 \\ \cos\theta\cos\phi & \cos\theta\sin\phi & -\sin\phi \\ -\sin\phi & \cos\phi & 0 \end{pmatrix} \quad . \tag{5.26}$$

$\kappa(y-y')$ describes the roughness along the waveguide height and can be assumed to be 1 as a first-order approximation. The vector of the propagation coefficient $\mathbf{k}$ has the components $k_y = \sin(\theta)\sin(\phi)k$ and $k_z = \cos(\theta)k$. The integration is over the height of the waveguide H. To obtain the total radiated power per unit length, Equation 5.21 is integrated over the solid angle. The loss coefficient is therefore evaluated with

$$2\alpha = \frac{1}{P}\int_0^{\pi} \sin(\theta) \int_0^{2\pi} u(\theta,\phi)\mathrm{d}\phi\mathrm{d}\theta \tag{5.27}$$

where P is the input mode power for the corresponding z-component of the integrated Poynting vector

$$P = \frac{1}{2}\int_{-\infty}^{\infty}\int_{-\infty}^{\infty} \Re\{(\mathbf{R}\times\mathbf{H}^*)\ \cdot\hat{z}\}\mathrm{d}x\mathrm{d}y\ . \tag{5.28}$$

The factor two in front of α relates the power loss to the attenuation coefficient of the mode's fields in Equation 5.14.

The Hoermann model correctly conforms the scattered field to the boundary conditions of the waveguide's cross section using the perturbation in Equation 5.16. Additionally, the only input it requires is the roughness parameters of the Gaussian process' spectrum, the RMS roughness σ and correlation length L_c for the autocorrelation function, as well as the fields of the unperturbed mode. These fields can be calculated using simulation suits such as Ansys Lumerical and Comsol amongst others. The TE and TM fields at the interfaces provide the input for E_0 in Equation 5.24. Integration can be done using software packages such as Python′s Scipy. This will be shown in a later chapter to predict the waveguide loss for the fabricated waveguides.

CHAPTER 6

State of the Art

Silicon photonics aims to leverage decades of accumulated know-how in CMOS processing to apply it to integrated photonic applications. Advances in the fabrication of passive components, such as waveguides, enable low-loss interconnection for more complex components such as directional couplers, multiplexers and demultiplexers, as well as active components such as tunable micro ring resonators and Mach-Zehnder modulators. The low absorption loss in the infrared band between ∼1.1 µm and ∼1.6 µm positions silicon as an interesting material for telecom communication applications, with SiGe photodetectors and in-package lasers in transceivers [32].

There are two commonly used measurement methods to determine the waveguide losses. One is the cutback method where the light is coupled into the waveguide via edge coupling and coupled out via edge coupling of the chip facets. The light intensity is measured at the exit for multiple waveguide lengths to determine the loss in dB/cm via the slope of a linear regression through the measured transmissions. The offset of the linear fit can be used to determine the total in- and outcoupling loss. Its advantage is that it has a relatively simple design as the only requirement is multiple waveguides of different length. The significant drawback is that variations in the local topography of the facet around each measured waveguide influences the measurement and results in higher uncertainty of the linear fit. If the facets are too rough, the coupling loss might be too high, which may make measurements impossible.

The other method is by using ring resonator structures, a simple example is depicted in Figure 6.1. The resonator is designed to be in resonance at the desired wavelength, this resonance depends on factors such as the gap between the waveguide and the ring [33].

To obtain propagation losses, the quality factor Q is estimated by measuring the

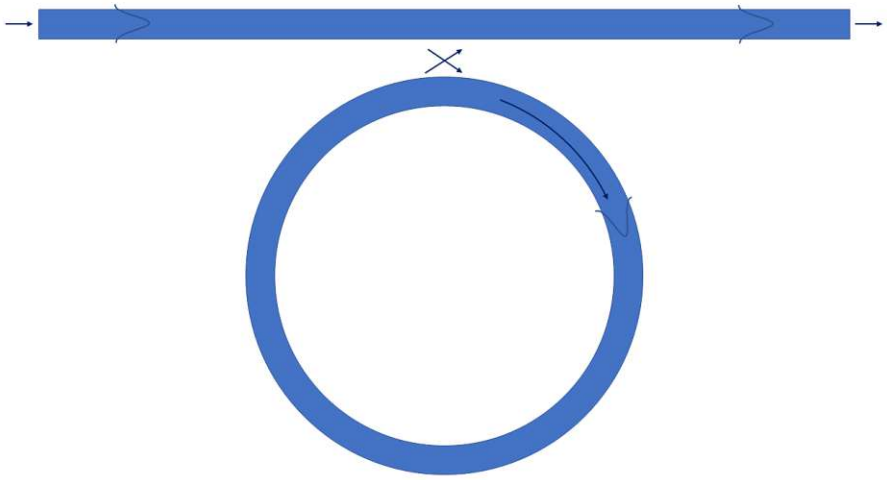

Figure 6.1: Schematic layout of a single ring resonator. The waveguide on top acts as a bus line to the resonator. At the designed wavelength the coupling into the ring is at a maximum, the ring is in resonance [33].

transmission spectra of the ring cavity to obtain the linewidth of the resonator (FHWM), which allows for estimation of Q. Using the quality factor, the loss of the ring can be calculated using the following Equation [33]

$$\alpha_{ring} = \frac{2\pi n_g}{Q\lambda_0} = \frac{\lambda_0}{Q \cdot R \cdot FSR} \quad . \tag{6.1}$$

Where λ_0 is the free space wavelength, FSR the free spectral range, Q the quality factor, n_g the group index, and R the radius of the ring resonator. The main advantage compared to the cutback method is the independence of the edge surface, as the loss depends only on Q and FSR that are not influenced by the edge. One drawback of this measurement method is that the transmission spectra strongly depend on the gap between the bus line and the ring, the geometry of the structure, and the radius of the ring. Thus, careful simulation and calculation must be performed in advance if an accurate determination of the propagation loss is desired. Furthermore, a small-bandwidth frequency-tunable laser is needed for the characterisation [33][34][35].

An alternative to silicon photonics is silicon nitride, which it the focus of this thesis, as it exhibits low absorption for a wide spectral range of ∼400 nm to ∼4 µm [36]. This enables the usage of PICs in areas such as medical diagnostic tools [1], gas sensing [2][37], broadband, high-efficiency photodetectors [3], and trapped-ion quantum computing [6][38], among others. Significant advancements have been made to achieve ultra-low-loss waveguides.

Roeloffzen et al. [39] employed double-core and BOX-shaped structures to achieve losses as low as 0.1 dB/cm for a wavelength of 1550 nm.

Single-layer waveguides have reduced thicknesses down to 40 nm to reduce roughness-induced sidewall scattering to achieve low losses of around 0.1 dB/m for the fundamental TE mode at telecom wavelengths of 1550 to 1600 nm. The drawback is that the bending radii are as high as 10 mm to prevent bending and mode mismatch losses as shown by Puckett et al. [40]. They also mention that increasing the thickness reduces the required bending radius to achieve minimal bending-induced losses, with the added drawback that material and scattering-induced losses increase, due to the different shape of the mode.

Bose et al. [41] demonstrated 6 µm wide and 80 nm thick LPCVD SiN waveguides with TEOS SiOx upper caldding and thermal SiOx lower cladding. The lowest loss was measured for the TE mode at a wavelength of 8.66 dB/m at 1581 nm.

Roberts et al. [42] proposed a method to measure the roughness of the sidewalls, as depicted in Figure 6.2. They measured sidewall roughness values between 0.53 and 2.83 nm and correlation lengths between 47.4 and 145.6 nm, depending on the lithography method used and the etch recipe. They reported losses of 730 nm thick resonator rings of radius 115 µm for a wavelength of 1560 nm. The largest loss was measured for the 1.2 µm wide ring at 5.02 ± 0.38 dB/m, with the smallest losses for the 5 and 10 µm rings at 1.29 ± 0.29 and 1.27 ± 0.25 db/m respectively. They proposed a modified Payne-Lacey scattering loss model to calculate the impact of the shift in waveguide mode due to different bending radii on the scattering loss, by introducing an additional factor η into the Payne-Lacey model. This correction factor is the ratio of the mode overlap of the bending mode field to the mode overlap of the waveguide.

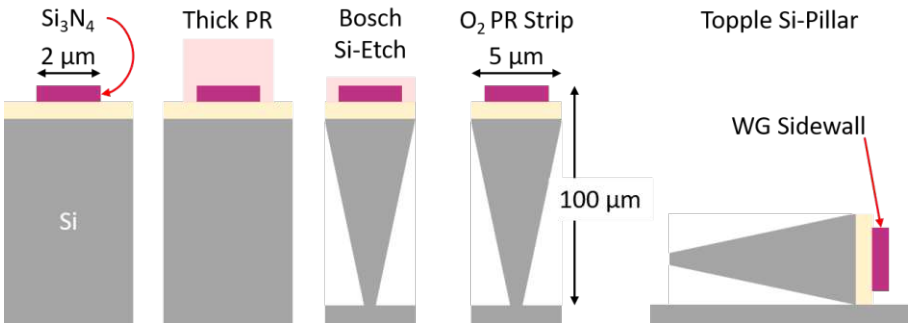

Figure 6.2: Schematic process of the fabrication of a waveguide (WG) pillar for sidewall measurements. After structuring the waveguide on top of the SiOx cladding, a protective photoresist (PR) is deposited to protect the waveguide during the subsequent Bosch etch of the underlaying Si. Afterwards the PR is stripped in using O_2 plasma and the pillar is toppled using a tungsten microelectrode probe. The waveguide can now be easily accessed using the AFM [42].

Roberts et al. [42] argue that this direct measurement has a higher precision than inferring the roughness from stitched grey scale SEM images, as was done by Yap et al. [28], as the resolution of a SEM is normally in the range of tens of nanometres, while the resolution limit of an AFM is in the range of Angstroms. The measured roughness and

correlation lengths for three different processes are listed in Table 6.1. Using an electron beam lithography significantly improves the roughness as a result of the better resolution of the process. The change in etch recipe resulted in a low-polymer etch for the same DUV process.

Lithography	**Etch Recipe**	R_q **[nm]**	$L_{c,z}$ **[nm]**
DUV	CHF_3/O_2	2.83	96.0
DUV	$CHF_3/O_2/N_2$	1.23	145.6
Electron-beam	CHF_3/O_2	0.53	47.4

Table 6.1: RMS roughness R_q and correlation length along the propagation axis $L_{c,z}$ for different etch recipes and lithography methods [42].

For quantum computing and information applications [6][38], as well as certain sensing applications [1][37] the visible spectrum is of interest, as opposed to communication applications where wavelengths of ∼1.3 to 1.6 µm are used.

Sorace-Agaskar et al. [43] reported losses for LPCVD SiN using cutback measurements in the near UV to infrared range. The waveguides for this range were 100 nm thick and 250 nm wide for wavelengths of 405-458 nm, 500 nm wide for a wavelength of 634 nm, and 1100 nm wide for a wavelength of 1092 nm. They fabricated a chip with two SiN layers, one for incoupling via the facet, where the mode is then transferred to the second layer by evanescent coupling, and measured the losses in both TE and TM polarisation. Their results are depicted in Figure 6.3, where a lower loss for TM polarisation is visible, which is likely due to the dominant mode overlap with the smoother top and bottom surfaces, as opposed to the TE mode, where the field of the mode is concentrated at the sidewalls. They also measured the sidewall roughness and found a value of 1.54 nm for a correlation length of 30 nm. Figure 6.3 also shows the predicted scattering loss, which was obtained using the Payne-Lacey model. The predicted scattering loss for TE is overestimated for a wavelength range of ∼500-800 nm and underestimated for wavelengths below ∼500 nm. The predicted scattering loss for the TM mode fits well for wavelengths above ∼500 nm and is underestimated for wavelengths below ∼500 nm. Due to the relatively low thickness of 100 nm and wider waveguides for longer wavelengths, the Payne-Lacey model exhibits a good fit for wavelengths above 600 nm.

Chauhan et al. [44] demonstrated 20 nm thick LPCVD SiN waveguides on PICs for integrated atomic, molecular and quantum photonics. They calculated the waveguide loss by measuring the Q factor of the resonator rings. The widths of the resonator rings for TE modes are chosen such that quasi-single mode operation is ensured, they are thus 1.3 µm wide for a wavelength of 461 nm and 2.3 µm wide for wavelengths of 674, 698, and 802 nm. The TM is filtered out by choosing the appropriate bending radii. Propagation losses of 0.09, 0.01, 0.01, and 0.02 dB/cm were measured, with the loss corresponding to the wavelengths above in order of increasing wavelength.

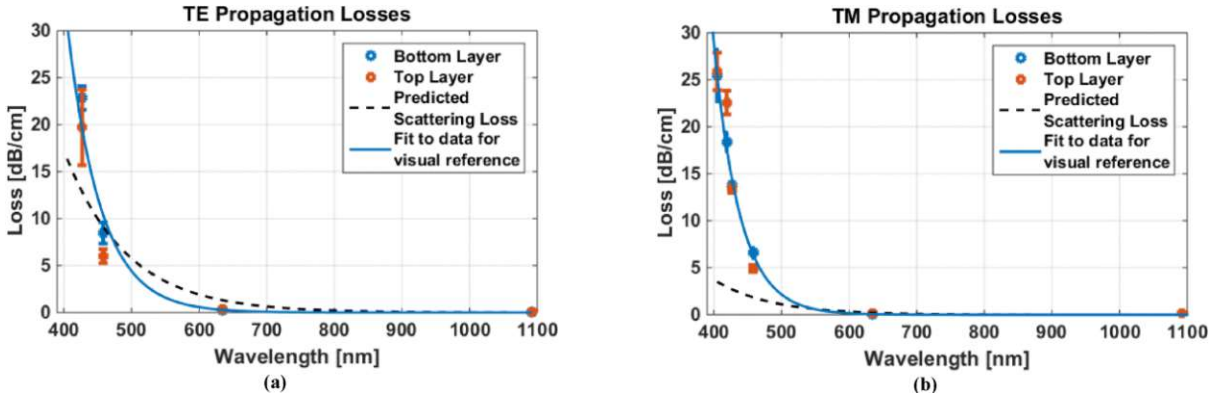

Figure 6.3: a) TE and b) TM propagation loss for top layer (orange) and bottom layer (blue) with exponential fit (blue line) and scattering loss fit using the Payne-Lacey-model (dashed line) [43].

Zanarella et al. [13] also employed resonator rings to calculate the losses of 275 nm thick LPCVD SiN waveguides. They measure rings of varying width and radius over a wavelength range of 461 to 780 nm. The different waveguide widths range between 400 and 4000 nm and the bending radii between 30 and 300 µm. Using ellipsometry, they obtained refractive indices and absorption coefficients of their thin films. Using the measurements, they separated absorption losses from scattering losses by calculating the confined power in the waveguide, as seen in Equation 5.1, and employed the Payne-Lacey model to fit the sidewall roughness and correlation length. This results in a fitted sidewall roughness of 1.5 nm with a correlation length of 90 nm. They show that for the fundamental TE mode, the loss decreases from ∼1 dB/cm for 500 nm wide rings with a radius of 55 µm to ∼0.01 dB/cm for 4000 nm wide rings with a radius of 300 µm, as shown in Figure 6.4. They attribute this decrease to a lower overlap of the waveguide mode with the sidewall, thereby minimising the influence of the scattering loss. They further show that, depending on the wavelength, the losses in the waveguide are either dominated by absorption or by surface scattering.

Smith et al. [34] fabricated resonator rings with 150 nm thick SiN. They used Q factor measurements to calculate propagation losses for a width of 500 nm and a radius of 110 µm in a wavelength range of 400 to 1000 nm for both TE and TM polarisation. They achieved mean propagation losses for all tested chips of ∼4 dB/cm and ∼2.5 dB/cm at a wavelength of 400 nm for TE and TM respectively. At a wavelength of 700 nm the mean propagation losses of all tested chips are ∼1.3 dB/cm and ∼0.7 dB/cm for TE and TM respectively, while at 1000 nm the mean propagation losses for all chips are ∼1 dB/cm and ∼0.3 dB/cm.

Silicon nitride is not the only candidate for guiding light in the visible spectrum on chips, the high absorption losses for SiN in the UV range are especially limiting for wavelengths below 400 nm.

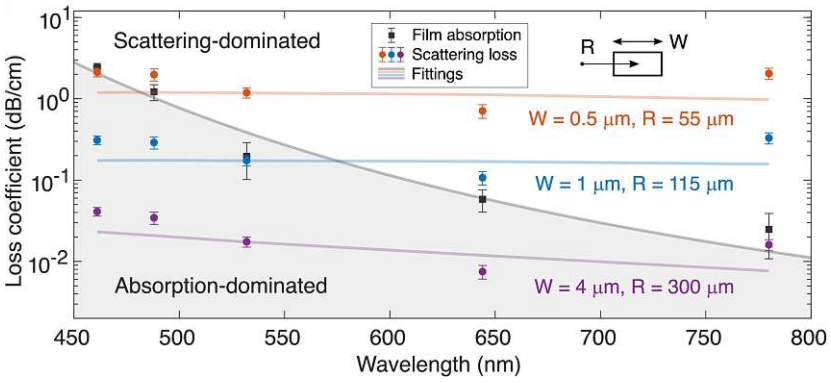

Figure 6.4: Dependence of the waveguide loss on wavelength; Increasing the width (W) and radius (R) leads to a decrease in waveguide loss, thereby moving from an absorption-dominated area into a scattering-dominated area. Using the film absorption measurement (black squares) the scattering is calculated from the total loss [13].

Single-crystalline aluminium nitride (AlN) is a promising material for UV waveguiding, as its large bandgap of ∼6.2 eV results in a transparent window starting at wavelengths of 200 nm. Furthermore, AlN exhibits an intrinsic $\chi^{(2)}$ susceptibly, which makes it interesting for non-linear interactions [36][35]. Liu et al. [35] fabricated ring resonators from a 500 nm thick single-crystalline AlN film. For a width of 800 nm and radius of 30 µm, they achieved losses of ∼8 dB/cm at a wavelength of 390 nm for TE polarised light using ring resonators of 800 nm width. For TE polarised light at a wavelength of 455 nm, the loss is reduced to ∼3.5 dB/cm. They argue that the increased loss stems from scattering at rough sidewalls, as wider waveguides exhibit smaller losses.

Aluminium oxide (Al_2O_3) has a reported electrical bandgap of 5.1 to 7.6 eV, depending on the deposition method used, translating into transparent windows starting from 163 to 243 nm [45] [36]. West et al. [45] used Atomic Layer Deposition (ALD) for 100 nm thick Al_2O_3 films with high uniformity and low defect densities. Their measurements showed a refractive index of 1.65-1.72 in the visible to NUV spectrum, which is higher than the surrounding SiOx ($n \sim 1.45$) but significantly lower than that of SiN ($n \sim 2$). They fabricated 600 nm wide waveguide structures for cutback measurements and achieved losses of 3.12 dB/cm and 2.89 dB/cm for both TE and TM polarised light of 371 nm. For 405 nm light, their measurements showed a propagation loss of 1.77 dB/cm (TE) and 1.35 dB/cm (TM). They argue that the difference in loss is due to the different interaction with the waveguide sidewalls for different polarisations.

Another promising material stack was recently shown by Jaramillo et al. [46], which proposed a hafnium oxide (HfO_2) aluminium oxide (Al_2O_3) stack for low absorption losses in a wavelength range of 400 to 650 nm. They deposited HfO_2 and Al_2O_3 films using ALD with a layer periodicity P, whereas each period consisted of $(1-x)P$ layers of Al_2O_3 followed by xP layers of HfO_2. Films between 80 and 100 nm thickness were grown in this way and ellipsometry measurements showed that a period of 3 yields the lowest film losses.

They provided a comparison of measured refractive indices n and extinction coefficients k for Si_3N_4, HfO_2, Al_2O_3, SiO_2 and their HfO_2/ Al_2O_3 film with period 3, shown in Figure 6.5

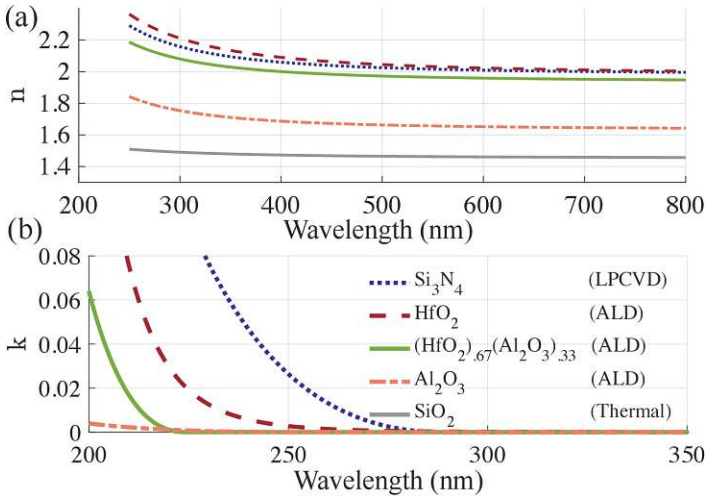

Figure 6.5: Measured a) refractive index n and b) extinction coefficient k for commonly used materials in PICs. The ellipsometry does not resolve k-values $\ll 0.002$ [46]. Note that extinction coefficient values as low as 0.002 for $\lambda = 405$ nm equate to $\alpha \approx$6200 dB/cm, see Equation 3.8.

Waveguides of varying width were measured using the cutback method to determine waveguide losses. For TE polarised light of $\lambda = 375$ nm, a loss of ∼8 dB/cm was measured for a 300 nm wide waveguide. The same waveguide shows a loss of ∼5 dB/cm for TE polarised light of $\lambda = 405$ nm [46].

In summary, SiN waveguides show low losses, ∼0.1-0.01 dB/cm, in both infrared and visible spectra for low-confinement structures, where most of the mode's power is guided in the cladding material. Multiple publications identify scattering at the sidewalls as the main contribution to total propagation loss. Wide and thin waveguides have the advantage of low loss, around 0.1-0.01 dB/cm, because the waveguide mode exhibits a reduced overlap with the sidewall but has the significant drawback of large bending radii of >300 µm to efficiently guide light in the PIC, resulting in increased chips sizes. Furthermore, estimations of the sidewall roughness statistics were made by fitting the loss to the Payne-Lacey model, which displays bad agreement for waveguides of <1000 nm as well as wavelengths below ∼500 nm for waveguides above 500 nm width. Sidewall measurements involve either elaborate sample preparation to access the sidewall directly for AFM measurements or were done by inferring the sidewall roughness via SEM images, which has a lower precision for smaller roughnesses.

CHAPTER 7

Material Losses

In Chapter 3 the frequency dependence of the refractive index and the absorption coefficient was explained. Measurements, as seen in [13] and [46], show that for SiN material losses for wavelengths toward the UV regime start to become increasingly larger, thus it cannot be disregarded for the efficient guiding of light in PICs. Ansys Lumerical uses the refractive indices of SiN from the Handbook of Optical Constants of Solids [36] but does not include the absorption coefficient for SiN. To obtain profiles for the SiN used in this thesis and compare it with the SiN data from [36], my colleague Arie McOnie and I measured the refractive index and loss using the Metricon 2010/M prism coupler for the optical characterisation of thin films at multiple wavelengths. To facilitate this, 400 nm of LPCVD SiN was deposited on 2.3 µm of thermal SiOx to enable guided modes in the SiN thin film, the need for this is described below.

7.1 Optical Characterization of SiN

The Metricon 2010/M prism coupler uses the optical tunnel effect to couple coherent light into the thin film using a prism. For measurements of the refractive index and film thickness, part of the light couples into the thin film at certain angles between thin film and prism, which cause dips in the measured intensity at the photodetector on the outcoupling side of the prism, shown in Figure 7.1a. To measure the loss of the film, the propagating mode is then measured using a fibre, which travels along the slab waveguide capturing the out-scattered light at the surface as a function of length, as seen in Figure 7.1b [47].

The results of these measurements are depicted in Table 7.1. It is apparent that both

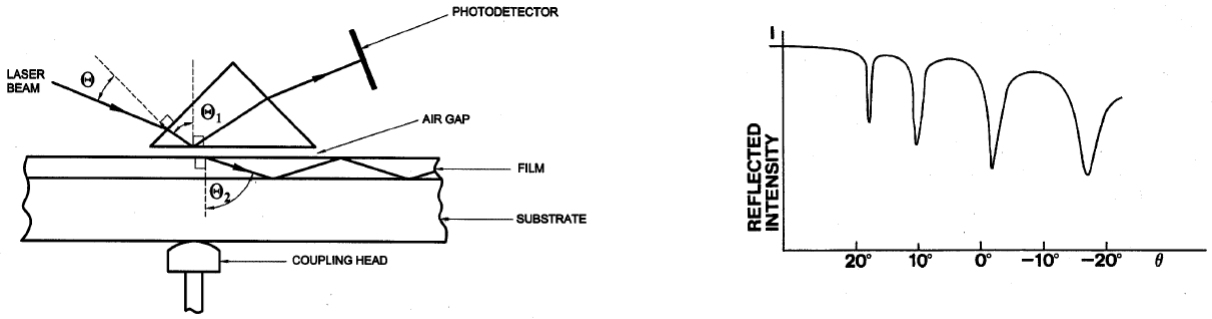

(a)

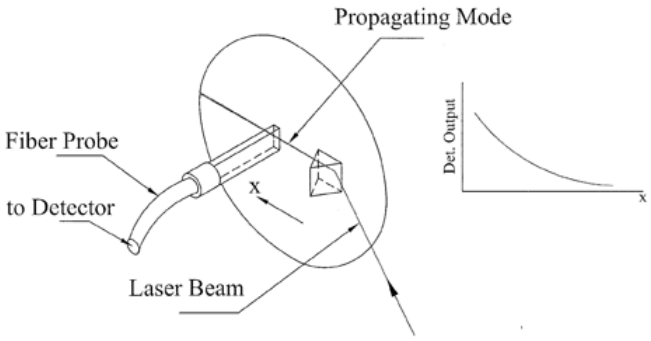

(b)

Figure 7.1: Principle of a) Refractive index measurement and b) Loss measurement in a Metricon prism coupler [47].

the refractive index and the loss increase exponentially for shorter wavelengths. This is the Urbach tail as explained in Chapter 3.4.

Wavelength [nm]	**RI [1]**	**Loss [dB/cm]**
375	2.073±0.001	9.83±5%
405	2.059±0.001	5.17±5%
457	2.038±0.001	1.53±5%
488	2.028±0.001	0.36±5%
515	2.022±0.001	0.16±5%
633	2.003±0.001	0.12±5%

Table 7.1: Measured refractive index (RI) and bulk loss at different wavelengths with the Metricon 2010/M prism coupler.

7.2 Modelling of the Optical Properties in SiN

As seen in the previous section, both refractive index and loss increase exponentially with decreasing wavelength, where our data matches well with the data given in [36], but there a much broader energy range was covered, providing measurement points down to the

XUV wavelength of 50 nm, which is not possible with the prism coupler. Thus, it is of interest to extend the range of the measured data points by fitting and comparing the Tauc-Lorentz and Tauc-Lorentz-Urbach model from Chapters 3.3 and 3.4 respectively, as well as a simple exponential fit of the data to see which model fits best. The exponential fit describes the behaviour of the dielectric functions in the region of the Urbach tail, as explained in Chapter 3.2, but is certainly inaccurate for wavelengths below this region. It is also of interest to compare our data to that of Palik's Handbook of Optical Constants of Solids [36], to see if the refractive indices used for the simulation of waveguides in Lumerical's MODE fit the fabricated waveguides and if the extinction coefficient of the materials are similar.

All three fits under consideration were implemented using the Python scipy optimze library. To accurately fit the models, the measured loss, which is provided in dB/cm, was converted into the extinction coefficient κ using the following equation:

$$\kappa(\lambda) = \frac{\alpha(\lambda)\lambda}{4\pi} \ . \tag{7.1}$$

With the absorption coefficient α and the wavelength λ. The refractive index and the extinction coefficient can now be used to obtain the complex permittivity $\tilde{\varepsilon}$ using the rewritten system of Equations 3.4 and 3.5. For the exponential fit, the function $a\exp(-(xb)+c)$ is used to model the decreasing refractive index and extinction coefficient for increasing wavelengths.

Using the complex permittivity, a fit of the TL-an and TLU-an functions is performed, with the parameters obtained as follows

Model	**A [eV]**	**E_0 [eV]**	**E_g [eV]**	**C [eV]**	**a [eV]**	**E_c [eV]**
TL-an	200.02	9.01	5.72	1.11	0.00025	-
TLU-an	256.41	8.10	5.26	5.94	0.00014	5.69

Table 7.2: Resulting parameters from fit for TL-an and TLU-an models.

The refractive index is fitted using the exponential function described above and yields the following parameters

Function	**a**	**b**	**c**
n	0.91	6232909	1.99
κ	$1.386 \cdot 10^4$	$2.323 \cdot 10^7$	0

Table 7.3: Resulting parameters from the exponential fit.

Using these fit values to calculate the fits for refractive index and extinction coefficient yields the following results:

Figure 7.2 shows the functions of the fits obtained over a large wavelength range from 50 to 1000 nm. The exponential fit is restricted to a wavelength range of 375 to 730

nm, as it is likely to deviate strongly for wavelengths below the measured 375 nm data point. The TL-an fit deviates significantly for both n and κ while the TLU-an fit is closer to the measured n data, while deviating significantly for κ, which is clearly visible on the logarithmic scale. Even though the validity of the exponential fit is restricted to the above-mentioned spectrum, it provides the most accurate fit.

The measured data points for SiN from Palik's Handbook of Optical Constants of Solids [36] are also fitted using the TLU model and compared to the fit of our SiN, as shown in Figure 7.3.

Although fewer points are available from the prism coupler measurement, good agreement with the refractive index data from the Handbook of Optical Constants of Solids [36] is observable, indicating that the simulated waveguide in Ansys Lumerical should be similar to the fabricated waveguides in terms of mode shape. Furthermore, our measurements provide values for the extinction coefficient κ in the visible to near-IR wavelength region, which was not available in [36].

Lastly, the obtained extinction coefficients are used to calculate the bulk loss expected by the fits. This is done with the assumption that the whole mode is contained in the film. If the mode is not contained exclusively in the film, the loss caused by the film can be calculated with the Equation 5.1. The results for the bulk loss are shown in Figure 7.4.

Figure 7.4 emphasises the point stated above that the extinction coefficient is overestimated in the TL-an and TLU-an fits. With the current fit parameters, significant loss should be observed even for infrared wavelengths. Even an increased number of data points, as in the case for the fit with Palik's data, does not result in a better fit. A possible explanation for this is that the fits for n and κ are done by first fitting the imaginary part of the permittivity ε_r'' and calculating the fit functions for n and κ from the fit function for the complex permittivity $\tilde{\varepsilon}_{r,an}$. Small deviations from the data caused by the fit of the permittivity function might not be significant for the refractive index but, due to the large difference in scale, have a large impact on the extinction coefficient. A better fit might be achieved by rewriting the Equations 3.11 and 3.15 for n and κ to fit each function separately. The exponential fit on the other hand models the real loss well, with some deviation around 500 nm, thus it is justified to use the values from the exponential fit to estimate the material loss in the waveguide simulations, as will be shown in Chapter 11.

In conclusion, it was shown that a fit of the SiN used in this thesis with the TL-an and TLU-an models, as detailed in Chapter 3 is possible with the measured data using a prism coupler. The resulting refractive index fit is best for the exponential model, although the TLU-an yields sufficient results, while the TL-an model shows a significant deviation. Both models overestimate the extinction coefficient, and even more data points for the fit do not provide sufficient accuracy. Furthermore, the data from SiN in this thesis closely match the data from Palik [36] which is used for the refractive index in waveguide simulations, which means that there are no expected differences in terms of the

modal behaviour in the waveguide. The bulk losses are best described by the exponential fit, especially in the wavelength region of interest.

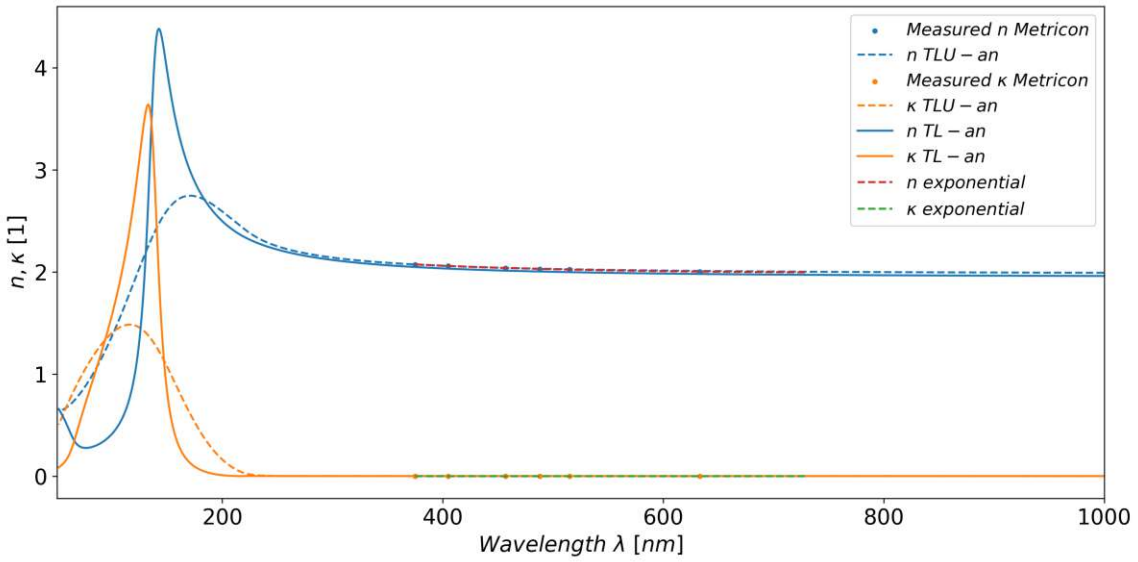

(a)

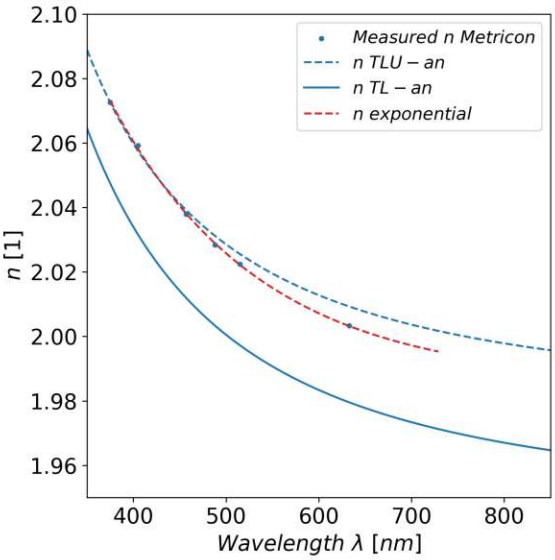

(b)

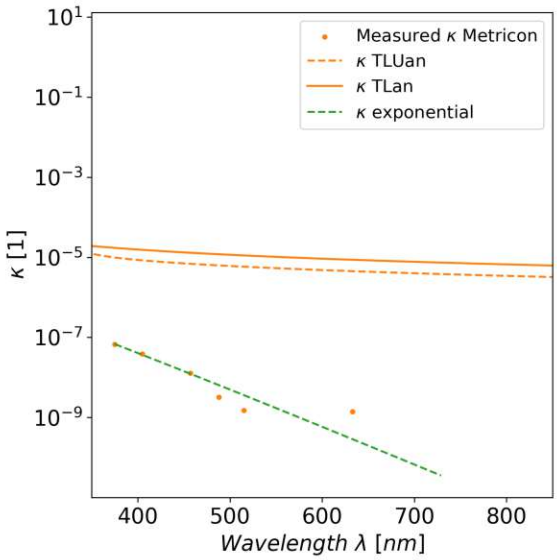

(c)

Figure 7.2: (a) Refractive index (blue) and extinction coefficient (orange) for the TL-an (dotted) and TLU-an (solid) models over a wavelength range of 50 to 1000 nm. The exponential fit (dotted) of the refractive index (red) and extinction coefficient (green) is in the wavelength range of 375 to 730 nm. Magnified view of (b) the refractive index and (c) the extinction coefficient on a logarithmic scale in the visible to near-IR wavelength spectrum.

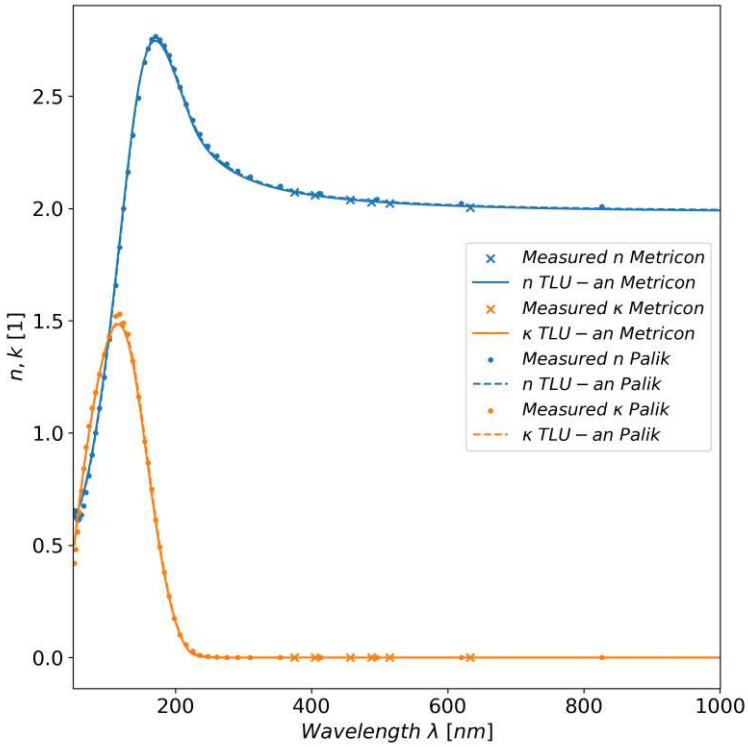

(a)

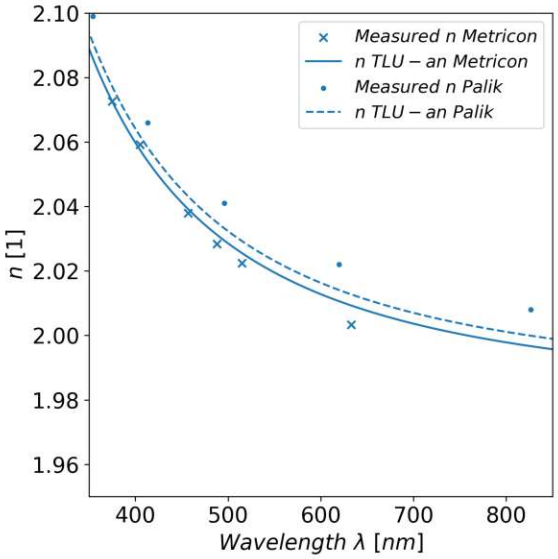

(b)

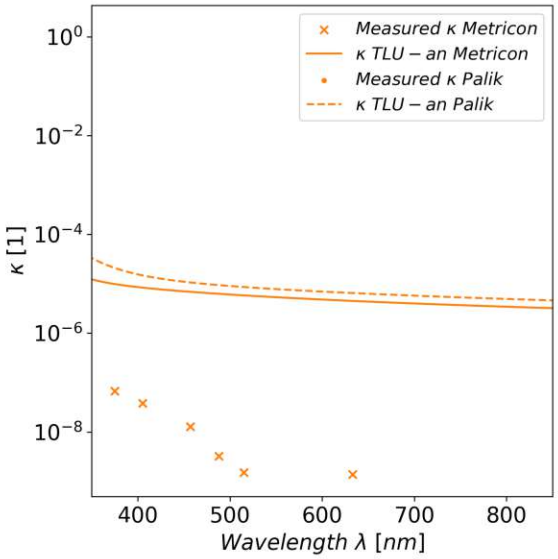

(c)

Figure 7.3: (a) Refractive index (blue) and extinction coefficient (orange) for the TLU-an models of the SiN used in this thesis (solid) and from Palik's collection [36] (dotted) over a wavelength range of 50 to 1000 nm. Magnified view of (b) the refractive index and (c) the extinction coefficient on a logarithmic scale in the visible to near-IR wavelength spectrum, note that Palik's data is not shown in this plot as no data for the extinction coefficient is available, hence they are assumed to be zero for fitting purposes. The data points for the fit from the Metricon measurement are shown as crosses, while the data points from Palik are dots.

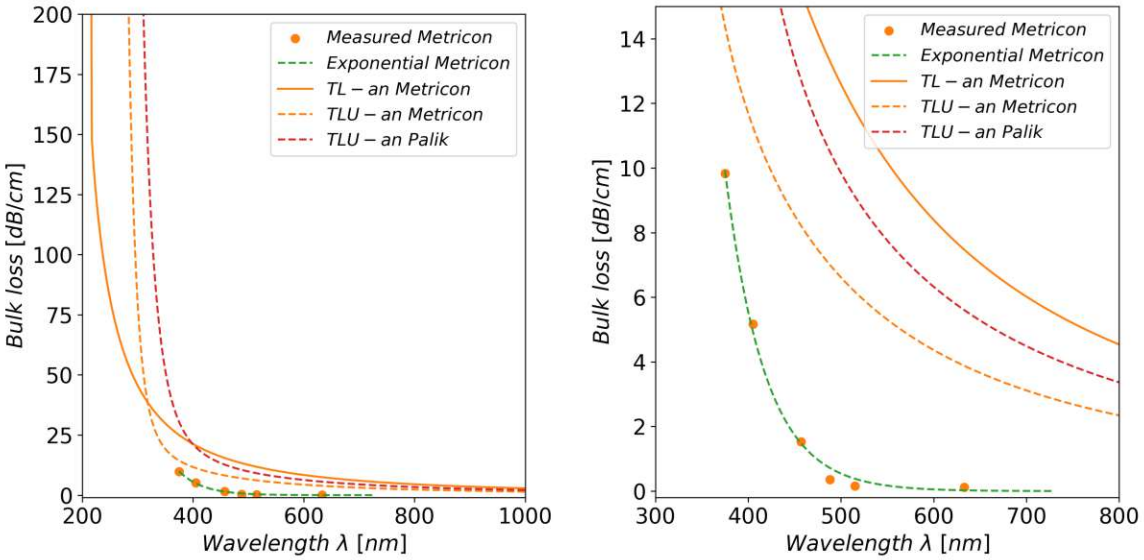

(a) (b)

Figure 7.4: (a) Comparison of the bulk loss of TL-an (orange, solid), TLU-an (orange, dotted), and exponential (green, dotted) models with data measured using the Metricon and bulk loss from TLU-an fit of Palik's [36] data (red, dotted) over a wavelength range of 200 to 1000 nm. (b) Magnified view of (a) for the loss over the visible spectrum of 300 to 800 nm, closer to the wavelengths of interest in this thesis.

CHAPTER 8

PIC Design

As both the propagation loss of the waveguides due to material and scattering losses, as well as a direct measurement of the sidewall roughness are of interest, the design of the PIC must incorporate both. The full PIC is shown in Figure 8.1 and the design of the structures will be explained for the remainder of this chapter.

Figure 8.1: Design of the PIC used in this thesis.

8.1 Waveguides

The waveguides were designed to operate in single mode for a wavelength range of 493 to 729 nm with an additional waveguide for 1763 nm, which was not used in this thesis. All waveguides were simulated using Ansys Lumerical MODE and resulted in a set of three waveguides of widths 250, 300 and 500 nm with a thickness of 170 nm. In FDTD simulations, crosstalk above 10^{-5} dB between any two waveguides with a distance of 15 µm between each other and over a length of 50 µm was excluded for the chosen wavelength range. To obtain a longer propagation distance over the limited chip area, the waveguides must incorporate multiple bends, which were simulated using Ansys Lumerical MODE and showed a large mode overlap between the straight and bent mode of 99.9% at the wavelengths for single mode operation, which equals a loss of 0.0043 dB, for a bending radius of 150 µm. This overlap shows that the mode inside the bent portion of the waveguide closely resembles that of the straight waveguide, which results in negligible losses due to conversion of the mismatched modes and additional scattering in the bends. A large mode mismatch, resulting from small bending radii, means that the mode in the bend is strongly shifted, as can be seen in Roberts et al. [42]. The worst case radiative loss from this bend radius occurs for the 250 nm wide waveguide with 729 nm light and is $4.78 \cdot 10^{-5}$ dB/cm according to the Lumerical simulation. Figure 8.2 shows a closer view of the waveguide structures, with the inset showing the evenly spaced set of three waveguide widths, with a gap of 15 µm. The chosen lengths of the waveguides are 30, 40, 60, 80 and 100 mm to enable the measurement of the waveguide loss via the cut-back method, which was explained in Chapter 6. Structures on the left and right sides are duplicates, and the chip can be separated into two along the middle to measure waveguide lengths of only half length.

8.2 Sidewall Roughness Measurement Structures

As the direct measurement of the sidewall roughness is also of interest, additional test structures were designed to facilitate AFM measurements as much as possible. Roberts et al. [42] showed a possible approach, but it is coupled with an additional fabrication effort. To keep preparation simple, the idea is to simply cleave the chip as close as possible to a waveguide, flip the chip with the cleaved facet facing the AFM needle and measure over the sidewall using the AFM, as depicted in Figure 8.3.

To increase the probability of finding a portion of a measurable sidewall, an array of curved structures was designed such that a possible misalignment between lithography and substrate crystal axis, which would result in straight structures being at an angle of the cleave line which follows the crystal orientation of Si, would still result in a measurable area. The total width of the arrays is 2 mm and the length is 10 mm with the distance

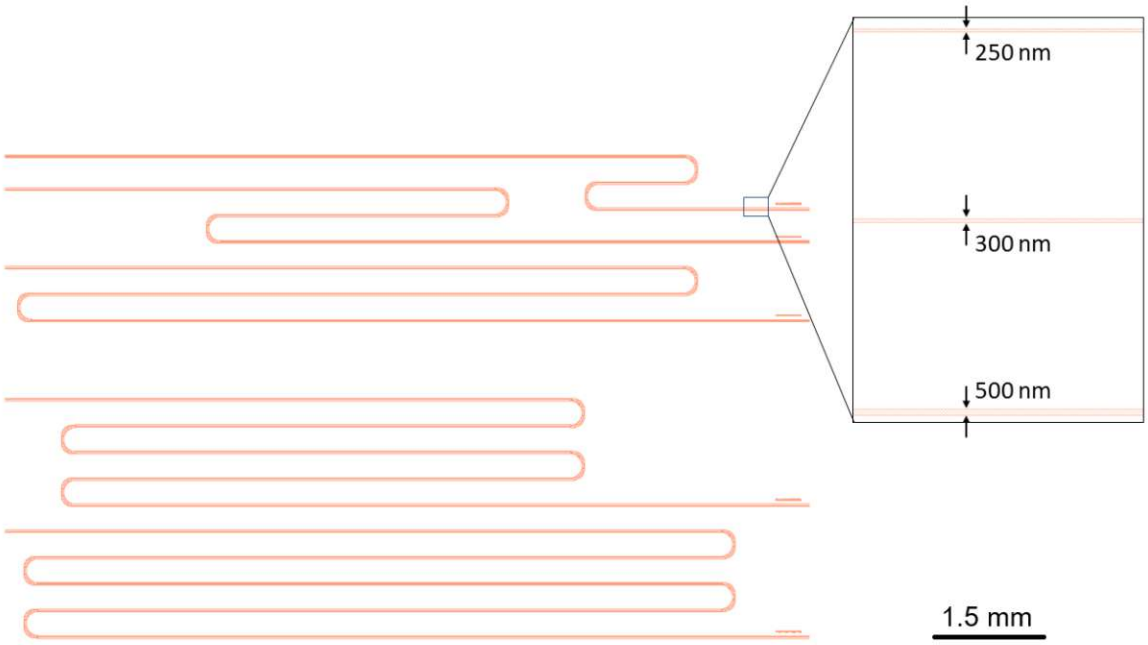

Figure 8.2: One half of the cut-back waveguide structures, with the inset showing the three waveguide widths each separated by a 15 µm gap.

between each single test structure being 5 µm. The structures are shown in Figure 8.4. The complete test structure array is visible in Figure 8.1, while 8.4 shows the alignment structure for cleaving on the left as well as three arrays of the bent structures. The width is repeatedly varied between the three waveguide widths used for the cut-back waveguides. Although this does not add any benefit to sidewall measurements, because the roughness is expected to be independent of the waveguide width, it allows easier detection of significant overetching during the fabrication process of the different waveguide widths.

8.3 Crosstalk Structures

The crosstalk of the waveguides for the cut-back measurements must be avoided to ensure accurate measurements, but the simulation of the waveguides in Ansys Lumerical FDTD is limited due to the large computational task of simulating long distances. Because of this, 250 nm wide waveguides were placed at decreasing gap sizes beside each other. The gaps are 10, 7, 5, 3, 1, and 0.5 µm. For longer wavelengths, crosstalk will be observable for larger gaps than for shorter wavelengths.

However, crosstalk can be exploited for directional coupling where the power of one waveguide can be deliberately coupled into another. The power coupling ratio in the second waveguide can be calculated using the following equation

$$P_2(L) = P_0 \sin^2\left(\frac{\pi L \Delta n}{\lambda_0}\right) \tag{8.1}$$

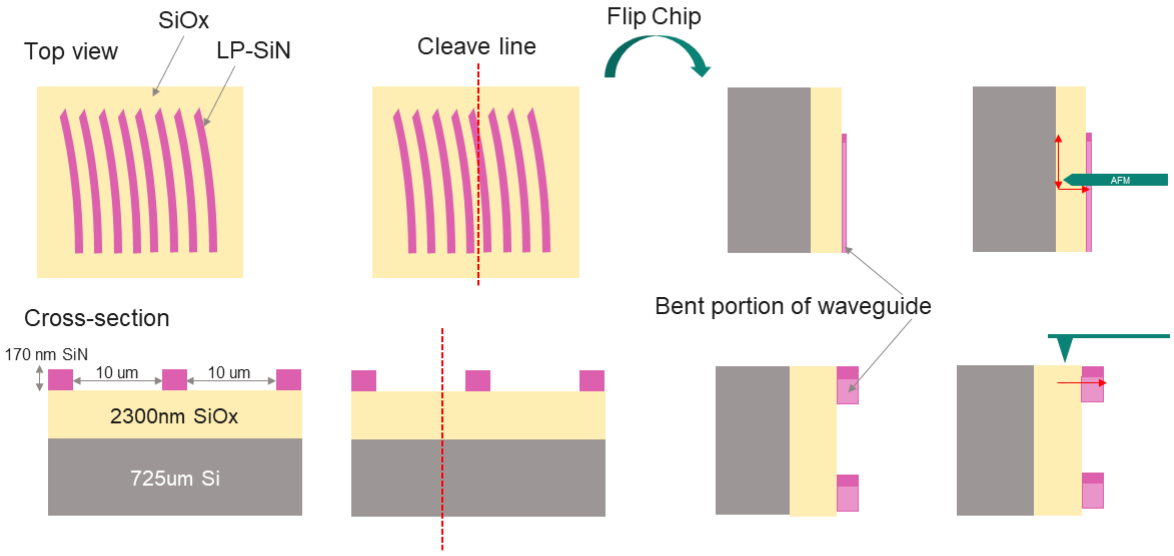

Figure 8.3: Schematic process description of the sidewall AFM measurement. First the chip is cleaved along the middle of the test structures, then flipped such that the facet is facing upwards. Then the sidewalls can be measured using an AFM.

where P_0 is the initial power in waveguide 1, Δn is the difference between the effective refractive index of the mode in waveguide 1 without the coupling structure and the mode in the coupling structure. λ_0 is the vacuum wavelength, and L is the length of the coupler [48]. The effective refractive index difference implies that the coupling is strongly dependent on width, distance, and wavelength.

These directional couplers have been realised to transfer ratios of 30/70, 50/50 and 0/100 for a wavelength of 729. 532, and 493 nm. One such directional coupler for a 50/50 split at 493 nm is shown in Figure 8.5.

8.4 Bent Waveguides

As mentioned above, small bending radii can result in radiative losses. To characterise the loss due to bends, waveguides were designed which have equal total length and equal bending radius but differing amounts of bends. If the loss due to bends is large, a higher amount of bends should result in a measurable reduction of the transmitted light. Instead of measuring the loss over different waveguide lengths in the cut-back method, the loss for different amounts of bends can be fitted to estimate the bending loss. For infrared light, separate bending loss structures have been placed in the bottom right section in Figure 8.1. The bending radii are 50, 75, and 100 µm where each radius has structures with 10,

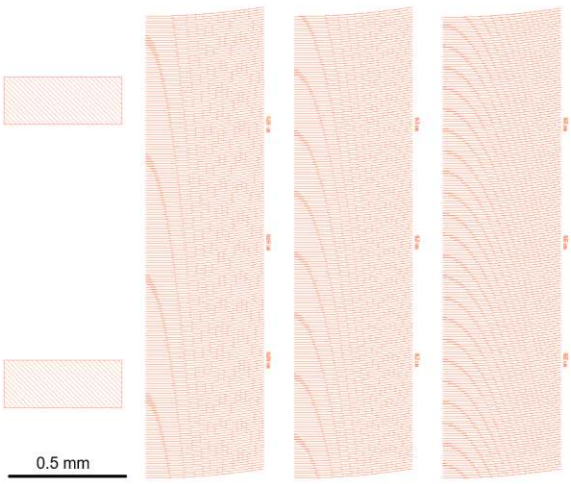

Figure 8.4: Close up of the bent sidewall roughness measurement structures. On the left are the alignment structures for cleaving, with three arrays of the three waveguide widths on the right of the alignment structures.

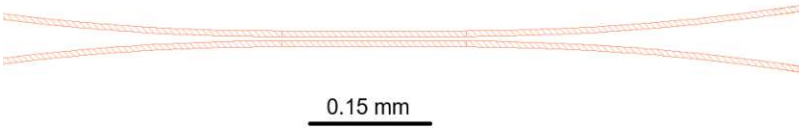

Figure 8.5: Close up of the directional coupling structure for 50/50 coupling of 493 nm laser light. The coupling length was calculated to be 8.1 µm.

20, 30, and 40 bends. The 50 µm radius bending loss structures are depicted in Figure 8.6.

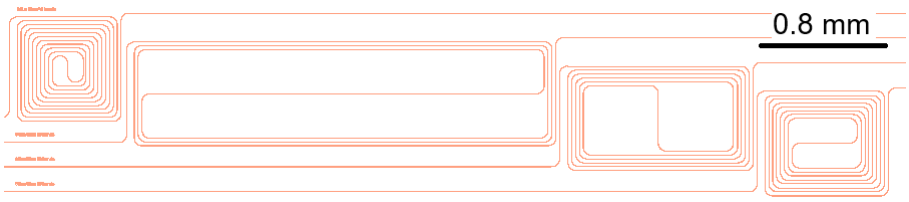

Figure 8.6: Structures for estimation of the bending losses with different amount of bends but total length.

Although the crosstalk and bending structures are included in the reticle, they were not characterised due to time constraints.

CHAPTER 9

Fabrication and Sidewall Measurements of Waveguides

This Chapter contains the discussion of the fabrication process. The etching process has the largest impact on the shape and roughness of the fabricated waveguides, and the results from different etching tools and methods will be presented.

9.1 Fabrication Process

As a first step, 2300 nm of thermal SiOx was grown on the Si substrate, after which the SiOx was polished using chemical-mechanical polishing (CMP) to reduce the surface roughness. As the next step 170 nm of SiN was deposited in an oven process, which showed low roughness, of $R_q \approx 0.15$ nm, and did not need an additional CMP step. Afterwards, the backside antireflection coating (BARC) and photoresist were deposited on the wafer using spin coating. The reticle, presented in Chapter 8, was transferred to the photoresist using a KrF DUV process and the resist was developed. The critical dimension (CD) of the patterned resist was measured in a SEM, where the target width was the widths discussed in Chapter 8 increased by 15 nm due to a known overetch which will be explained later in this chapter. In the next step, first the BARC was etched in the etching chamber and then the SiN was etched. The remaining photoresist and BARC were removed with an O_2 plasma. After that, the CD was measured again using a SEM. The wafers dedicated to sidewall roughness measurement were mechanically diced. For wafers with waveguides for loss measurements, ∼6 µm of PECVD SiOx was deposited on top of the etched waveguides after resist removal, after which they were stealth diced, a process which will be explained in the following paragraph.

Wafers which are fabricated to yield chips for loss measurements are diced using the stealth dicing method as opposed to mechanical dicing using a saw, as the latter creates rough facets, which negatively impacts the incoupling of the laser light. The rough facets can be polished, but this involves extra effort, as both facets for every chip need first a rough polish step followed by a fine polish. This procedure yields optically smooth chip facets. The method of stealth dicing involves the following procedure: First, a laser is used to induce multiple defects in the silicon lattice along the dicing lines and at different depths in the substrate. This is followed by expanding the foil on which the wafer is mounted to separate the chips from each other along the dicing lines.

The facets of chips without further preparation are shown in Figure 9.1a and b and show that the quality of the facet varies, this could stem from the dicing process itself or it is possible that the facets of neighbouring chips are ground against each other while picking the chips from the foil. A single fine polish step was conducted on the facet in Figure 9.1c and shows a clear improvement. The facet quality of stealth diced chips warrants further investigation but these results indicate that a combination of stealth dicing and a fine polish produce high quality facets for edge coupling of photonic chips.

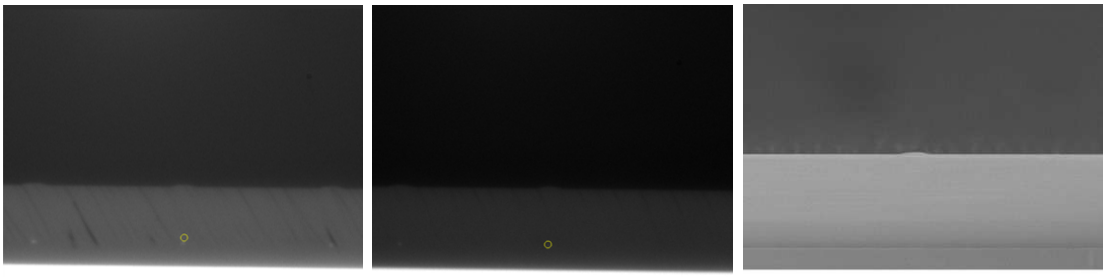

(a) (b) (c)

Figure 9.1: (a) and (b) Facets of stealth diced chips under microscope view, the white dots are the waveguides where the waveguide in the middle is in the yellow circle, (c) SEM image of the polished facet, the waveguide is in the middle of the picture but not visible in SEM.

9.2 Investigation of Etching Tools and Methods

The etching process is the main impact on waveguide shape and sidewall roughness, as seen in multiple publications in Chapter 6. Therefore, an investigation of different etching tools and methods was conducted.

9.2.1 Variation of RIE Etch Tools

Reactive ion etching (RIE) is the main etching process used to fabricate waveguides. To see if the employed tools have an impact on the shape and sidewall roughness, four different

etchers were used to structure the waveguides. Etchers 1 and 2 employ an inductively coupled plasma, while etchers 3 and 4 use a capacitively coupled plasma. Figure 9.2 shows top-down SEM images of the etched structures. To evaluate which etcher is the best, it is important to see if the waveguide is properly etched. That is, if the top surface is etched, if the taper angle is close to 90°, schematically shown in Figure 9.3, and if the resulting width of the waveguide deviates from the target width due to an overetch, this difference is called the etch bias.

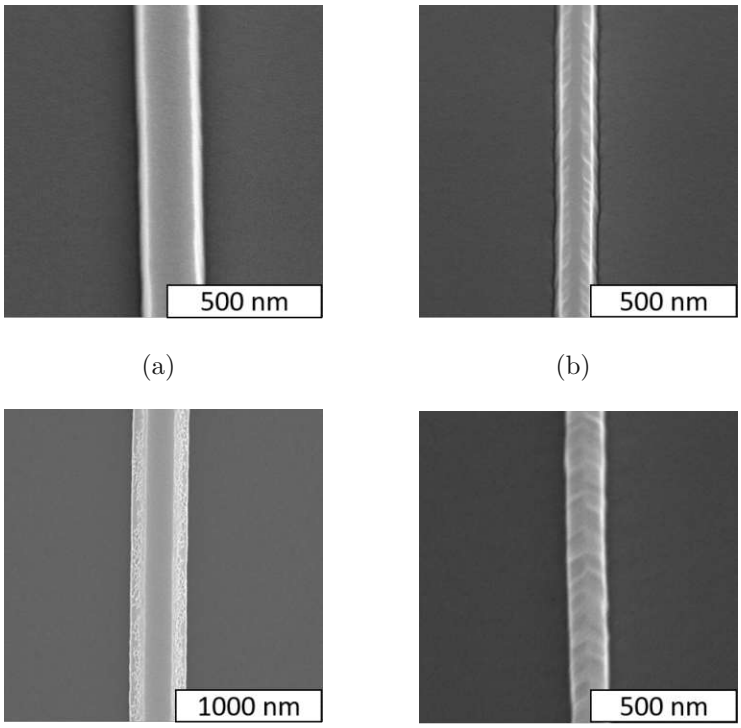

Figure 9.2: Top-down SEM images of waveguides etched with (a) etcher 1, (b) etcher 2, (c) etcher 3, and (d) etcher 4.

Etcher	**Taper Angle** α [°]
1	85
2	87
3	60
4	80

Table 9.1: Measured taper angles α for the different etchers. The calculation of the angle depends on the resolution of the cross-section and is accurate up to ±2°.

As can be seen in Figure 9.2, the etched waveguides have a tapered geometry because the sidewalls of the waveguides are visible in the top-down image. The taper angles α for the different etchers are listed in Table 9.1. Figure 9.2a shows the results from etching with etcher 1. The sidewalls are steep and the top surface is not etched during the process,

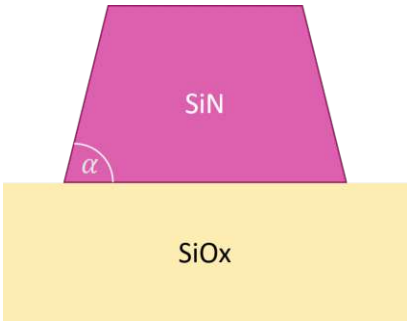

Figure 9.3: Schematic depiction of a tapered waveguide cross-section of the SiN waveguide on SiOx bottom cladding. The taper angle is α.

the angle of the sidewalls is 85°. The etch bias is close to zero, as this etcher was used for previous structuring of SiN waveguides before this thesis and thus the reticle was adjusted for the expected etch bias, as mentioned in Chapter 9.1. The result of etcher 2 is depicted in Figure 9.2b, although the sidewall angle is close to ideal at 87°, the top surface is strongly etched, which is clearly visible in the top-down SEM image. Additionally, the waveguide overetch is significant with a bottom width of ∼140 nm instead of the target 250 nm. Figure 9.2c shows the waveguide etched with etcher 3. The top surface is not etched, but a small taper angle of 60° is visible in addition to redeposited material on the sidewalls. The source of this could be either redeposited oxide, from an overetch into SiOx, or repolymerisation from the etched photoresist. Additionally, the waveguide shows a large etch bias of 100 nm. The result with etcher 4 is shown in Figure 9.2d, with an acceptable sidewall angle of 80° but strong etching of the top surface reduced the waveguide thickness to ∼80 nm. Additionally, the width is reduced to ∼130 nm instead of 250 nm. An overetch into the SiOx below was visible for each etcher, where etchers 1 and 2 showed a stronger etch close to the sidewall commonly due to the physical etch component.

By judging each etcher's performance with the above-mentioned criteria, together with initial AFM measurements, I could determine that etcher 1 is the best available etcher for the purpose of producing SiN waveguides. Even disregarding the advantage of the etch-bias-adjusted reticle, it resulted in good taper angles without etching the top surface. Furthermore, for each etcher, the etch recipes were adjusted but showed no significant improvement, with etcher 1 showing the best overall performance.

Thus, all further RIE steps in the following trails were conducted using it. A first test wafer using etcher 1 was diced after etching as described in Chapter 9.1, and the separated chips were used to measure the roughness of the sidewalls of the test structures according to the scheme proposed in Chapter 8.2. Multiple measurements were performed with the resulting RMS roughness values R_q and correlation length values along the waveguide $L_{c,z}$ shown in Table 9.2. The information on whether the chip was taken from the centre or

the half-radius of the wafer is also listed. Figure 9.4 shows an example of the sidewall AFM measurement. The lower part of Figure 9.4 shows the oxide layer, with a clear jump due to the cleave edge followed by the SiN waveguide sidewall. The vertical striations, often referred to as curtaining, is clearly visible. The slight angle of the striations comes solely from an offset during measurement. This was checked by repeated measurements of the same sidewall, where the striations were perfectly vertical on another try, while a measurement in the other direction showed the striations angled in the opposite direction as before. The varying roughness along the waveguide's propagation axis is also visible. Above the waveguide, the AFM tip is in the air, and thus only noise is measured. CD measurements of the etched waveguides showed a worst-case deviation of the target width of ±15 nm, due to the sum of variations from lithography and etching. The AFM measurements in Table 9.2 indicate a slightly higher roughness of waveguides further away from the waveguide centre, while there is no clear connection between correlation length and position of the measured chip on the wafer. No measurements of the sidewall roughness were made at the outermost edge of the wafer. Table 9.3 shows mean values and standard deviation of the R_q and $L_{c,z}$ data, which will be important for the simulation of the waveguide loss in Chapter 11.

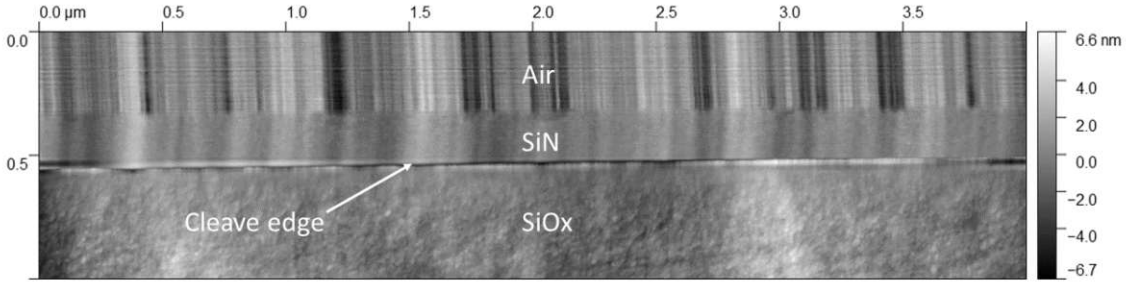

Figure 9.4: AFM measurement of the sidewall of a SiN waveguide on a cleaved chip. The transition from bottom SiOx to SiN is clearly visible by the edge produced curing the cleaving of the chip.

Location	R_q **[nm]**	$L_{c,z}$ **[nm]**
Centre	0.86	72
Centre	1.04	54
Centre	0.95	99
Centre	0.97	61
$R/2$	1.07	52
$R/2$	1.08	47
$R/2$	1.17	77
$R/2$	1.26	70

Table 9.2: Measured R_q and $L_{c,z}$ for different chips of the wafer etched by etcher 1. Chips were either taken from the centre or the half radius ($R/2$) of the wafer.

R_q **Mean [nm]**	R_q $\pm\sigma$ **[nm]**	$L_{c,z}$ **Mean [nm]**	$L_{c,z}$ $\pm\sigma$ **[nm]**
1.05	0.12	67	16

Table 9.3: Mean values and standard deviation of R_q and $L_{c,z}$ for the etching process using etcher 1.

9.2.2 Variation of Etching Methods

Although RIE is most commonly used to etch waveguides, other methods such as wet-chemical etching and ion beam etching (IBE) were explored to see how the different etching processes impact the resulting waveguides. Figure 9.5 shows top down SEM images of the etched structures. The wet-chemical process uses a polycrystalline Si hard mask and a subsequent etch in hot phosphoric acid to selectively etch the SiN to the Si.

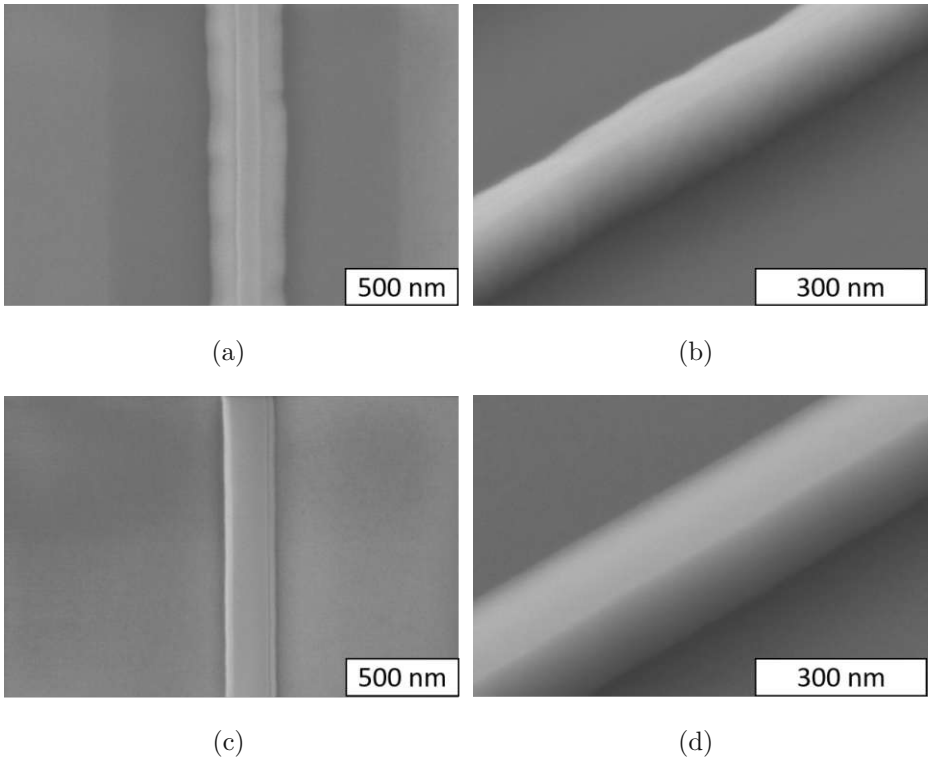

Figure 9.5: SEM images captured (a) top-down and (b) 45° angled of IBE process as well as (c) top-down and (d) 45° angled capture of wet etch process. In both processes, the pictured waveguide has a target width of 500 nm.

Figure 9.5a and b show the ion beam etched waveguide. A high roughness is clearly visible, as well as a strong decrease in the target CD. The top surface was also etched, creating the waviness visible in Figure 9.5b. The wet-chemically etched waveguide is depicted in Figure 9.5c and d. The sidewalls are smooth compared to the IBE process. The SEM images indicate a nearly rectangular cross-section, with an estimated taper angle of ∼85°, as no significant taper is visible in neither top-down nor angled image, similar to the RIE etched waveguide in Figure 9.2a.

Although the IBE process did not produce an accurately measurable sidewall, a single AFM measurement of the wet-etched waveguide showed a R_q value of 1.51 nm and a $L_{c,z}$ value of 107 nm. The roughness higher by ∼50% while the correlation length is slightly larger compared to the results of the RIE process with etcher 1 in Table 9.2.

Although the wet-chemical process results in waveguides of acceptable shape and roughness, it is not viable for fabrication of usable PICs because of the significant overetch resulting from the isotropic nature of the process. The significant reduction of the target width prohibits the fabrication of structures with large height-to-width ratios, such as grating couplers. The IBE process showed etching of the surface and increased sidewall roughness. Tuning of the etching parameters and the possible inclusion of a hard mask to protect the SiN during etching could improve the process but warrants further engineering.

9.3 Investigation of BARC Etch and SiN Etch on Photoresist

Top-down SEM measurements of the resist after lithography, BARC etch, and SiN etch are shown in Figure 9.6. After lithography (Figure 9.6a), the resist is smooth and does not exhibit clearly visible roughness. Etching the BARC (Figure 9.6b) results in a lumpy and rough resist topography. The SiN etch (Figure 9.6c) consumes the resist during the process, but local deviations of the width are observable. Figure 9.7 shows a SEM image at a 45° angle where unknown material is clearly visible on the sidewall and the bottom of the waveguide. A possible explanation is the polymerisation of the resist during the BARC etch, which could lead to increased non-uniformity in the pattern transfer step of the SiN etch, as explained by Marchack et al. [49] in the case of Si waveguides.

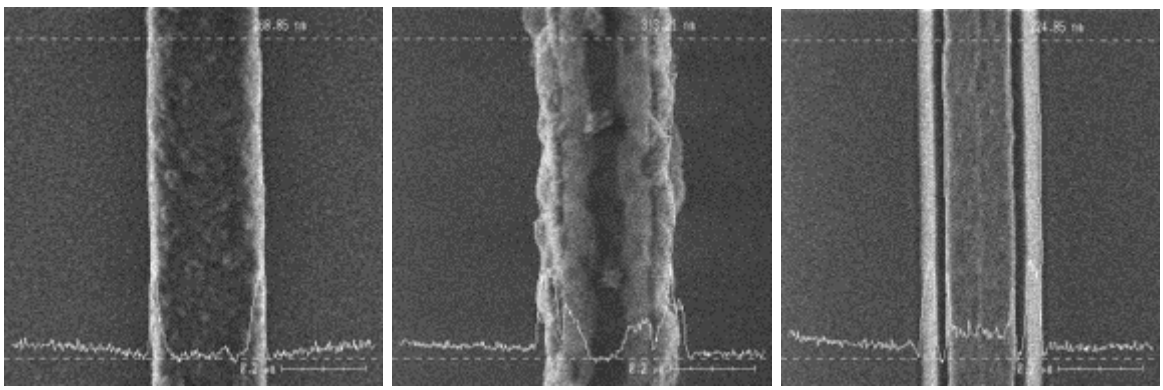

(a) (b) (c)

Figure 9.6: Top-down SEM images of the same 250 nm wide waveguide after (a) lithography, (b) BARC etch and (c) SiN etching. For each step the CD is measured which shows the etch bias for the SiN etch.

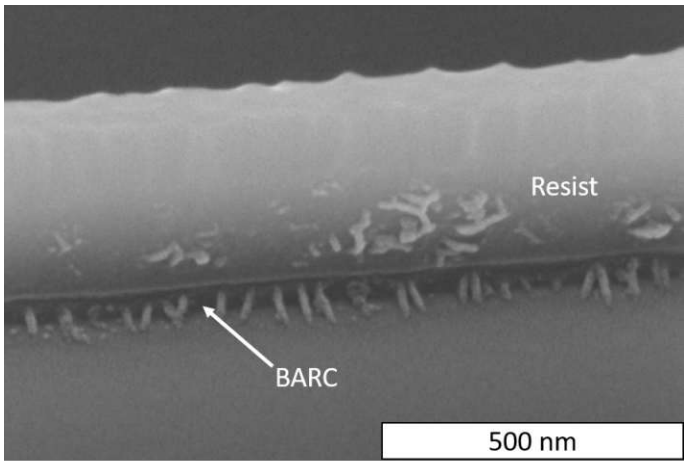

Figure 9.7: 45° angled SEM image of the resist after opening the BARC. The etched top surface of the resist is clearly visible as well as the redeposition along the sidewall and at the bottom interface between SiN and BARC.

To mitigate this, the lithography process was tested without BARC but because of the low surface adhesion of the photoresist on SiN, even with the addition of the adhesion promoter hexamethyldisilazane (HMDS), the resist structures were removed during the development step.

Comparison of these results with the measurements from Roberts et al. [42] in Table 6.1 show that our DUV process performs better in terms of RMS roughness while a deviation in the correlation length is observable. How the correlation length impacts the scattering loss will be explained in a later chapter. In contrast, the electron-beam process yields better roughness while yielding comparable correlation lengths. The most significant drawback of electron-beam lithography is low throughput.

CHAPTER 10

Waveguide Characterisation

This chapter contains a description of the measurement setup for waveguide characterisation. An overview of which waveguide width was measured with the corresponding wavelength is given in Table 10.1, as the waveguides should only be single mode. As explained in Chapter 8, the waveguides were originally designed for single mode operation in a wavelength range of 497-786 nm, but due to the availability of wavelengths 450 and 866 nm the single mode operation was checked with Ansys Lumerical MODE and is discussed in the corresponding section of the measurement results.

Input Laser Wavelength [nm]	**250 [nm]**	**300 [nm]**	**500 [nm]**
450	x		
532	x		
639	x	x	
730	x	x	x
866			x

Table 10.1: Measured waveguide widths (rows) for available wavelengths (columns). The waveguide widths was chosen such that the waveguides were expected to operate in single mode.

10.1 Measurement Setup and Method

Figure 10.1 shows the measurement setup used for waveguide characterisation, as well as a schematic overview of the setup. The incoupling setup is fixed on a high-precision hexapod positioning system from PI, which allows the input to be positioned and aligned in six degrees of freedom, three translation axes and three rotational axes. The laser

light is coupled in via a polarisation-maintaining fibre and the beam collimated with an aspheric lens. The subsequent half- and quarter-plates are used to adjust the polarisation of the light. Afterwards a 66/33 splitter is used to direct a part of the light to an opening where collimation, polarisation, or power of the beam can be measured. Fixed to the same splitter is a light source to visualise the input facet and a Thorlabs CS165MU/M camera to find the waveguides. A Nikon LU Plan 100x BD microscope objective is used to focus the beam. The PIC is placed on a vacuum chip holder in the middle of the setup, which can move vertically to place the output facet in the output camera's field of view. The output stage of the setup is placed on two GMT servo motors which allow the camera to be moved along the remaining two translation axes. The outgoing light of the waveguide is collected by a Nikon LU Plan x50 BD microscope objective. A cage for a Thorlabs filter holder is placed after the objective to optionally dampen the light to prevent damage to the camera. Similarly to the input side, a light source and Lucid camera are attached to find the waveguides at the output facet and record the outgoing light. An additional Lucid camera is placed facing the surface of the chip to assist in finding the waveguide structures and optionally record top-side scattered light

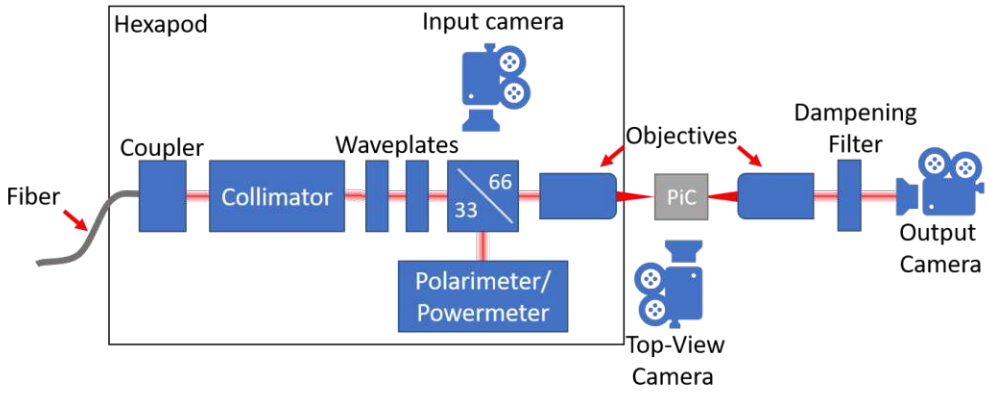

Figure 10.1: Setup used for waveguide loss characterization. Light is coupled in from the left side and focused at the sample mounted on the sample holder. The transmitted light is collected by an objective and measured with a camera mounted on the rightmost part of the cage. Additional cameras on the input side and front facing support in finding waveguide structures.

All waveguides were measured using the cut-back method, explained in Chapter 6. For each waveguide measurement, the following procedure is carried out:

1. The waveguide to be measured is roughly approached such that the incident laser light beam is overlapping with the waveguide at the input side. The output side is adjusted such that the waveguide is visible in the output camera.

2. The microscope illumination at input and output are turned off and the laser light is switched on.

3. The polarisation is checked to ensure that the incoupled light is TE or TM polarised, depending on the current measurement.

4. The powermeter is connected at the splitter output on the input side to monitor the power of the laser light during measurement.

5. The input and output stages are positioned such that the recorded light spot at the output is as bright as possible.

6. The image of the output is saved together with the exposure time of the camera to enable accurate post-processing.

10.2 Measurement Results

The measurement results are presented for each waveguide geometry. For each measured wavelength, an example of the linear fit for one chip is shown, and the weighted mean of the measurements with error bars of one standard deviation are presented at the end. In total, five chips were measured that are labelled chips 1-4 with the additional chip whose facets were polished, labelled chip B1. Unfortunately, after the first measurement with 639 nm laser light chip 4 was damaged which is why, besides for 639 nm, only four chips were available for measurement. As explained in Chapter 8, the full chip has waveguides of lengths 30, 40, 60, 80 and 100 mm, with the possibility of halving the waveguide lengths. Due to an error in the dicing plan, only chips with halved waveguide lengths were available to measure.

10.2.1 170x250 nm

Simulation of the tapered waveguide, which is closer to the actual waveguide shape as seen in Chapter 9, has shown that the waveguide possesses a strongly dampened second-order TE mode for a wavelength of 450 nm, which disappears if the waveguide base width is slightly narrower than the target of 250 nm. Higher wavelengths always resulted in single-mode operation, even for rectangular waveguides wider than the target width. Therefore, the measurements for 450 nm light were included, with the result for chip 5 shown in in Figure 10.2a for the TE mode and 10.2b for the TM mode. Although a linear fit is possible, a slight curvature in the distribution of the points is observable, which is present for each chip measurement. A possible explanation for this behaviour could be mode conversion into the higher TE mode or conversion from TE to TM modes and vice versa over long distances and in bends, which might be the cause for the reduced loss. Similarly, the initial TM mode might leak into the TE modes, which increases the loss. This could explain the similar loss for TE and TM polarised light.

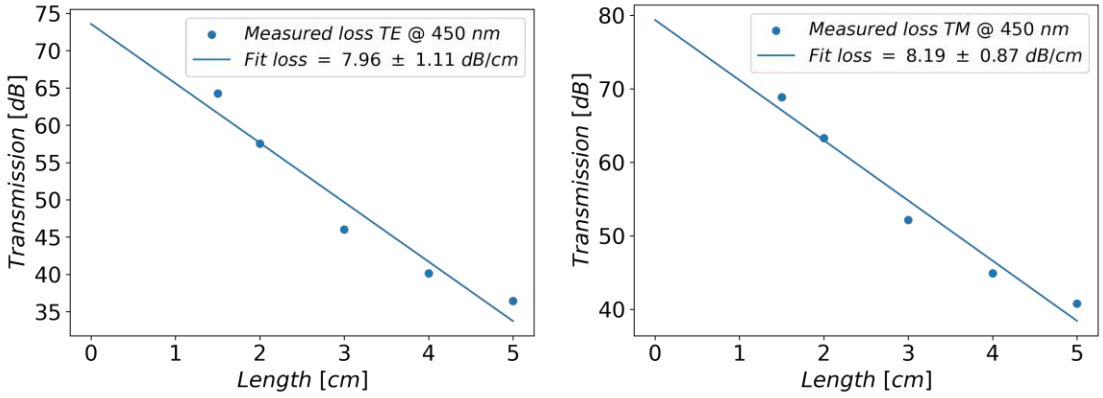

(a) (b)

Figure 10.2: Linear fit of the measured loss for 250 nm wide waveguides at a wavelength of 450 nm for (a) TE and (b) TM modes of chip 5.

The linear fit of the measurement with 532 nm wavelength of chip 5 is shown in Figure 10.3a for the TE mode and 10.3b for the TM mode. Some variation in the power of the measured output was observed, which is likely due to power fluctuations in the laser. Each fit of the measured chips is of similar quality to the example given.

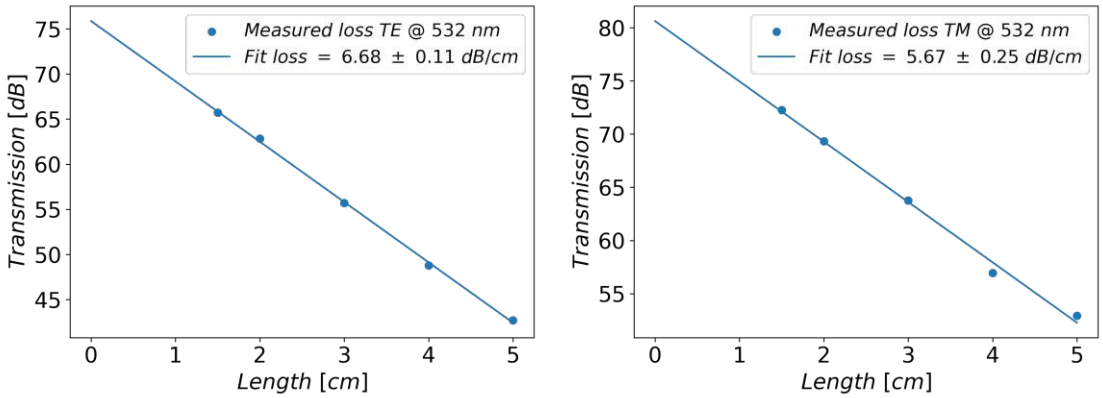

(a) (b)

Figure 10.3: Linear fit of the measured loss for 250 nm wide waveguides at a wavelength of 532 nm for (a) TE and (b) TM modes of chip 5.

Measurements with 639 nm laser light exhibited higher fluctuations in power resulting in greater uncertainties of the linear fits. The best fit from chip 5 is depicted in Figure 10.4a for the TE mode and 10.4b for the TM mode. The measurements for other chips show a greater variance, likely because of the greater fluctuation of the laser's power or local inhomogeneities in the facet roughness, which was observed during measurement, because no clear trend in the distribution of the measured powers was observed.

The longest wavelength measured for the 250 nm wide waveguides was 730 nm. The linear fits show good results, with the best fit depicted for chip B1 in Figure 10.5a for the

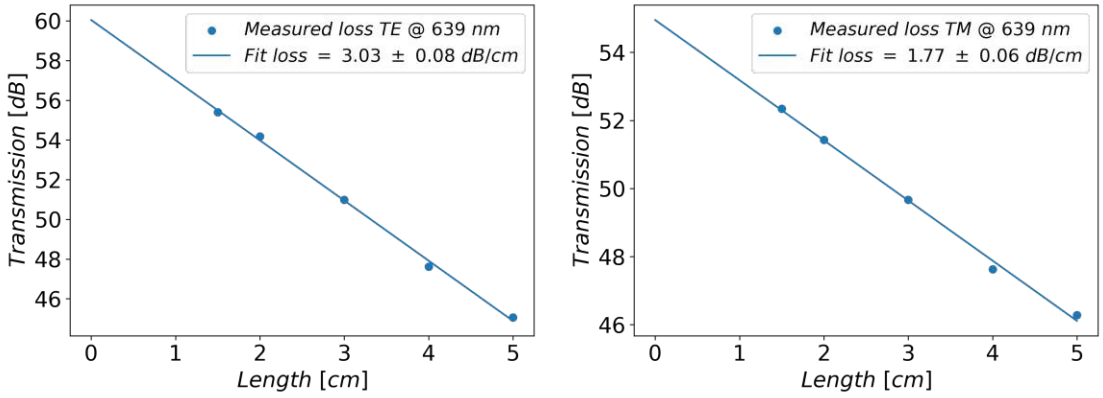

(a) (b)

Figure 10.4: Linear fit of the measured loss for 250 nm wide waveguides at a wavelength of 639 nm for (a) TE and (b) TM modes of chip 5.

TE mode and 10.5b for the TM mode.

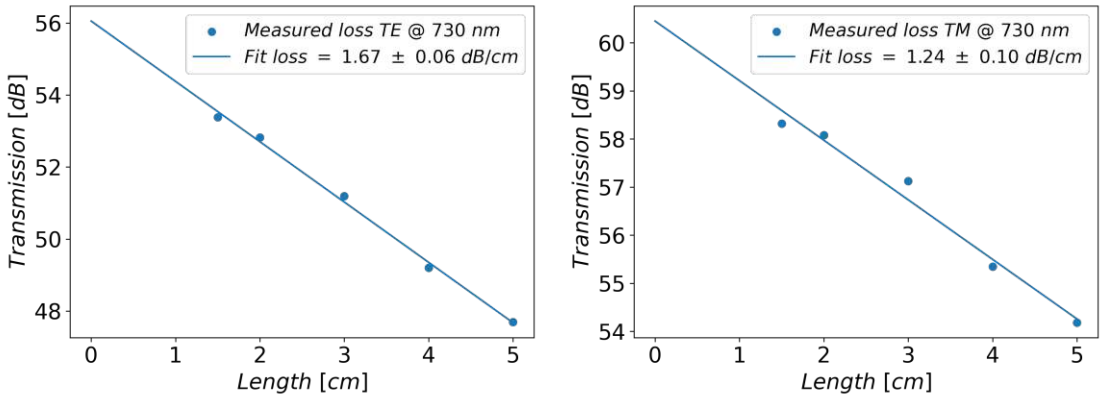

(a) (b)

Figure 10.5: Linear fit of the measured loss for 250 nm wide waveguides at a wavelength of 730 nm for (a) TE and (b) TM modes of chip B1.

Figure 10.6 shows the measured losses of TE and TM modes with the corresponding mean values and standard deviations listed in Table 10.2. The loss for a wavelength of 450 nm was measured to be higher for TE than for TM mode, which is, as explained above, likely due to multimode conversion in the waveguide. For the remaining wavelengths, the loss of the TE mode remains larger than the loss of the TM mode, but the difference decreases as the wavelength increases. The next highest available wavelength, 866 nm, was not measured as simulations showed that no mode could propagate in the waveguide.

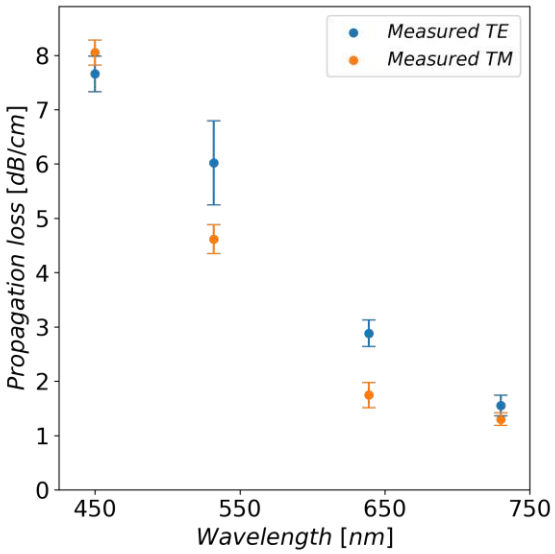

Figure 10.6: Collected mean loss with one standard deviation of TE (blue) and TM (orange) modes over the measured wavelengths for 250 nm wide waveguides.

Input Laser Wavelength [nm]	**TE Mean Loss [dB/cm]**	**TE $\pm\sigma$ [dB/cm]**	**TM Mean Loss[dB/cm]**	**TM $\pm\sigma$ [dB/cm]**
450	7.66	0.33	8.05	0.23
532	6.02	0.77	4.62	0.26
639	2.88	0.24	1.75	0.23
730	1.55	0.19	1.30	0.12

Table 10.2: Mean loss and standard deviation for TE and TM polarised laser light of the measured wavelengths for 250 nm wide and 170 nm thick waveguides.

10.2.2 170x300 nm

The best linear fits of the measurements with 639 nm were observed for chip 5 and are depicted in Figure 10.7a for the TE mode and 10.7b for the TM mode. Similarly to the 250 nm wide waveguides, an increased variation in the measured power was observed for some chips with rough facets.

The measurements for 730 nm showed little variation, as seen in the examples in Figure 10.8, with the fit of chip 5 yielding the best results.

Simulations predicted both TE and TM propagating modes for 866 nm but the measurement showed significant crosstalk from the 300 to the 500 nm waveguides. Because during chip design the crosstalk simulations for this wavelength was not conducted and the gap distance between waveguides is too small.

The collected measurements are depicted in Figure 10.9 with the means and standard deviations in Table 10.3, as expected the loss for TE is higher than TM and decreases

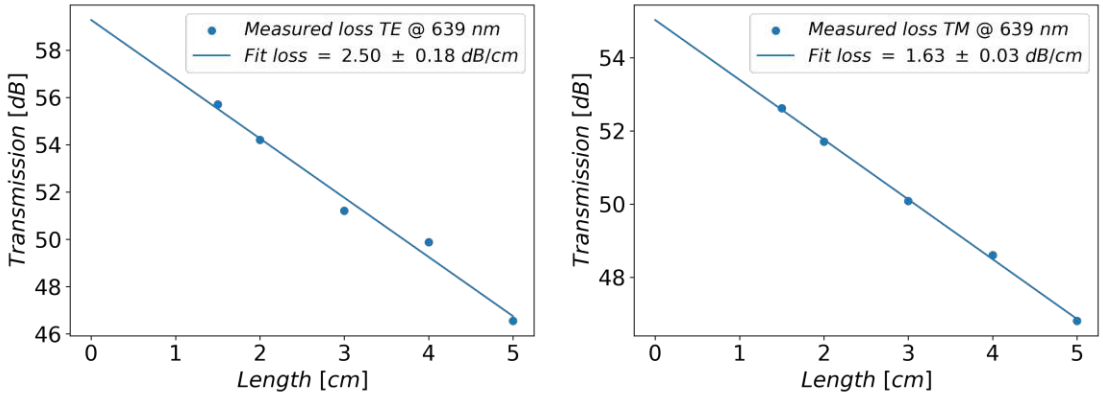

(a) (b)

Figure 10.7: Linear fit of the measured loss for 300 nm wide waveguides at a wavelength of 639 nm for (a) TE and (b) TM modes of chip 5.

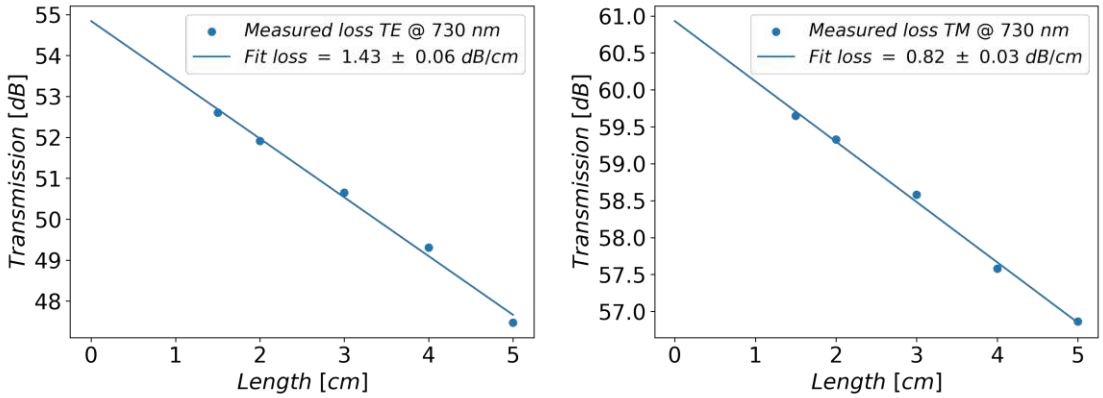

(a) (b)

Figure 10.8: Linear fit of the measured loss for 300 nm wide waveguides at a wavelength of 730 nm for (a) TE and (b) TM modes of chip 5.

with longer wavelengths. Due to only two measurement wavelengths, it is not possible to qualitatively describe the behaviour of the loss over other wavelengths. Furthermore, a decrease in the loss for the wider waveguide is observable when comparing the results for the 250 and 300 nm wide waveguides.

This is concurrent with the theory that an increased width reduces the electric field strength at the sidewall and thus the scattering losses.

10.2.3 170x500 nm

Similarly to the measurements of 250 and 300 nm wide waveguides, some output power variation was observed for the 500 nm wide waveguides for 730 nm laser light. Also, similarly to the other measurements, better facets yielded less variation in the output powers. The best fit from the measured chips was for chip 5 and is shown in Figure 10.7a

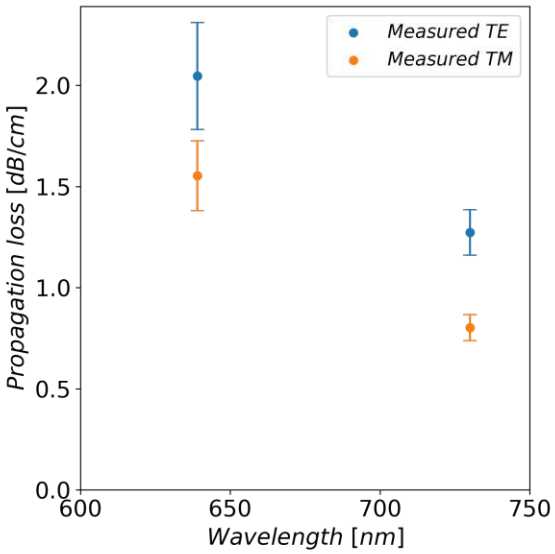

Figure 10.9: Collected mean loss with one standard deviation of TE (blue) and TM (orange) modes over the measured wavelengths for 300 nm wide waveguides.

Input Laser Wavelength [nm]	**TE Mean Loss [dB/cm]**	**TE $\pm\sigma$ [dB/cm]**	**TM Mean Loss[dB/cm]**	**TM $\pm\sigma$ [dB/cm]**
639	2.05	0.26	1.55	0.17
730	1.27	0.11	0.80	0.06

Table 10.3: Mean loss and standard deviation for TE and TM polarised laser light of the measured wavelengths for 300 nm wide and 170 nm thick waveguides.

for the TE mode and 10.7b for the TM mode.

The measurements with 866 nm wavelength only yielded results for both TE and TM mode in chip 1, depicted in Figure 10.11, while it was possible for chip B1 to conduct a linear fit of the TE mode, this was not possible for the TM mode. In the case of chip 2 this was the other way around with the TM yielding an acceptable fit. A possible explanation could be that the loss is so low that the fluctuations in the observed spot brightness at the waveguide outputs are larger than the loss itself. Therefore, a good fit can only be extracted when the error due to the fluctuations is equal over the measured wavelengths. Crosstalk between waveguides is unlikely, as overexposed measurements of the waveguide outputs yielded no observable crosstalk. Measurements of the full chip, which contains waveguide lengths of 60, 80 and 100 mm, could result in better loss measurements, as the loss of the individual waveguides is larger due to the longer propagation distance.

The measurements of the two wavelengths are collected in Figure 10.12 with the calculated means and standard deviations listed in Table 10.4. The results of 730 nm wavelength show the expected decrease in loss for the wider waveguide, as well as a smaller TM loss than TE loss. The larger loss of the TM mode at 866 nm is due to the unreliable measurements.

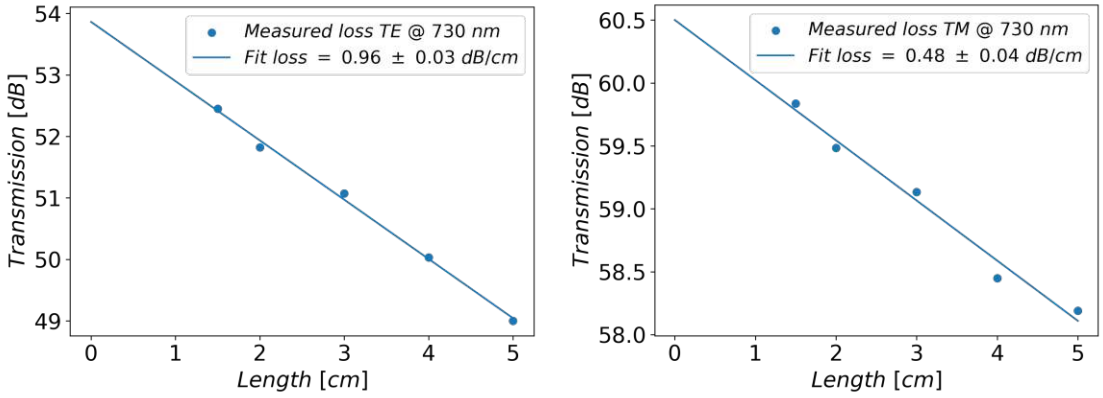

(a) (b)

Figure 10.10: Linear fit of the measured loss for 500 nm wide waveguides at a wavelength of 730 nm for (a) TE and (b) TM modes of chip 5.

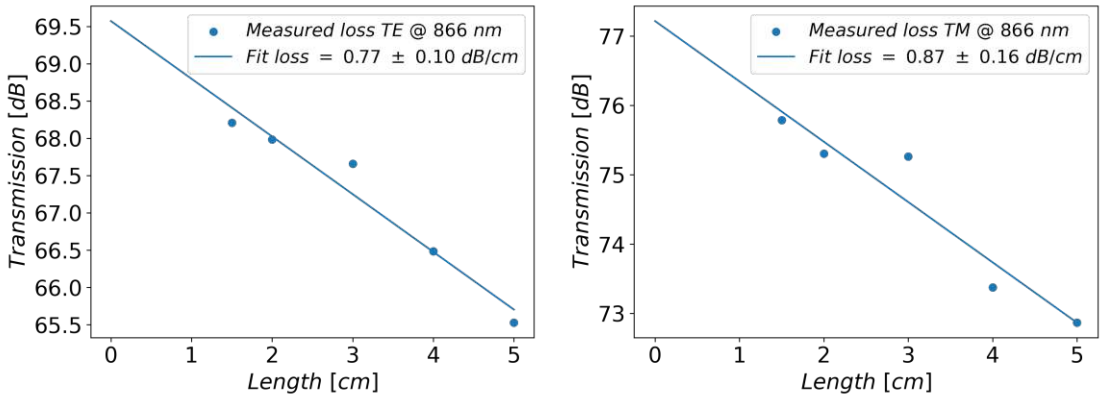

(a) (b)

Figure 10.11: Linear fit of the measured loss for 500 nm wide waveguides at a wavelength of 866 nm for (a) TE and (b) TM modes of chip 1.

The measurements generally yielded good linear fits. An increased fit quality was observed in chips with smooth facets over all waveguide lengths, such as chip 5 and chip B1, compared to visibly rougher facets, which was observed for chip 1 and chip 2. Although chip 5 was not polished after dicing, better facet quality was observed compared to chips 1 and 2. This warrants further investigation in the stealth dicing process and confirms the discussion in Chapter 9.1. Furthermore, for wavelengths in near-IR, measurements over longer waveguide lengths are expected to increase the accuracy of the measurements.

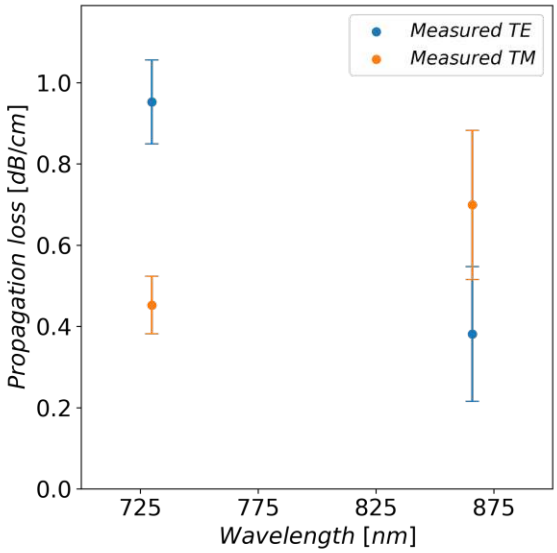

Figure 10.12: Collected mean loss with one standard deviation of TE (blue) and TM (orange) modes over the measured wavelengths for 500 nm wide waveguides.

Input Laser Wavelength [nm]	**TE Mean Loss [dB/cm]**	**TE $\pm\sigma$ [dB/cm]**	**TM Mean Loss[dB/cm]**	**TM $\pm\sigma$ [dB/cm]**
730	0.95	0.10	0.45	0.07
866	0.38	0.16	0.70	0.18

Table 10.4: Mean loss and standard deviation for TE and TM polarised laser light of the measured wavelengths for 500 nm wide and 170 nm thick waveguides.

CHAPTER 11

Simulation of Waveguide Loss

While measurements give loss values for fabricated waveguide geometries at certain wavelengths, a robust waveguide loss estimation is desired to predict the loss for arbitrary waveguide geometries and wavelengths. The loss from material absorption can be calculated by fitting the measured thin film losses, as seen in Chapter 7, and applying Equation 5.1 with the percentage of power contained in the waveguide for the chosen mode. This is calculated as follows

$$P = \frac{1}{2}\int_0^t \int_0^w \Re\{\mathbf{E} \times \mathbf{H}^*\} dxdy \tag{11.1}$$

where t is the thickness of the waveguide, and w the waveguide width. The cross product of electric field $\mathbf{E}$ and magnetic field $\mathbf{H}$ is the Poynting vector, which can be used instead to calculate the power in the waveguide. The 1/2 factor comes from the fact that either input or output power is calculated, which are equal for the cross-section. The power of the whole mode, including the portion of the mode in the cladding, can be calculated by setting the integration limits to $\pm\infty$, as seen in Equation 5.28.

All loss values presented include the waveguide material loss, unless it is explicitly stated that only the scattering loss is discussed. Furthermore, unless stated otherwise, all calculations of the waveguide modes were done using the Ansys Lumerical MODE simulation suite. Only rectangular waveguides are simulated, as the simulation of the tapered waveguide results in inaccurate fields extracted from the sidewall due to the rectangular mesh of the finite difference method. A finite element method (FEM) simulation can be used for more accurate fields at the tapered sidewalls which will be discussed at the end of this chapter.

11.1 Implementation of the Scattering Simulation

To enable calculation of the scattering loss, the Hoermann model, as presented in Chapter 5.2, was implemented using Python. The calculation depends on the extracted electric field values at the waveguide interfaces, which was done by a function written in Python that searches the 2D mode field and extracts an 1D array of the electric field in the three spatial coordinates at the surfaces. The process of obtaining the waveguide loss is as follows:

1. The desired waveguide geometries and wavelengths are simulated, and the resulting TE and TM fields are saved using Python's Pickle module.
2. The simulation result file is loaded in the Python script for loss calculation.
3. The script extracts the necessary information for calculation from the simulation results, such as wavelength, waveguide width and height, effective refractive index of the modes, and electric fields.
4. The script finds the electric fields at the inside of the waveguide surfaces and saves them in an array, as well as calculating the power in the waveguide from the field of the Poynting vector.
5. The scattering at the interface is calculated using the Hoermann model using the measured R_q, $L_{c,y}$, and $L_{c,z}$ values.
6. The scattering for each interface and the total loss, including the waveguide material loss, are saved for further visualization.

11.2 Simulation of the Measured Waveguides

To compare the simulation with the fabricated and measured waveguides, combinations of wavelength and waveguide, as seen in Table 10.1, were simulated and the loss was estimated using the roughness parameters extracted from the AFM measurements listed in Table 9.2. Hoermann et al. [15] use a variation of the correlation length to match the theory results with experimental values. As the goal of this thesis is to find a suitable simulation model to estimate the waveguide loss without directly comparing it with measured values, and not to adjust the simulation to obtain the best fit, $L_{c,y}$ is measured by extracting the ACF from the sidewall AFM measurement. As mentioned in Chapter 5, the correlation length is commonly understood to be the distance after which the ACF has decayed to 1/e. The normalised ACF from a sidewall measurement, which is nearly identical for all sidewall measurements, is shown in Figure 11.1a. Clearly, the ACF does not drop to 1/e in the measured region because the waveguide height is too small. The

correlation length of the exponential kernel is therefore found by fitting the kernel over an extended distance, the result is shown in Figure 11.1b and estimates a correlation length of 2.8 µm. Although this method is not the most accurate, it is the best guess unbiased by the experimental loss results and is therefore used for the calculation of the propagation losses. Compared to the thickness of the waveguide of 170 nm the correlation length of 2.8 µm is effectively infinite and, as will be shown in Chapter 11.3, the difference in simulated loss for $L_{c,y}$=2.8 µm and $L_{c,y}$=∞ is very small. To check if the correlation length along the waveguide's propagation direction $L_{c,z}$ is accurate, the kernel is compared to the extracted ACF in Figure 11.2, where the measured correlation length was 47 nm and shows good agreement with the AFM data.

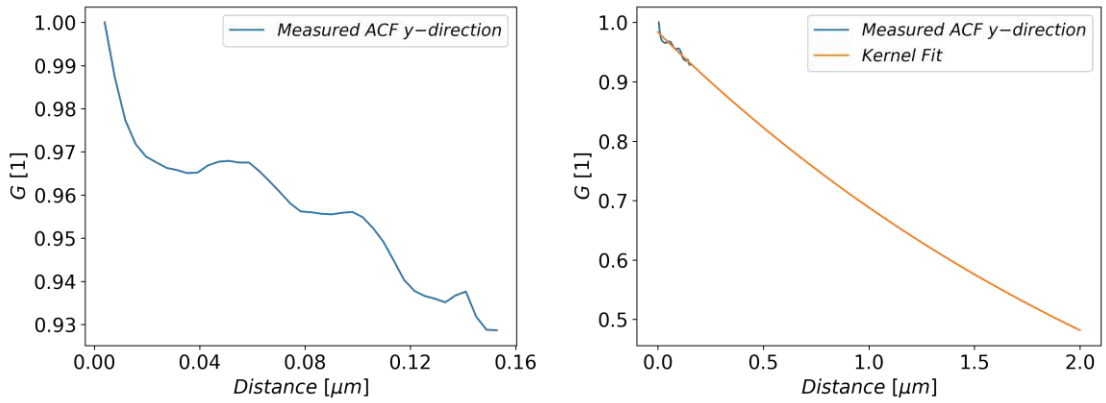

(a) (b)

Figure 11.1: (a) Measured ACF along y-axis (b) Fit of exponential kernel with $L_{c,y}$=2.8 µm over a distance of 2 µm as the measured ACF does not drop to 1/e in the measurement.

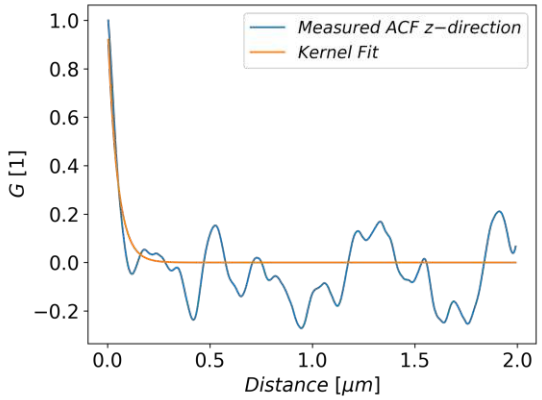

Figure 11.2: Measured ACF along z-axis (blue) with measured $L_{c,z}$=47 nm and fit of the exponential kernel (orange) for the measured correlation length.

The propagation losses are estimated with two methods: One in which each tuple of the R_q and $L_{c,z}$ values is used to calculate the loss and another in which a combination of the

R_q and $L_{c,z}$ values is used. The results are presented in Figure 11.3 where the simulated losses are compared to the measured losses for 250, 300 and 500 nm wide waveguides, where each width is one row. The left column contains the results for the loss calculations using the measured R_q and $L_{c,z}$ tuples, while the right column shows the calculated losses for the combinations for the mean values with one standard deviation for R_q and $L_{c,z}$. In both cases, the measured losses are identical. The large difference in measured and simulated losses for 450 nm in Figures 11.3a and b is likely due to the possible multimode operation or TE $\leftrightarrow$ TM mode conversion in the waveguide, as discussed in Chapter 10.2. Although the results for the TE mode at 532 nm in Figures 11.3a and b show good agreement, the TM mode is underestimated. For longer wavelengths, both modes show a closer match of the simulated and measured values. The TM modes for the 300 nm wide waveguides in Figures 11.3c and d show good fits between simulation and measurement, while the means of the TE mode for 639 nm deviate by $\sim$1 dB/cm and $\sim$0.5 dB/cm for 730 nm. The TE modes at 730 nm for the 500 nm waveguides in Figures 11.3e and f show good overlap, while the TM modes are almost coincident. Unfortunately, the simulation and measurement are poor fits for 866 nm due to inaccurate measurement. Furthermore, the losses for the R_q and $L_{c,z}$ tuples show a better agreement than the R_q and $L_{c,z}$ combinations.

The differences between measured and simulated losses could be influenced by two factors. On the one hand, the width was assumed to be exactly the target width of the design, variations in the actual width have been observed during fabrication, as mentioned in Chapter 9.2, with a worst-case deviation of $\pm$15 nm from the target width. Changes in the waveguide width lead to changes in the electric fields at the sidewalls. Therefore, simulations have been conducted where the wavelength was kept constant and the waveguide width varied. The other influence on the scattering loss could be the taper of the waveguide sidewalls. In cases where the difference of measured to simulated loss could not be reasonably explained by width variation, a simulation of the tapered waveguide could provide answers. For the calculation of the width sweep losses, the mean values of R_q and $L_{c,z}$, with deviations of $\pm\sigma$, were used to obtain upper and lower bound of a band for the simulation results. The error bars for the measured points denote the calculated standard deviation of the measured propagation loss and the deviation from target width. The correlation length in y-direction was kept constant at 2.8 µm Figure 11.4 shows the width sweep for the 250 nm wide waveguide at a wavelength of 450 nm. Although the TE loss could be explained by the deviation of the target width, the TM mode loss is significantly greater than the simulated loss. This supports the theory that other mechanisms, in addition to scattering and material losses, have an influence.

The width sweep for a 250 nm wide waveguide at a wavelength of 532 nm is depicted

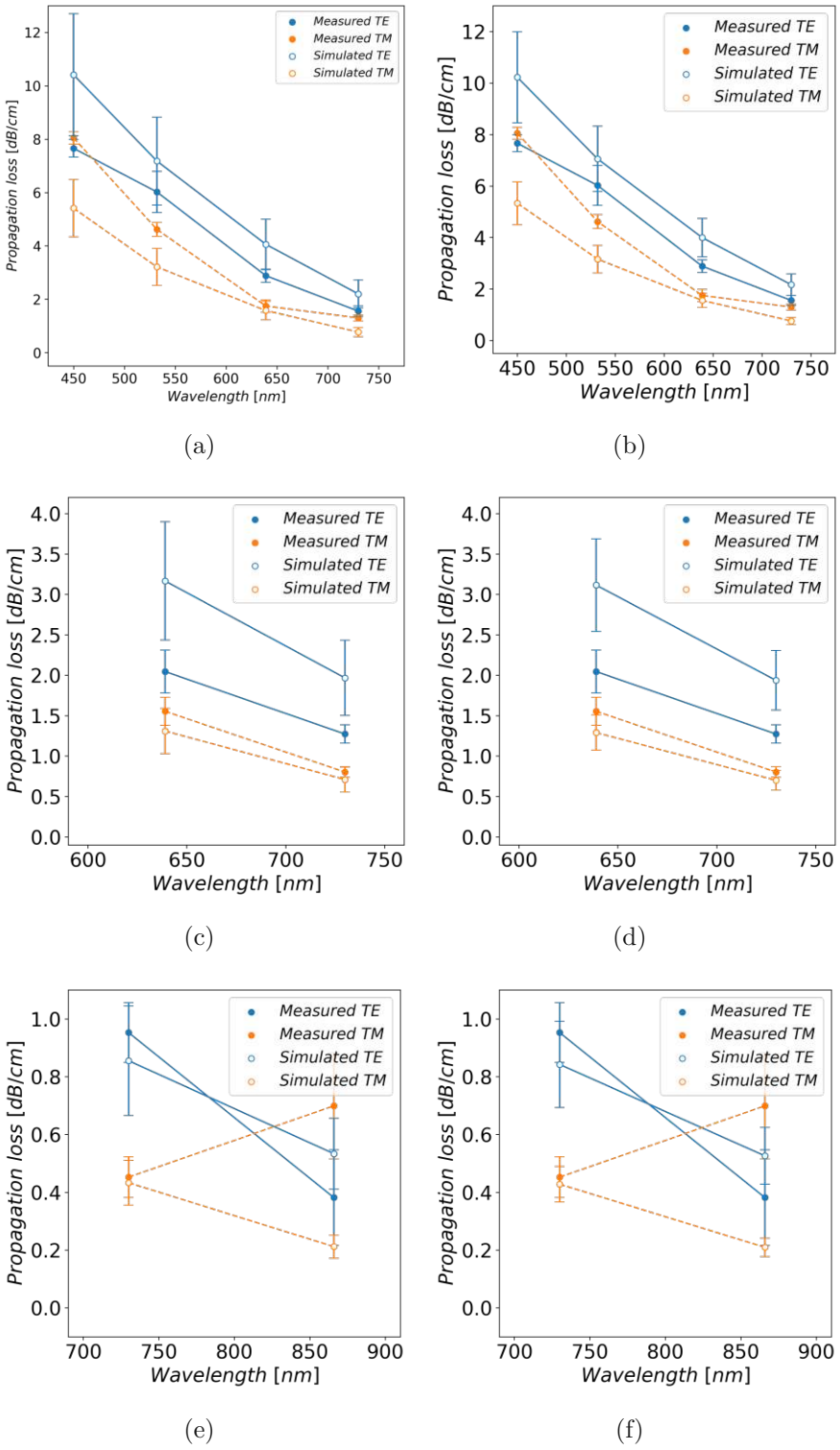

Figure 11.3: Left columns shows the result for measured R_q and $L_{c,z}$ tuples, right column shows the results for the combination of means ± one standard deviation of measured R_q and $L_{c,z}$ values. The measured TE (blue) and TM (orange) mode losses are plotted for the simulated TE (green) and TM (red) mode losses. (a) & (b) 250 nm wide waveguides, (c) & (d) 300 nm waveguides, and (e) & (f) 500 nm waveguides. The dotted lines between the measurement points are used to guide the eye and are not measured data.

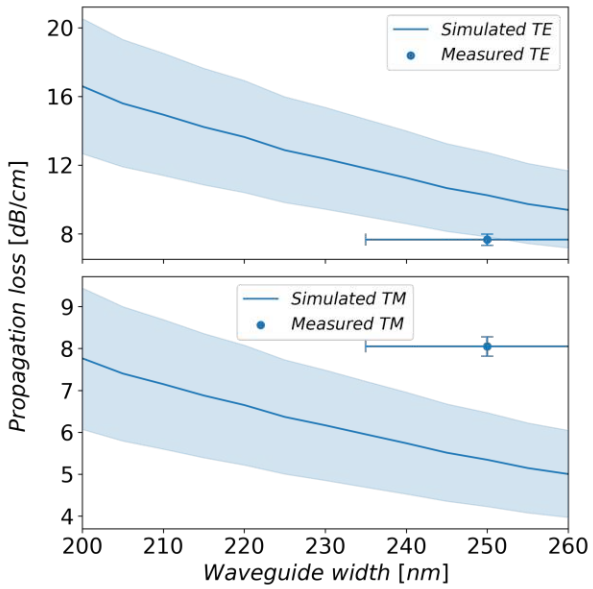

Figure 11.4: Propagation loss for the width sweep of a 250 nm waveguide at a wavelength of 450 nm.

in Figure 11.5. The loss of the TE mode fits within the lower bound for the target width, while the loss of the TM mode is outside the upper bound. TE $\leftrightarrow$ TM mode mixing could is unlikely to occur here, because the curvature in measured power as seen in the case for 450 nm in Figure 10.2 was not observed for 532 nm in Figure 10.3.

The waveguide width sweep of the 300 nm wide waveguide at a wavelength of 639 nm is shown in Figure 11.6. The difference in TM mode loss is explained by assuming a smaller width of the measured waveguides and the TE mode loss is overestimated.

Carrying out the width sweep for a target width of 500 nm at 730 nm wavelength yields the result shown in Figure 11.7. As seen in Figures 11.3e and f, the simulation of the intended width is already a good fit, while a reduced waveguide width provides results closer to the measured loss.

By sweeping the waveguide width, the deviation of the simulation from the measurement for 730 nm can be explained by assuming that the measured waveguides were more narrow than assumed. For the lower wavelengths 450 and 532 nm for 250 nm width and 639 nm for 300 nm width, the sweep did not provide sufficient explanation. Whilst the loss of the TE mode for 532 nm can be explained by the sweep but shows a small overestimation, the loss of the TM mode is significantly underestimated. Likewise, the sweep of the 300 nm wide waveguide for 639 nm shows an overestimation of the TE mode loss while the TM mode loss is slightly overestimated. This leads to the conclusion that the differences are caused by the comparatively low wavelength in regards to the waveguide width. This

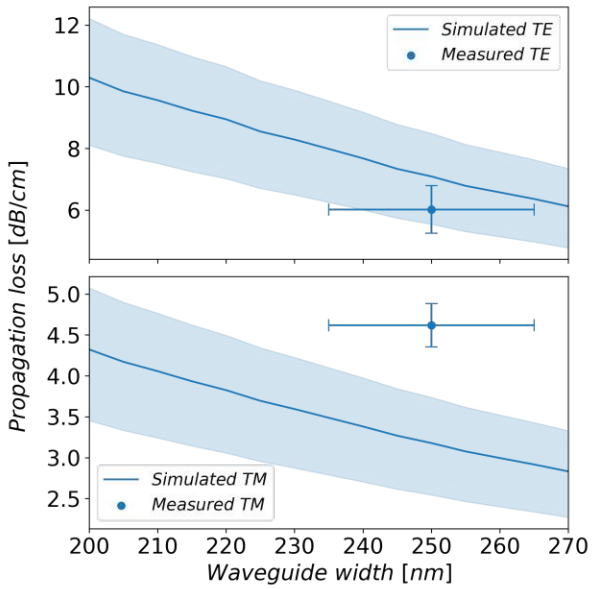

Figure 11.5: Propagation loss for the width sweep of a 250 nm waveguide at a wavelength of 532 nm.

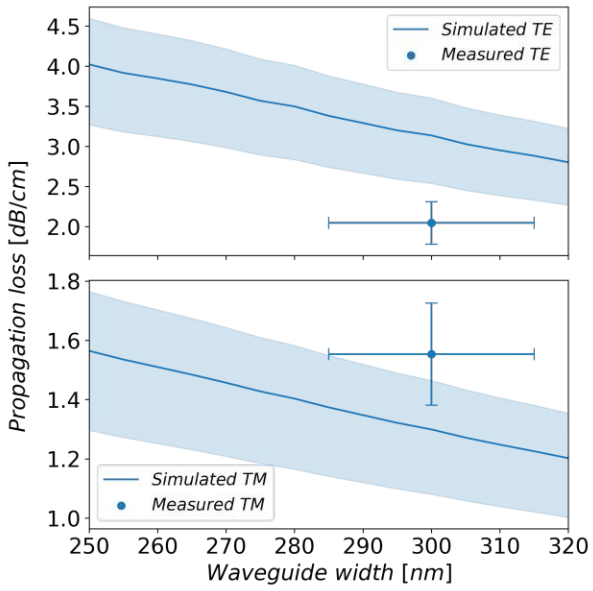

Figure 11.6: Propagation loss for the width sweep of a 300 nm waveguide at a wavelength of 639 nm.

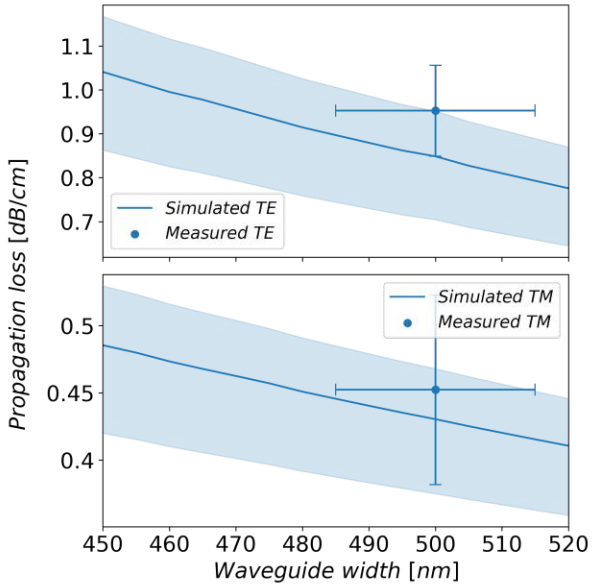

Figure 11.7: Propagation loss for the width sweep of a 500 nm waveguide at a wavelength of 730 nm.

could also be the case for the 250 nm width sweep at 450 nm wavelength, but because of the curvature observed in the losses of the different waveguide widths in Figure 10.2, another mechanism could cause the increased divergence from the measured losses.

Therefore, a simulation of the tapered waveguides with the measured 85° taper angle could provide better results, but as the correct extraction of these fields at the interfaces is not trivial for tapered waveguides, this is outside of the scope of this thesis.

As the position of the extracted field is vital to estimate the scattering loss, Table 11.1 shows the comparison of the calculated loss with the measured loss for the 250 nm wide waveguide with 532 nm laser light when using the electric field values inside and outside of the waveguide at a distance of 1 nm from the interface. It is therefore essential to extract the electric fields as close as possible on the inside of the interface between waveguide and cladding to get the best results.

	Loss Mean [dB/cm]	**Loss σ [dB/cm]**
Measurement TE	6.02	0.77
Sim TE outside	2.45	0.54
Sim TE inside	7.18	1.65

Table 11.1: Comparison of measured and calculated loss for 532 nm light in 250x170 nm waveguides for fields outside and inside the waveguide.

11.3 Influence of Roughness and Correlation Length on Scattering Loss

The previous chapter focused on comparing the measurement with the simulation. To estimate how changes in roughness parameters R_q, $L_{c,y}$, and $L_{c,z}$ influence the scattering loss, a simulation of a single sidewall of a 250 nm wide and 170 nm thick waveguide at a wavelength of 532 nm was performed. Figure 11.8a-c shows contour plots of the loss resulting from the sweep, where $L_{c,y}$ is 170 nm, 2.8 µm and ∞ for a-c respectively. The change in $L_{c,y}$ causes only an evenly distributed shift of the loss, but no change in the contour plot. The loss values from 170 nm to 2.8 µm change significantly, while the change from 2.8 µm to ∞ is marginal, it is therefore justified to assume a $L_{c,y}$ value of ∞ as was done in [15] for waveguides that exhibit curtaining. A decrease in R_q results in a smaller scattering loss, due to the dependence of the scattering loss on the square of the RMS roughness in Equation 5.23. Very short or very long correlation lengths in z-direction result in a reduction of the loss which is caused by the fraction in Equation 5.23.

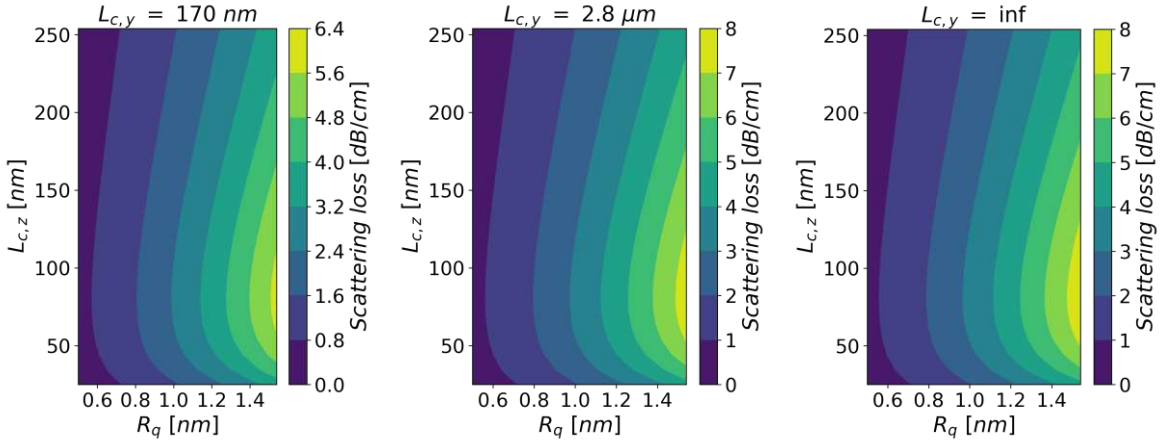

(a) (b) (c)

Figure 11.8: Calculated scattering loss of a single sidewall of a 250 nm wide and 170 nm thick waveguide for a wavelength of 532 nm for a sweep of R_q and $L_{c,z}$. The loss is shifted dependent on the values chosen for $L_{c,y}$ with (a) 170 nm, (b) 2.8 µm, and (c) ∞.

The shape of the $L_{c,z}$ dependence changes with the wavelength because the variable q in Equation 5.23 of the spectrum $S(q)$ is $(\beta - k_z)$, with $k_z = \cos(\theta)k$ where θ is a spatial angle, as seen in Equation 5.21. This results in peak broadening of the $L_{c,z}$ dependence for 730 nm light compared to 532 nm.

Physically, the correlation length L_c describes the distance over which the sidewall roughness profile remains similar. A short L_c corresponds to rapidly varying and high spatial-frequency roughness, while a long L_c means slowly varying and low spatial-frequency roughness. When L_c is much smaller than the wavelength, roughly by a factor of 10,

the roughness mostly contains very high spatial frequencies, which means guided modes cannot efficiently couple to radiation modes. In this limit, the mode experiences the surface as effectively smooth, analogous to the effective medium theory in metamaterials. However, when L_c is much larger, the roughness varies slowly and its spectrum becomes too narrow to provide the momentum for scattering, reducing the loss. According to Hoermann et al. [15] the peak position is the length at which the surface roughness follows the mode oscillation and maximum coherence of the scattered radiation occurs so the peak position shifts with wavelength through the λ-dependence of β and k_z. This λ-dependence could also be the reason for the peak broadening, as β and k_z do not necessarily change at the same rate, which can cause smaller q for longer wavelengths, and in turn the $L_{c,z}$ dependence is wider as the denominator in 5.23 varies slowly. This is the case for $L_{c,z} = \frac{\lambda}{2\pi}$ which matches the peaks in Figure 11.9.

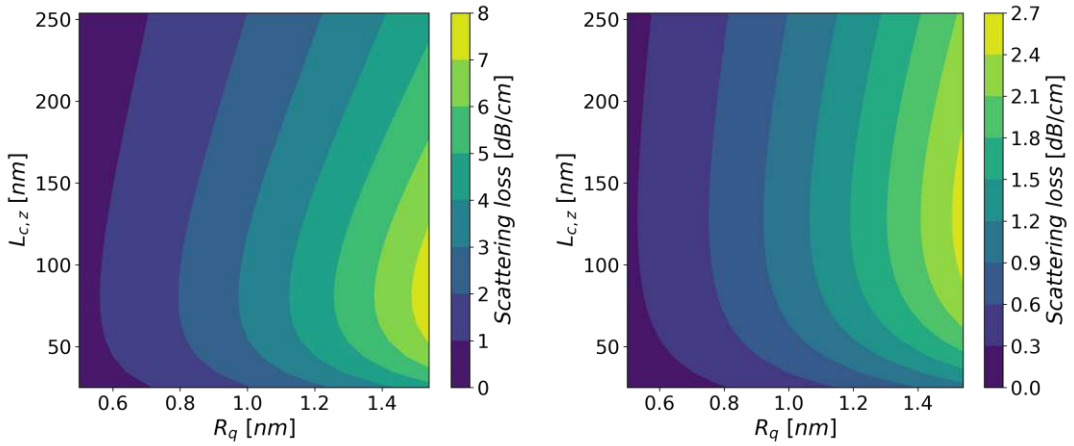

(a) (b)

Figure 11.9: Calculated scattering loss of a single sidewall of a 250 nm wide and 170 nm thick waveguide for a wavelength of (a) 532 nm and (b) 730 nm for a sweep of R_q and $L_{c,z}$. For both a $L_{c,z}$ value of 2.8 µm was used.

CHAPTER 12

Conclusion

In conclusion, waveguides were successfully fabricated and measured using our integrated optics setup and different models for the absorption loss were implemented. The SiN used for the fabrication was characterised to ensure a close match with the simulated waveguides in Ansys Lumerical. Furthermore, the simulation does not provide built-in loss estimation as the absorption is not included for SiN. The measured refractive index shows a close match with the index values used for simulation, as well as providing a good fit. However, a significant deviation from the physical model to the measured material losses was observed, which requires further investigation and measurements with wavelengths especially below 400 nm. An exponential fit was found which best describes both the refractive index and the measured loss as functions of the wavelength in the spectral range of 375 to 730 nm. This was used to calculate the material absorption loss for the simulated waveguides.

Variations of etchers and different etching methods were investigated to find the best suitable process to structure SiN waveguides with taper angles close to 90° and low roughness. Sidewall roughness measurements were performed for different fabrication processes, with the best process yielding a R_q value of 1.05±0.12 nm and a $L_{c,z}$ value of 67±16 nm at a taper angle of 85°. As shown in Figure 11.9 the scattering loss scales with R_q^2, while either a very short or very long $L_{c,z}$ with respect to $\lambda/2\pi$ is beneficial.

Simulations of the waveguide loss using the Hoermann model and an exponential material loss fit showed an overall acceptable agreement with the measured values. For 450 nm laser light, large deviations from the simulated results were observed, which warrant further investigation. The best fit was observed for the 500 nm wide waveguides at 730 nm light, where the differences in mean loss between simulation and measurement are 0.098 and 0.019 dB/cm, at losses close to 1 and 0.5 dB/cm for TE and TM respectively. The 250 nm wide

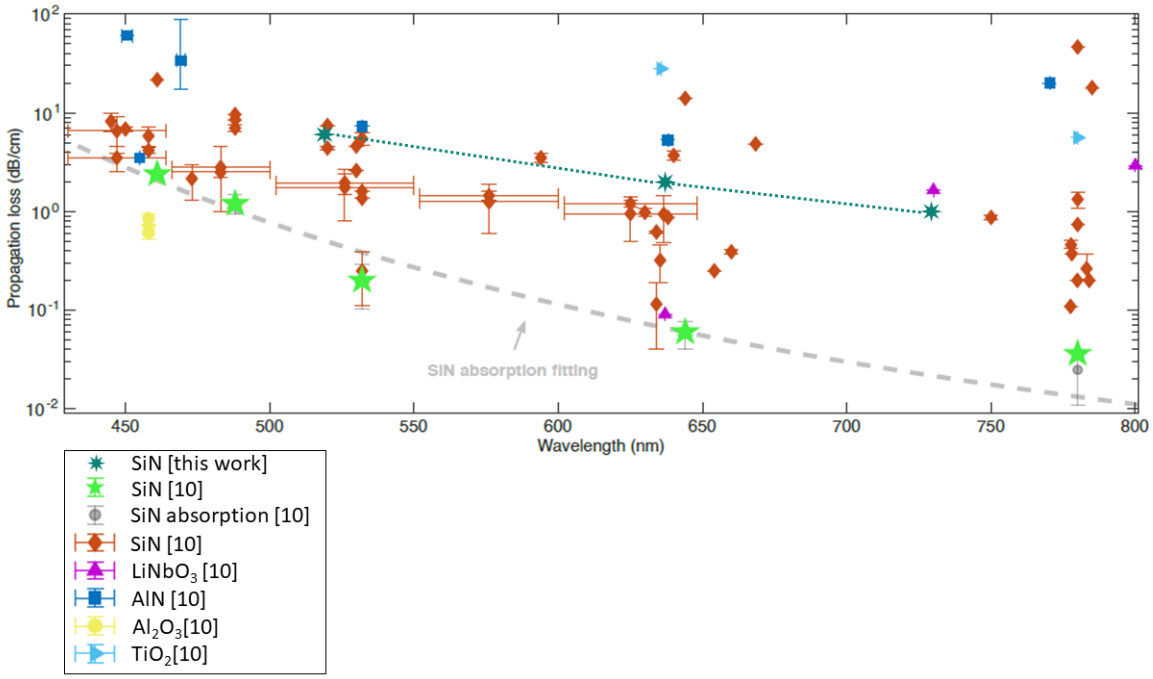

Figure 12.1: Comparison of waveguide losses modified from [13]. The best achieved losses in this thesis for the corresponding wavelength are added with ocean green eight-pointed stars with the dotted line to guide the eye.

waveguides for 532 and 639 nm light showed unaccounted for differences of ∼1-2 dB/cm. Changes in the width of the assumed perfectly rectangular waveguides were simulated to investigate if the differences stem from the smaller waveguide widths of the fabricated waveguides but could not fully explain the contrast between simulation and measurement.

Lastly, Figure 12.1 shows previously published waveguide losses taken directly from Zanarella et al. [13] with the addition of the losses from this thesis in ocean blue eight-pointed stars. It shows that the measured losses are comparable. Although other publications achieve lower values, this is due to multimode operation of the waveguides as well as low confinement, which reduces the losses incurred by material absorption and scattering.

The investigation of roughness-induced scattering losses in waveguides, combined with the exploration of fabrication approaches, has yielded significant insights into optimising PIC fabrication. Through analysis of sidewall roughness resulting from different etching techniques, the best etcher has been determined and compared to literature values. Furthermore, with the measured and simulated waveguide propagation losses, this thesis contributes to the development of low-loss optical waveguides. However, there are opportunities for further improvement.

Although current fabrication techniques have demonstrated sidewall roughness values comparable to reported benchmarks, further optimisation of etching methods, such as refining etch parameters and utilising advanced etch chemistries, could push the boundaries of achievable smoothness. Another possibility is the use of further layer deposition after etching to smooth the surface. Even if the sidewall roughness can be reduced, this thesis has shown that the SiN used is highly absorbent for wavelengths <400 nm. Therefore, advancements in material-dependent loss such as ultra-low-loss dielectrics or hybrid III-V platforms could offer a solution for the high loss of UV wavelengths. The implemented scattering loss model could be extended to account for the tapered waveguide cross-section to improve the accuracy of the simulations, while further measurements of the material loss could lead to more accurate fits thereof.

Reducing waveguide losses, especially in the visible to UV wavelength range, could enable dramatic performance improvements across various applications. Suppressing losses opens pathways for denser, larger-scale PICs with complex functionalities, such as integrated multiplexers, filters, modulators, and detectors. This could accelerate adoption in telecommunications, sensing, and LiDAR systems. For photonic integrated circuits designed for trapped ion quantum computing, ultra-low-loss waveguides are critical to achieving efficient light delivery and maintaining high fidelity in optical interactions with ions. The results achieved lay a strong foundation for future work in fabrication techniques to meet the loss requirements, supporting scalable ion trapping architectures. The predictive loss modelling combined with experimental validation guides design choices, further improving light delivery performance and integration density of PICs for trapped ion quantum computing. In conclusion, the ultimate goal of realising fully integrated quantum computing platforms with PICs remains within sight, supported by the foundational insights from studies such as this thesis.

Bibliography

[1] A. Agneter *et al.*, "Cmos optoelectronic spectrometer based on photonic integrated circuit for in vivo 3d optical coherence tomography", *PhotoniX*, vol. 5, no. 1, Oct. 2024. DOI: 10.1186/s43074-024-00150-7.

[2] N. Koompai, P. Limsuwan, X. Le Roux, V. Laurent, M.-M. Delphine, and P. Chaisakul, "Analysis of si3n4 waveguides for on-chip gas sensing by optical absorption within the mid-infrared region between 2.7 and 3.4µm", *Results in Physics*, vol. 16, p. 102 957, 2020. DOI: https://doi.org/10.1016/j.rinp.2020.102957.

[3] Y. Lin *et al.*, "Monolithically integrated, broadband, high-efficiency silicon nitride-on-silicon waveguide photodetectors in a visible-light integrated photonics platform", *Nature Communications*, vol. 13, no. 1, Oct. 2022. DOI: 10.1038/s41467-022-34100-3.

[4] S. G. Menon, N. Glachman, M. Pompili, A. Dibos, and H. Bernien, "An integrated atom array-nanophotonic chip platform with background-free imaging", *Nature Communications*, vol. 15, no. 1, Jul. 2024. DOI: 10.1038/s41467-024-50355-4.

[5] J. Wang *et al.*, "Multidimensional quantum entanglement with large-scale integrated optics", *Science*, vol. 360, no. 6386, pp. 285–291, Mar. 2018. DOI: 10.1126/science.aar7053.

[6] K. K. Mehta, C. Zhang, M. Malinowski, T.-L. Nguyen, M. Stadler, and J. P. Home, "Integrated optical multi-ion quantum logic", *Nature*, vol. 586, no. 7830, pp. 533–537, Oct. 2020. DOI: 10.1038/s41586-020-2823-6.

[7] C. D. Bruzewicz, J. Chiaverini, R. McConnell, and J. M. Sage, "Trapped-ion quantum computing: Progress and challenges", *Applied Physics Reviews*, vol. 6, no. 2, p. 021 314, Jun. 2019. DOI: 10.1063/1.5088164.

[8] J. I. Cirac and P. Zoller, "Quantum computations with cold trapped ions", *Physical Review Letters*, vol. 74, no. 20, pp. 4091–4094, May 1995. DOI: 10.1103/physrevlett.74.4091.

[9] C. Ospelkaus *et al.*, "Microwave quantum logic gates for trapped ions", *Nature*, vol. 476, no. 7359, pp. 181–184, Aug. 2011. DOI: 10.1038/nature10290.

[10] S. Auchter *et al.*, "Industrially microfabricated ion trap with 1 ev trap depth", *Quantum Science and Technology*, vol. 7, no. 3, p. 035 015, May 2022. DOI: 10.1088/2058-9565/ac7072.

[11] D. U. Chrsitopher Monroe, https://iontrap.duke.edu/resources/ion-periodic-table/, Accessed: 2025.09.07.

[12] D. Melati, A. Melloni, and F. Morichetti, "Real photonic waveguides: Guiding light through imperfections", *Advances in Optics and Photonics*, vol. 6, no. 2, p. 156, May 2014. DOI: 10.1364/aop.6.000156.

[13] M. C. Zanarella, X. Ji, A. Mohanty, and M. Lipson, "Absorption and scattering limits of integrated photonics in the visible spectrum", *Optics Express*, May 2023. DOI: 10.1364/opticaopen.22783628.v1.

[14] F. P. Payne and J. P. R. Lacey, "A theoretical analysis of scattering loss from planar optical waveguides", *Optical and Quantum Electronics*, vol. 26, no. 10, pp. 977–986, Oct. 1994. DOI: 10.1007/bf00708339.

[15] S. M. Hörmann, J. W. Hinum-Wagner, and A. Bergmann, "An ab initio, fully coherent, semi-analytical model of surface-roughness-induced scattering", *Journal of Lightwave Technology*, vol. 41, no. 5, pp. 1503–1510, Mar. 2023. DOI: 10.1109/jlt.2022.3224777.

[16] G. A. Reider, *Photonik : Eine Einführung in die Grundlagen*, ger, 4th ed. 2022. Berlin Heidelberg: Springer Berlin Heidelberg Imprint: Springer Vieweg, 2022.

[17] U. Mishra and J. Singh, *Semiconductor Device Physics and Design*, 1st. Springer Publishing Company, Incorporated, 2007.

[18] F. Urbach, "The long-wavelength edge of photographic sensitivity and of the electronic absorption of solids", *Physical Review*, vol. 92, no. 5, pp. 1324–1324, Dec. 1953. DOI: 10.1103/physrev.92.1324.

[19] N. Bacalis, E. N. Economou, and M. H. Cohen, "Simple derivation of exponential tails in the density of states", *Physical Review B*, vol. 37, no. 5, pp. 2714–2717, Feb. 1988. DOI: 10.1103/physrevb.37.2714.

[20] L. V. R.-d. Marcos and J. I. Larruquert, "Analytic optical-constant model derived from tauc-lorentz and urbach tail", *Optics Express*, vol. 24, no. 25, p. 28 561, Dec. 2016. DOI: 10.1364/oe.24.028561.

[21] M. Foldyna, K. Postava, J. Bouchala, J. Pistora, and T. Yamaguchi, "Model dielectric functional of amorphous materials including urbach tail", in *SPIE Proceedings*, J. Pistora, K. Postava, M. Hrabovsky, and B. S. Rawat, Eds., SPIE, Apr. 2004, pp. 301–305. DOI: 10.1117/12.560673.

[22] B. E. A. Saleh and M. C. Teich, *Guided-Wave Optics*. John Wiley & Sons, Ltd, 1991, ch. 7, pp. 238–271. DOI: https://doi.org/10.1002/0471213748.ch7.

[23] C. R. Pollock and M. Lipson, *Integrated Photonics*. Springer US, 2003. DOI: 10.1007/978-1-4757-5522-0.

[24] Z. Zhu and T. Brown, "Full-vectorial finite-difference analysis of microstructured optical fibers", *Optics Express*, vol. 10, pp. 853–864, Aug. 2002. DOI: 10.1364/OE.10.000853.

[25] A. C. Ltd. "Mode - finite difference eigenmode (fde) solver introduction". (2024), [Online]. Available: https://optics.ansys.com/hc/en-us/articles/360034917233-MODE-Finite-Difference-Eigenmode-FDE-solver-introduction (visited on 05/23/2025).

[26] D. Marcuse, "Radiation losses of dielectric waveguides in terms of the power spectrum of the wall distortion function", *Bell System Technical Journal*, vol. 48, no. 10, pp. 3233–3242, Dec. 1969. DOI: 10.1002/j.1538-7305.1969.tb01744.x.

[27] J. Lacey and F. Payne, "Radiation loss from planar waveguides with random wall imperfections", *IEE Proceedings J Optoelectronics*, vol. 137, no. 4, p. 282, 1990. DOI: 10.1049/ip-j.1990.0047.

[28] K. P. Yap *et al.*, "Correlation of scattering loss, sidewall roughness and waveguide width in silicon-on-insulator (soi) ridge waveguides", *Journal of Lightwave Technology*, vol. 27, no. 18, pp. 3999–4008, Sep. 2009. DOI: 10.1109/jlt.2009.2021562.

[29] T. Barwicz and H. Haus, "Three-dimensional analysis of scattering losses due to sidewall roughness in microphotonic waveguides", *Journal of Lightwave Technology*, vol. 23, no. 9, pp. 2719–2732, Sep. 2005. DOI: 10.1109/jlt.2005.850816.

[30] S. G. Johnson, M. Ibanescu, M. A. Skorobogatiy, O. Weisberg, J. D. Joannopoulos, and Y. Fink, "Perturbation theory for maxwell's equations with shifting material boundaries", *Physical Review E*, vol. 65, no. 6, p. 066 611, Jun. 2002. DOI: 10.1103/physreve.65.066611.

[31] C. E. Rasmussen, *Gaussian processes for machine learning*. MIT Press, 2006, p. 272.

[32] S. Y. Siew *et al.*, "Review of silicon photonics technology and platform development", *J. Lightwave Technol.*, vol. 39, no. 13, pp. 4374–4389, Jul. 2021.

[33] P. Rabiei, W. Steier, C. Zhang, and L. Dalton, "Polymer micro-ring filters and modulators", *Journal of Lightwave Technology*, vol. 20, no. 11, pp. 1968–1975, Nov. 2002. DOI: 10.1109/jlt.2002.803058.

[34] J. A. Smith, H. Francis, G. Navickaite, and M. J. Strain, "Sin foundry platform for high performance visible light integrated photonics", *Optical Materials Express*, vol. 13, no. 2, p. 458, Jan. 2023. DOI: 10.1364/ome.479871.

[35] X. Liu *et al.*, "Ultra-high-q UV microring resonators based on a single-crystalline AlN platform", *Optica*, vol. 5, no. 10, p. 1279, Oct. 2018. DOI: 10.1364/optica.5.001279.

[36] E. D. Palik, *Handbook of Optical Constants of Solids*, E. D. Palik, Ed. Burlington: Academic Press, 1997. DOI: https://doi.org/10.1016/B978-012544415-6.

[37] N. F. Tyndall *et al.*, "Foundry-based waveguide-enhanced raman spectroscopy in the visible", *Opt. Express*, vol. 32, no. 4, pp. 4745–4755, Feb. 2024. DOI: 10.1364/OE.504195.

[38] N. Chauhan *et al.*, *Trapped ion qubit and clock operations with a visible wavelength photonic coil resonator stabilized integrated brillouin laser*, 2024. DOI: 10.48550/ARXIV.2402.16742.

[39] C. G. H. Roeloffzen *et al.*, "Low-loss si3n4 triplex optical waveguides: Technology and applications overview", *IEEE Journal of Selected Topics in Quantum Electronics*, vol. 24, no. 4, pp. 1–21, 2018. DOI: 10.1109/JSTQE.2018.2793945.

[40] M. W. Puckett *et al.*, "422 million intrinsic quality factor planar integrated all-waveguide resonator with sub-mhz linewidth", *Nature Communications*, vol. 12, no. 1, Feb. 2021. DOI: 10.1038/s41467-021-21205-4.

[41] D. Bose *et al.*, *Anneal-free ultra-low loss silicon nitride integrated photonics*, 2023. DOI: 10.48550/ARXIV.2309.04070.

[42] S. Roberts, X. Ji, J. Cardenas, M. Corato-Zanarella, and M. Lipson, "Measurements and modeling of atomic-scale sidewall roughness and losses in integrated photonic devices", *Advanced Optical Materials*, 2021. DOI: 10.48550/ARXIV.2105.11477.

[43] C. Sorace-Agaskar *et al.*, "Versatile silicon nitride and alumina integrated photonic platforms for the ultraviolet to short-wave infrared", *IEEE Journal of Selected Topics in Quantum Electronics*, vol. 25, no. 5, pp. 1–15, 2019. DOI: 10.1109/JSTQE.2019.2904443.

[44] N. Chauhan *et al.*, "Ultra-low loss visible light waveguides for integrated atomic, molecular, and quantum photonics", *Optics Express*, vol. 30, no. 5, p. 6960, Feb. 2022. DOI: 10.1364/oe.448938.

[45] G. N. West *et al.*, "Low-loss integrated photonics for the blue and ultraviolet regime", *APL Photonics*, vol. 4, no. 2, p. 026 101, Feb. 2019. DOI: 10.1063/1.5052502.

[46] O. Jaramillo, V. Natarajan, H. M. Rivy, J. Tensuan, L. Massai, and K. K. Mehta, "Hfo2-based platform for high-index-contrast visible and uv integrated photonics", *Opt. Lett.*, vol. 50, no. 10, pp. 3165–3168, May 2025. DOI: 10.1364/OL.553552.

[47] M. Corporation, https://www.metricon.com, Accessed: 2025.08.07.

[48] A. C. Ltd., https://optics.ansys.com/hc/en-us/articles/360042304694-Evanescent-waveguide-couplers, Accessed: 2025.08.07.

[49] N. Marchack *et al.*, "Reducing Line Edge Roughness in Si and SiN through plasma etch chemistry optimization for photonic waveguide applications", in *Advanced Etch Technology for Nanopatterning VI*, S. U. Engelmann, Ed., International Society for Optics and Photonics, vol. 10149, SPIE, 2017, 101490F. DOI: 10.1117/12.2258112.

List of Figures

List of Tables